Electrochemical Stability of Nanoscale Electrodes

by

Xiaoqian Li

A Dissertation Presented in Partial Fulfillment
of the Requirements for the Degree
Doctor of Philosophy

Approved September 2012 by the
Graduate Supervisory Committee:

Karl Sieradzki, Chair
Daniel Buttry
Peter Crozier
Cody Friesen

ARIZONA STATE UNIVERSITY

December 2012

ABSTRACT

The electrochemical behavior of nanoscale solids has become an important topic to applications, such as catalysis, sensing, and nano-electronic devices. The electrochemical behavior of elemental metal and alloy particles was studied in this work both theoretically and experimentally. A systematic thermodynamic derivation for the size-dependent Pourbaix Diagram for elemental metal particles is presented. The stability of Pt particles was studied by *in situ* electrochemical scanning tunneling microscopy (ECSTM). It is shown that small Pt particles dissolve at a lower potential than the corresponding bulk material. For the alloy particles, two size ranges of AuAg particles, 4 nm and 40 nm in diameter, were synthesized by co-reduction of the salts of Au and Ag from an aqueous phase. The alloy particles were dealloyed at a series of potential by chronoamperometry in acid, and the resulting morphology and composition were characterized by electron microscopy, energy dispersive X-ray spectroscopy (EDX). In the case of the smaller particles, only surface dealloying occurred yielding a core-shell structure. A porous structure was observed for the larger particles when the potential was larger than a critical value that was within 50 mV of the thermodynamic prediction.

ACKNOWLEDGMENTS

First of all, I would like to acknowledge my advisor, Dr. Karl Sieradzki for his support and guidance throughout my Ph.D. study. No matter what kind of problems that I met, he was always beside me and worked through the difficulties with me. As a mentor, he taught me a lot not only in theory and knowledge, but also in the way of doing research and solving problems. In addition, he always gave me the freedom and chances to learn and try. His interests and persistence in science has a great influence on me, which is a perpetual impetus during my research studies. I would like to show my profound obligation to my co-advisor, Dr. Peter Crozier, who gave me a lot of guidance and help on electron microscopes. He is amazing in teaching and I have learned a lot from him both from class and experiment. I want to express my appreciation to Dr. Dan Buttry for his valuable guidance on nanoparticles and chemistry. I also want to thank Dr. Cody Friesen for offering the resources for vacuum STM experiment and thin film depositions in his lab.

I would like to thank Dr. Lei Tang, who is a former Ph.D. student and a post-doctorate in our lab. She gave me tremendous help on many experimental techniques and taught most of the fundamental knowledge about electrochemistry and thin films. I also want to thank my lab-mates, Shaofeng Sun and Qing Chen, for their valuable discussions on my research and assistance during experiment. I am grateful to Dr. Jungwoo Nah and Dr. Jordan Kennedy for their assistance on thin film deposition and vacuum STM experiment. I am obliged to Dr. Nan Jiang, Dr. Zhengtao Deng, Dr. Poonam Singh and Christopher Starr for their help and

suggestions on nanoparticle synthesis and characterization. I want to thank Dr. John Mardinly for his help on Aberration Corrected Microscope. In addition, I would like to acknowledge the use of facilities in the LeRoy Eyring Center for Solid State Science.

Finally I would like to thank my husband, Dr. Jin Fan, who is also my best friend, for his love, patient, understanding and persistent support during my life as a Ph.D. student. Without him, I wouldn't achieve what I have today. I am grateful to my parents for their love and support through my life. They made everything possible.

TABLE OF CONTENTS

Page

CHAPTER

APPENDIX

LIST OF TABLES

Table Page

LIST OF FIGURES

Figure Page

Figure Page

Chapter 1

INTRODUCTION

Dealloying is a corrosion process that results in the selective dissolution of one or more elements from an alloy. Research and speculation on the mechanism of dealloying of bulk materials dates back almost 100 years [1]. In the past 25 years, considerable experimental and theoretical work has been done which has provided a basis for understanding this process in bulk alloys [2–9]. Although several groups have reported the dealloying behavior of Pt alloy particles, generally emphasizing the composition and structure of the dealloyed particles [4–6], to the best of our knowledge, little work has been done examining the details of the dealloying mechanism for nanoscale alloys. The major objectives of this research project are to study the electrochemical stability and corrosion behavior of elemental metals/alloys at the nanoscale, and to develop a continuum model to understand and predict this behavior.

A fundamental understanding of the corrosion behavior for nano-structures is extremely important in the electrochemistry field. This information is essential both theoretically and technologically in areas ranging from sensing to energy storage and production [10–13]. In some applications, corrosion of the alloy is what we want to avoid since the resulting porous structure may be brittle and has been linked to stress corrosion cracking in many alloy systems [14,15]. However, in other areas, different degrees of dealloying are used to fabricate a variety of structures that have novel properties. An important example of this relates to Pt or Pt alloy catalysts that are used or are planning to be used as cathodes in polymer electrolyte membrane fuel cells [16–19]. It is reported by Stamenkovic that surface dealloyed Pt-M (M=Ni, Cu, Fe, Co) nanoalloy catalysts show significantly enhanced oxygen reduction behavior [19]. Another paper from Shao's group [16] shows that Pt coated porous Pd-Cu nanoparticles also exhibit much higher oxygen reduction reaction activity than the state-of-the-art Pt/C catalysts. Understanding the thermodynamics and kinetics of dealloying and the stability of these structures at the nanoscale is very important.

The key factor that differentiates dealloying behavior of nanoparticles from that of the bulk, is the size effect which causes larger specific surface area, lower electrochemical equilibrium potential, lower melting point, etc. [20,21]. The richness of this project lies in that there are two intrinsic length scales. One is set by the composition which is estimated from percolation theory [2]. The other is the actual physical size of the alloy nanoparticles. It is expected that the interaction of these length scales drive different phenomena differentiating nanoparticle dealloying from that in a bulk alloy.

This dissertation is organized in four chapters. In Chapter 2, a detail description of the experimental methods, procedures and equipments covered in the project is introduced. Chapter 3 includes the theoretical thermodynamic derivation for the size dependent electrochemical stability for elemental metal nanoparticles, and the experimental results and analysis on the stability of Pt nanoparticles. The background and experimental work on dealloying behavior of alloy particles is presented in Chapter 4. In the background, the dealloying of bulk materials is summarized from both theoretical and experimental point of view, and a general thermodynamic analysis on nanoparticle dealloying is presented. The experimental results and analysis on the dealloying of AuAg alloy particles in two size ranges is then described.

Chapter 2

TECHNIQUES AND EXPERIMENTAL PROCEDURES

2.1 Electrochemistry experiments

All glassware and the electrochemical cell that was used for experiments were cleaned using hot concentrated HNO_3 (60°C) for 10 minutes and then rinsed with de-ionized water seven times. Then they were cleaned in hot concentrated H_2SO_4 (60°C) for 10 minutes and then rinsed with de-ionized water for seven times. Finally, they were rinsed with Barnstead Nanopure (>18 MΩ cm) water seven times. After the acid clean, the glassware and Teflon cells were dried in an oven set at ~70°C.

The simplest setup for an electrochemistry experiment includes three electrodes. The "working" electrode is the electrode for which the reactions that one is interested in occur. The reference electrode is used to gauge the potential and the counter electrode passes all the current needed to balance the charge.

The reference electrode usually contains a redox system with prescribed concentrations of each component of the redox reaction [22]. The most frequently used standard reference electrodes in aqueous electrolyte are mercury/mercurous sulfate electrode (Hg/Hg_2SO_4, MSE), saturated calomel electrode (Hg/Hg_2Cl_2, SCE), silver/silver chloride electrode (Ag/AgCl) and mercury/mercury oxide electrode (Hg/HgO). Since most commercial MSE and SCE reference electrodes use glass frits, they are normally used in acid or neutral electrolyte, while

Hg/HgO is used in basic solutions. All the standard electrodes used in the experiment of this project were ordered from Koslow Scientific Company.

To increase the ion conductivity and prevent contamination, a salt bridge is used between the electrolyte and the reference electrode. The salt bridge normally uses a similar electrolyte as the reference electrode in order not to introduce an extra liquid-phase junction. For example, 0.1 M KCl is used for the salt bridge for a SCE.

Besides standard reference electrode, certain elemental metals can be used as pseudo-reference electrodes in some electrolytes. For example, for an acid solution containing Ag^+, a Ag wire can be used as a reference electrode for which the equilibrium potential is determined by the Nernst equation:

$$E = E^0 - \frac{RT}{nF}\ln[Ag^+]. \qquad (2.1)$$

The potentials of the most frequently used reference electrodes are listed in Table 2.1.

Table 2.1 Equilibrium potentials of frequently used reference electrodes

Electrode	**Potential vs. NHE at 25°C**	**Reference**
Hg/Hg_2Cl_2, KCl (sat'd)	0.241V	[22,23]
Ag/AgCl, KCl (sat'd)	0.197V	[22]
Hg/Hg_2SO_4, K_2SO_4(sat'd)	0.65V	[23]
Hg/HgO, KOH (20%)	0.098V	[24]
Ag/Ag^+, Ag^+ (1M)	0.8V	
Cu/ Cu^{2+}, Cu^{2+} (1M)	0.34V	
Pd/H, H_2SO_4 (0.1M)	0V	[25]

The noble metal electrodes, such as Au, Pt, Ir and Pd, are normally cleaned in hot nitric acid and sulfuric acid, and then annealed in a H_2 flame. For Cu and Ag electrodes, dilute nitric acid (conc. $HNO_3 : H_2O = 1 : 2$) is used to remove the surface oxide.

All the dealloying experiments in this project were performed using a Gamry Series G potentiostat.

2.2 Microscopy

Several microscopy and spectroscopy techniques were used for sample characterization in this project, such as scanning electron microscopy (SEM), transmission electron microscopy (TEM), scanning transmission electron microscopy (STEM), energy dispersive X-ray spectroscopy (EDS), electron energy loss spectroscopy (EELS), scanning probe microscopy (SPM) including scanning tunneling microscopy (STM) and atomic force microscopy (AFM). The principles for the techniques and the equipments that were used in experiment are described below.

2.2.1 SEM

All electron microscopes use a beam of electrons to generate a variety of signals from a specimen which come from electron-sample interactions. Those signals can provide all kinds of information about the specimen, such as morphology, structure and chemical composition.

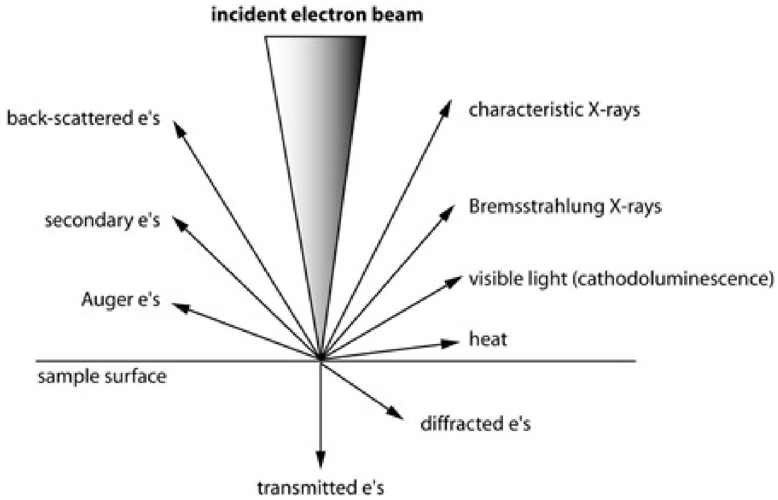

Figure 2.1. Types of signals generated from electron-sample interactions [26].

In SEM, the electron beam energy is typically between 0.2 keV to 30 keV, which is focused by a condenser lenses to a spot size of 1~5 nm in diameter. The major signal that is used for imaging is secondary electrons (<50 eV) which originate within a few nm from the sample surface. The secondary electron image reflects the surface morphology and topography of the specimen. Besides secondary electron, characteristic X-rays are also generated by electron interactions, which can be used for compositional analysis.

A Nova 200 NanoLab DualBeam-SEM/FIB operated and maintained by the LeRoy Eyring Center for Solid State Science (LE-CSSS) at Arizona State University was used to characterize the surface morphology in the project. The accelerating voltage is in the range from 0.2 kV to 30 kV and probe current is from 98 pA to 20 nA. The beam resolution can achieve 1.0 nm [27].

2.2.2 TEM

In TEM, an electron beam passes through the specimen and an image is formed from the interaction between electrons and the sample. The beam energy is in the range of 100~400 keV which is much higher than that of the SEM. A thin "electron transparent" specimen is necessary to avoid multiple scattering events which makes interpretation of the image contrast complicated. In theory, because of the small de Broglie wavelength of electrons, TEM can achieve atomic scale resolution.

There are three stages of lenses in TEM optics. The first stage includes two condenser lenses which are used for beam formation and focusing. The second stage is the objective lens which is the most important lens in the TEM. The objective lens forms an inverted image of the sample, and this image is subsequently magnified. The third stage includes intermediate lenses and projector lenses which are used to further magnify the image formed by objective lens [28].

Compared to the parallel electron beam in a conventional TEM, STEM uses a focused beam that is scanned over the sample in a raster. The optics difference between TEM and STEM is shown in Figure 2.2.

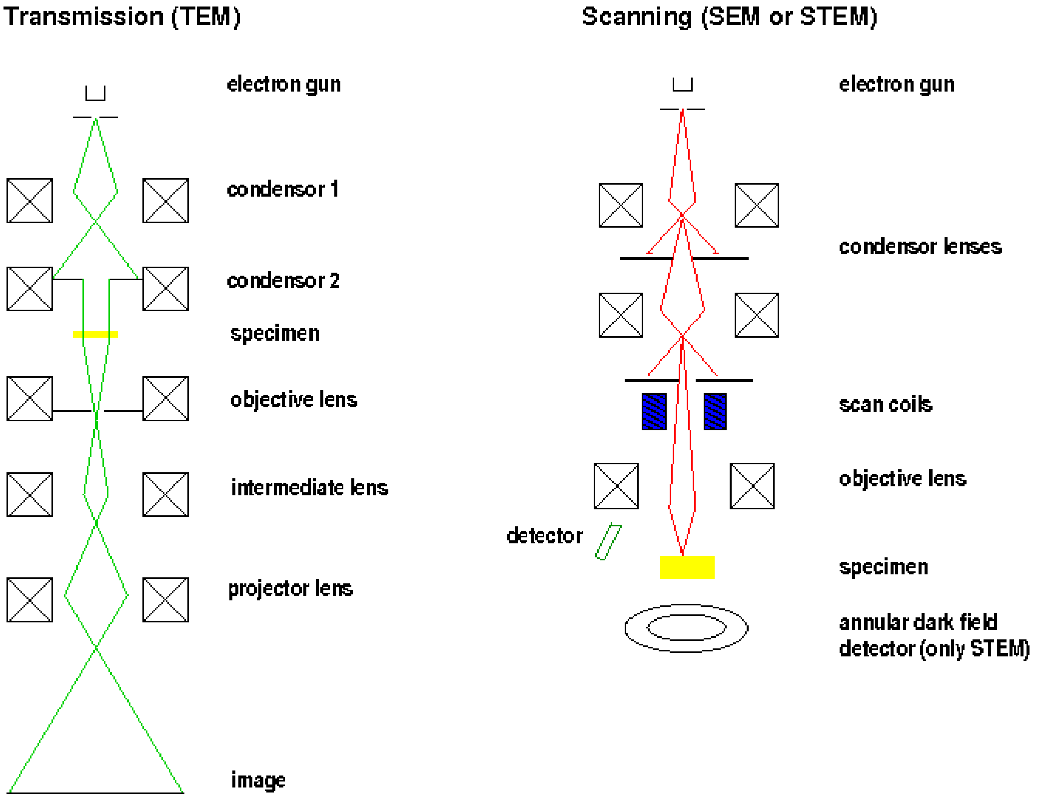

Figure 2.2. Structures and optical paths of TEM and STEM [29].

In STEM, a very important technique is high angle annular dark-field (HAADF) imaging. Here the image is formed by collecting the scattered electrons from a very high angle (>10°) which is highly sensitive to variations in the atomic number and sample thickness as shown by the following equation:

$$I \propto z^2 t, \tag{2.2}$$

in which, z is the atomic number of the element and *t* is the sample thickness.

Two analytical techniques, EDX and EELS, which are incorporated with STEM were used for the elemental analysis in this project.

The fundamental principle of EDX is that each element has a unique atomic structure; and the excited X-rays are characteristic of that element, so the elemental composition information of the sample can be determined from the generated characteristic X-rays. When a high-energy electron beam interacts with the sample, an inner shell electron of the sample element can be excited and ejected. Then, an outer shell electron with a higher energy fills the hole and the energy difference between higher energy and lower energy shell may be released in the form of an X-ray. The intensity and energy of the X-rays emitted from a specimen can be measured by the energy-dispersive spectrometer [28].

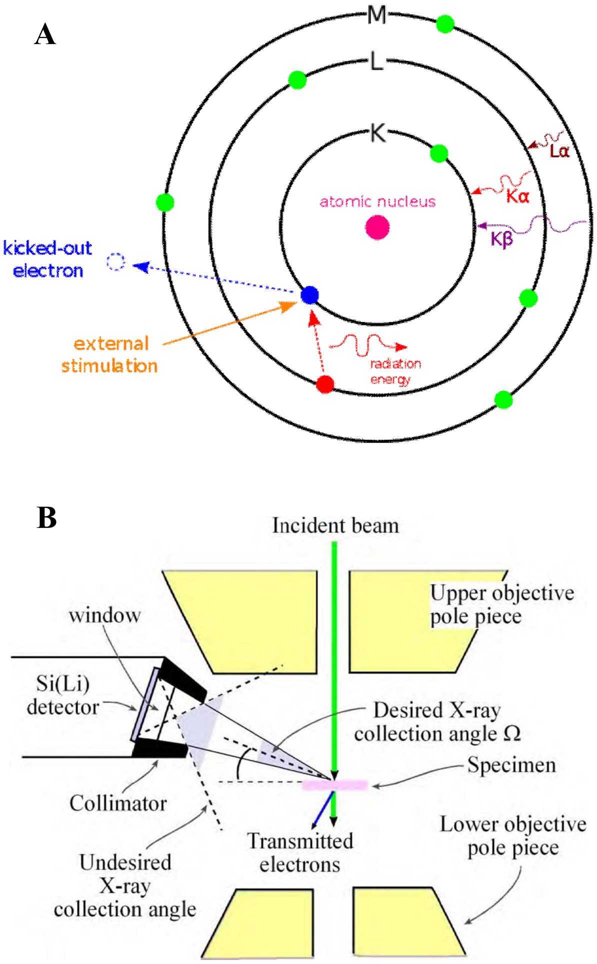

Figure 2.3. (A) Principle of X-ray generation when the electron beam interacts with materials. (B) Schematic diagram of the interface between the EDS and the TEM stage showing how the detector can “see” X-rays from regions other than the beam-specimen interaction volume over the undesired collection angle [28].

The most frequently detector for EDX is silicon-lithium [Si(Li)] semiconductor detector. It is a reverse-biased p-i-n diode. When X-rays interact with the detector, the energy transfers electrons from the valence band to the conduction band, which creates electron-hole (e-h) pairs. The energy required for each transfer in Si is ~3.8 eV, so the number of e-h pairs created is proportional to the incoming X-ray energy [28]. As shown in Figure 2.3(B), the detector is located at the side of the specimen and the collection angle Ω is in the range of 0.03 steradian (sr) to 0.3 sr, which is a small fraction of the total X-ray generation (4π sr).

The typical EDX spectrum is a plot of X-ray intensity versus X-ray energy ranging from 0 keV to 40 keV. The characteristic X-rays appear Gaussian-shaped peaks superimposed on a background of bremsstrahlung X-rays. The peak/background (P/B) ratio increases with the accelerating voltage. Three key parameters are considered: spatial resolution, energy resolution and chemical sensitivity. Although there is a large interaction volume with specimen for X-rays, the spatial resolution is close to the beam size for ultrathin specimens in TEM. The energy resolution shows the capability of identifying elements by distinguishing peaks. For a typical Si(Li) detector, the energy resolution is ~130 eV. The chemical sensitivity is just the detectability of one element, which depends on P/B ratio [28].

EELS is another spectroscopy technique that is widely used on many electron microscopes. During the electron-sample interaction, part of the electrons are inelastically scattered and lose a certain amount of the energy. This energy loss is related to the elemental information and atomic bonding state, which is the principle of EELS. The energy resolution for EELS can be less than 1 eV and the spatial resolution depends on the beam size. In an EELS spectrum, the low-loss region (<50 eV) contains electrons that have interacted with the weakly bound outer-shell electrons of the atoms, so it could give information about the electronic properties of the specimen. Electrons in the high-loss region have interacted with the more tightly bound inner-shell electrons, which gives information on the composition of the specimen.

Compared to EDX, EELS works better for relatively low atomic numbers (up to Zn), and it also has the capability of measuring the chemical bonding and local electronic state besides the composition analysis. In principle, EELS has a higher energy resolution and sometimes better spatial resolution than EDX. However, since the major signals for elemental analysis have an extended energy range above the ionization energy and sit on a high background, quantitative microanalysis using EELS is less accurate compared with EDX [28].

Two microscopes were used in this project. Both are maintained by LE-CSSS. JOEL-2010F TEM operated at 200 kV is equipped with a Schottky Field Emission Gun. The resolution could reach 0.19 nm. This microscope can operate in TEM and STEM modes and it is equipped with an Enfina PEELS Detector and EDAX Acquisition system for X-ray detection [30]. The other microscope is JEOL-ARM200F aberration corrected STEM equipped with a Schottky field emission gun and a CEOS CESCOR hexapole aberration corrector that enables imaging resolution of 78 pm, and beam current densities of 8 nA/nm^2. The microscope can be operated in high angle and medium angle annular dark-field STEM modes as well as bright field and annular bright field modes. It is equipped with a JEOL 50 square millimeter (0.3 St.) windowless light-element-sensitive X-ray detector [31].

2.2.3 SPM

The principle of STM is described in Figure 2.4. Basically, when a metal tip is brought close to a conducting sample surface, electron tunneling can happen under an applied bias between the two electrodes. The most simple physical model for this process is based on a assumption of a rectangular barrier between the two electrodes. The tunneling current decays exponentially with barrier width d as shown in equation (2.3) at a small bias V:

$$I \propto V\rho_s e^{-2d\sqrt{2m(\Phi-eV)/\hbar^2}}, \tag{2.3}$$

where ρ_s is the local density of state (DOS) near the Fermi level of the sample, Φ is the average work function of sample and tip. With a typical workfunction value ~5 eV, when the distance changes 1 Å, the current changes about one order of magnitude. In vacuum STM, this tunneling distance is below 1 nm, while in electrochemical STM, it can be several nano-meters (nm).

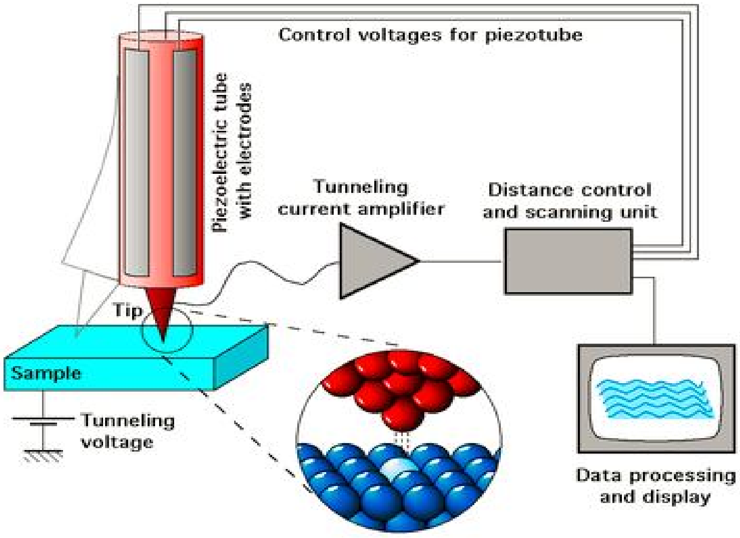

Figure 2.4. Schematic description of the STM working principle [32].

The probe tip is attached to a tube that consists of piezoelectric materials controlling the tip motion in x, y and z directions. The bias voltage between tip and sample is between 10 mV and 5 V and the tunneling current is typically between 10 pA and 5 nA. The electric feed-back loop contains a current amplifier that converts the tunneling current into voltage. When the surface is chemically uniform, which means the local DOS is constant across the surface, topography information can be generated by either measuring the tunneling current while keeping the height of the tip constant (current mode) or measuring the tip displacement in z direction while keeping the tunneling current constant (height mode). In the height mode, the tip moves up and down according to the topography of the surface, so the scan speed and the data acquisition are limited by the finite response time of the feed-back loop. For the current mode, the current variation is monitored and recorded without moving the tip vertically, so the surface must be quite flat in order to prevent tip crashing and scanning can be much faster than the height mode.

AFM is another scanning probe technique. Instead of using a tunneling current signal to detect the tip-sample distance, it uses the relationship between tip-sample distance and atomic force. Imaging is accomplished using a very sharp tip attached to the end of a cantilever. When the tip is very close to the sample surface, the atomic force between the tip and sample results in a deflection of the cantilever–the amount of which can be detected by an array of laser diode detectors. There are two frequently used modes in AFM: contact mode in which cantilever deflection is used as the feedback signal, and tapping mode in which the cantilever is driven to oscillate near its resonance frequency and the distance changes cause the oscillation amplitude changes.

All the STM experiments were carried out with a Molecular Imaging (MI) Pico Scan 300S scanner, Digital Instrument (DI) nanoscope E controller, and DI nanoscope software.

The AFM experiments were carried out in tapping mode with a Veeco Dimension 3100 AFM. The most common used probe for AFM tapping mode is made by silicon with a resonant frequency around 300 kHz.

2.3 ECSTM

2.3.1 Setup

The setup for ECSTM experiments was the same as the STM experiment. The potential control was provided by MI 300S Pico bi-potentiostat.

2.3.2 *Cell and electrodes*

All glassware and the electrochemical cell that were used in ECSTM were cleaned using hot concentrated HNO_3 (60°C) for 10 minutes and then rinsed with de-ionized water seven times. Then they were cleaned in hot concentrated H_2SO_4 (60°C) for 10 minutes and then rinsed with de-ionized water seven times. Finally, they were rinsed with Barnstead Nanopure (>18 MΩ cm) water seven times. The cell and glassware were then soaked in Piranha solution (concentrated H_2SO_4:30% H_2O_2 = 3:1) for at least 24 hours, followed by multiple rinsing in Barnstead Nanopure (>18 MΩ cm) water. The custom made Teflon-liquid cell of 1 cm^3 volume used in the experiment is shown in Figure 2.5. It exposes 0.23 cm^2 surface area of the sample.

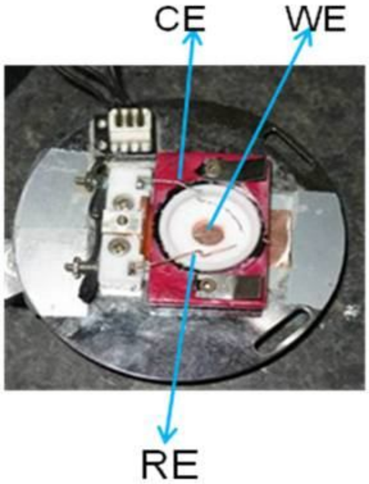

Figure 2.5. Customized ECSTM cell and sample holder. The two metal wires are the counter and reference electrodes (CE and RE). The bare area in the center of the Teflon cell is the working electrode (WE).

If there is a certain concentration of Ag^+ or Cu^{2+}, the corresponding metal wire was used as reference electrode. In other cases, the most frequently used reference electrode in ECSTM cell for acid and neutral electrolyte was the

Palladium Hydrogen (Pd-H) electrode, which is ~ 50 mV vs. RHE [33–35]. The electrolyte that is used to prepare Pd-H electrode is 0.1 M H_2SO_4. MSE is used as reference electrode. Palladium (Pd) wire (99.99%) as the working electrode is flamed annealed thoroughly before experiment to get rid of the residual hydrogen in the wire. PtIr wire is used as counter electrode. There are mainly four steps to load H into Pd wire. The first step is to run cyclic voltammetry of the Pd wire to make sure that there is no residual H in the wire, since the Pd-H electrode won't be stable if there is residual H initially. The second step is to accumulate H around the Pd wire through applying a negative potential. The third step includes loading H and stripping ~15% of the loaded H. The time for loading and stripping depends on the length of the Pd wire and concentration of the electrolyte. The last step is measuring the open circuit potential for several hours to see whether the electrode potential is stable. Normally, the potential of a good Pd-H electrode won't drift more than 5 mV overnight and the stability may last 1-2 days.

2.3.3 Substrates

For most STM and ECSTM experiments, Au thin film deposited by e-beam deposition was used as substrate. The vacuum chamber used for Au deposition is shown in Figure 2.6. A high purity Au (99.99%) source was cleaned in hot acid, rinsed with nanopure water and air dried. The sample holder was immersed in isoproponal and ultrasonically cleaned for 20 min. The base pressure of the vacuum chamber was normally ~2×10^{-7} torr. Typically Au thin films were deposited onto a freshly cleaved mica substrate (from SPI, Grade V-4 Mica) at 340°C ~370°C with an e-beam evaporation gun. The first 10 nm Au film is deposited at a rate of 0.1 Å/s as a seeding layer and then ~100 nm Au is deposited at 0.2 Å/s.

Figure 2.6. Vacuum chamber used for e-beam deposition.

For the *in-situ* ECSTM experiment on Pt nanoparticle stability, $Au_{0.95}Ag_{0.05}\{111\}$ films were used as substrates. A high purity Ag (99.99%) source was cleaned in dilute nitrate acid (conc. $HNO_3 : H_2O = 1 : 2$), rinsed with nanopure water and air dried. A 10 nm Au film was deposited at 0.1 Å/s as a seeding layer and then 150 nm of the AuAg alloy layer was deposited at 0.1 Å/s for Ag and 2.5 Å/s for Au. The addition of 5 at% Ag to the Au film was to help to avoid the $\sqrt{3} \times 22$ surface reconstruction which is lifted in 0.1 M H_2SO_4 at ~0.55 V NHE. The lifting of the reconstruction results in the formation of variously sized gold clusters on the surface which look quite similar to the Pt particles of interest [36]. Ancillary experiments have shown that this alloy surface was stable to morphology change in 0.1 M H_2SO_4 up to ~ 1.2 V vs. NHE.

2.3.4 Tip

The most frequently used materials for making STM tip are tungsten wire and Pt/Ir wire (80%Pt).

The old method of making Pt/Ir tip is a one step method. The electrolyte solution consists of $CaCl_2$ (sat.)/H_2O (15/30 mL). About 2~3 mm Pt/Ir wire is immersed in the electrolyte and electrochemically etched under a 30 V_{rms}/60 Hz potential until the wire in the solution drops off and the circuit is off. The SEM image of the general shape for the tip made by this method is shown in Figure 2.7. While tips produced in this manner do not appear to be sharp, there is no problem getting nice images on all sorts of sample surfaces with it since tunneling only happens between several atoms at the tip end and the sample surface. However, this method is not repeatable as only 3~4 tips out of ten are good enough for doing experiments. To improve the tip quality and yield, a new two-step method was investigated [37,38].

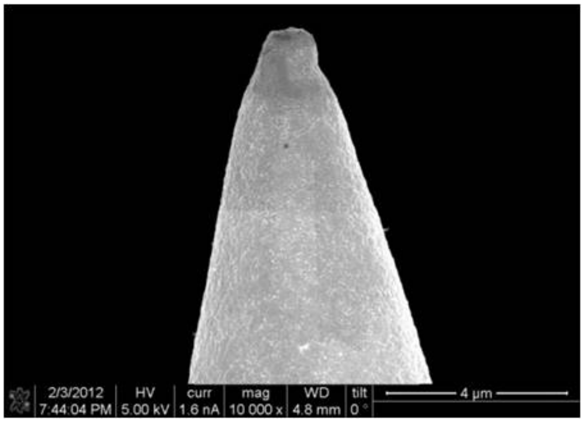

Figure 2.7. SEM image of a PtIr tip made by traditional one step method.

The schematic setup is shown in Figure 2.8. The first step is similar to the old etching method. About 1.5 mm wire is immersed into the electrolyte and a multi-meter is used to monitor the current of the reaction. Instead of etching it until the end falls off, the reaction is stopped when the current is lower than 40 nA which is about a tenth of the current at the beginning of etching. The shape of the tip after step one is shown in Figure 2.9(A). The purpose of step one is to get a thin enough neck and a decent size head.

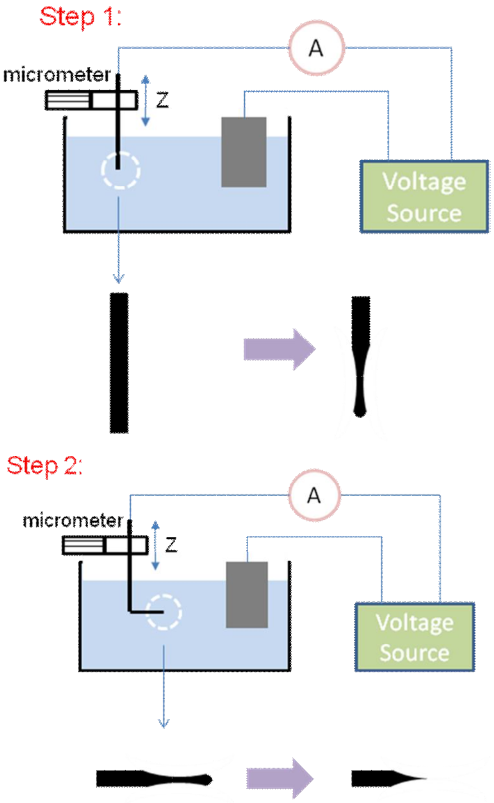

Figure 2.8. Schematic diagrams of the setups for two-step method of making PtIr tip.

In the second step, the tip is bent 90° about 2~3 mm above the droplet and immersed into H_2SO_4/H_2O (90/10 mL). Another Pt/Ir wire is used as both reference and counter electrode. BioLogic VMP3 potentiostat is used to generate a square wave at 500 Hz reaching 10 V for 0.2 ms and -0.5 V for 1.8 ms. The neck of the droplet becomes thinner and thinner and the head finally fall off which can be observed by eye. Then the potential is switched to a negative DC voltage of -1.1 V for 2 minutes to reduce the surface oxide. Figure 2.9(B) is the SEM image of the tip end and it can be seen that this method gives a much sharper tip shape than the old method. The problem with this two-step method is that the thinner tip end is soft and fragile, so it can not last very long during scanning especially for rough surface.

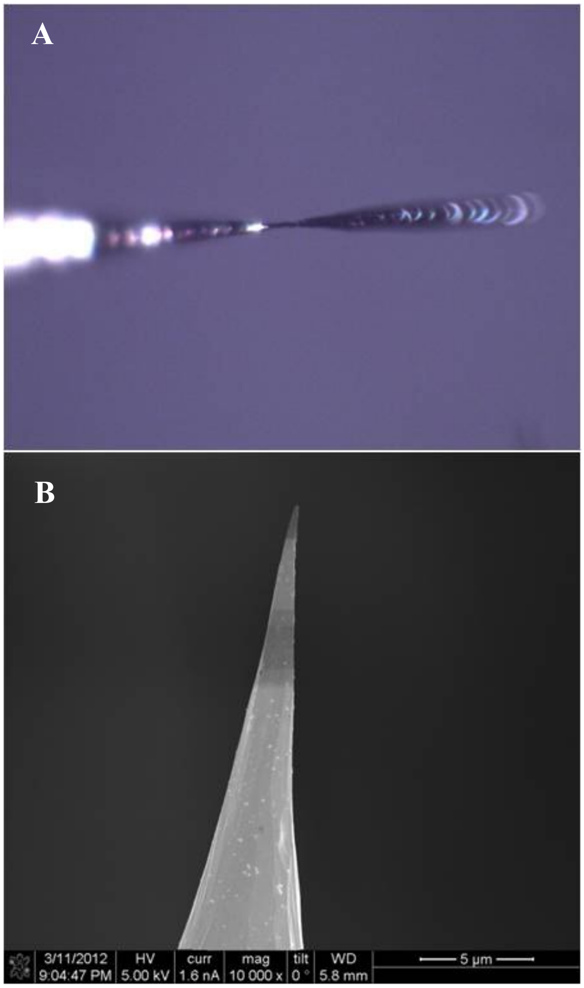

Figure 2.9. (A) Optical microscope image of the tip shape after step one. (B) SEM image of the tip shape after step two.

A Tungsten tip is made by etching a wire in 1 M NaOH using a 10~12 V AC potential [39]. A small amount of ethyl alcohol is added to the etching solution to inhibit bubble formation. Then the tip is rinsed with de-ionized water and dried in air. This is a quite repeatable method for producing sharp tips (Figure 2.10(A)), so W tips are widely used in vacuum STM. However, since W is easily oxidized in air, to use it in air, we electro-deposited a thin Au layer on the tip. Before coating, the tip was etched for a few second in NaOH solution to remove the oxide on the surface. Then the Au was electrochemically deposited onto the W tip in a two electrode electrochemical cell. The W tip was the cathode and a glassy carbon rod was used as the anode. The electrolyte was 1.5 mM $HAuCl_4$ + Glycol:HCl (3:1). A 3 V DC potential was applied between the two electrodes and the W tip taken out every 10 s to check the color of the deposited Au. The total deposition lasted for 2 minutes. A very light yellow color could be seen at the top end of the tip after deposition. The Au coated W tip was checked in SEM and it was found that the Au layer was quite rough. The coated tip was tested for STM imaging and there was no problem for imaging Au thin films or HOPG.

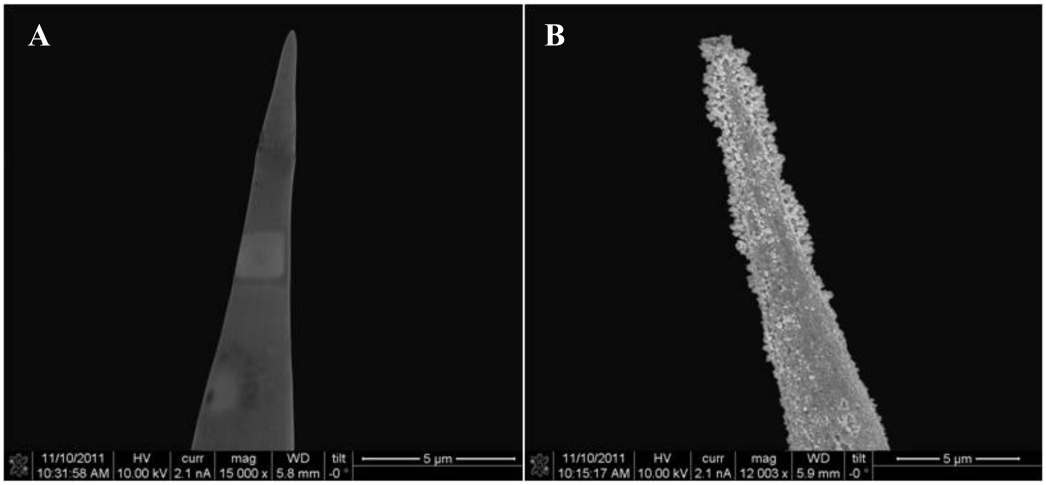

Figure 2.10. (A) SEM image of bare W tip. (B) SEM image of Au coated W tip.

To minimize the background Faradaic current from the tip in ECSTM experiments, the as prepared tips are normally coated with an insulator such as Apiezon wax to reduce the bare area of the tip. Since the most frequently used tunneling current is ~1 nA, the Faradaic current from the tip should be less than 20 pA. The prescription for Apiezon coating involves heating the wax to ~180 °C. The bare tip is immersed in the wax for a few seconds. Then the wax coated tip cools down at room temperature in air. The coated tip is examined in optical microscope to ensure that only the very end of the tip from which tunneling occurs is wax-free.

Chapter 3

CORROSION OF ELEMENTAL METAL PARTICLES

3.1 Background

3.1.1 Stability of elemental metal nanoparticle

When a single component solid, β, of radius r is in equilibrium with a surrounding fluid phase, α, Gibbs [40] showed that the chemical potential in the fluid is given by

$$\mu_l = [U_s - TS_s + (P_l + 2\gamma / r)V_s] / N_s \qquad (3.1)$$

in which s and l refer to the solid and fluid phase, (U_s–TS_s) is Helmholtz free energy, P_l is the pressure in fluid phase, V_s is molar volume of solid, N_s is the number of atoms per molar, r is the size of solid and γ is the interfacial free energy. The chemical potential in the solid when it is under uniform hydrostatic stress is given by

$$\mu_s = [U_s - TS_s + (P_l + 2f / r)V_s] / N_s \qquad (3.2)$$

In this expression, f is the surface stress. So, the chemical potential difference in the solid and fluid phase is given by,

$$\mu_s - \mu_l = \frac{2(f-\gamma)}{r}\left(\frac{V_s}{N_s}\right) = \frac{2(f-\gamma)\Omega}{r} \qquad (3.3)$$

In this expression, $V_s / N_s = \Omega$ is the atomic volume. It can be noted that for a planar solid surface, since $r \to \infty$, equation (3.3) reduces to $\mu_s = \mu_l$. Also, for fluid/fluid systems, since $f = \gamma$, we could get $\mu_s = \mu_l$.

For a multi-component solid, Cahn [20] showed that the chemical potential difference of a substitutional specie X between solid and fluid phase is given by,

$$\mu^s - \mu^l = \frac{2(f-\gamma)\langle\Omega\rangle}{r} \tag{3.4}$$

In this expression, $\langle\Omega\rangle$ is the average molar volume of the multi-component solid.

Based on the equilibrium conditions, we have derived the equilibrium equations for a finite size elemental particle. The relevant electrochemical and chemical equilibria that we considered are represented by the following set of equations:

(a) $M^{n+} + ne^- = M$

(b) $M_aO_n + 2nH^+ + 2ne^- = aM + nH_2O$

(c) $M_aO_n + 2nH^+ = aM^{n+} + nH_2O$

Assuming $\overline{a}_{M^{n+}}$ is the equilibrium metal-ion activity for planer solid, and $a_{M^{n+}}$ is the equilibrium ion activity for a finite size particle. The chemical potential of the liquid phase at $a_{M^{n+}}$ is,

$$\mu_l = \mu_l(\overline{a}_{M^{n+}}) + k_B T \ln(a_{M^{n+}} / \overline{a}_{M^{n+}}) \tag{3.5}$$

The chemical potential of the solid is,

$$\mu_s = \mu_l(\overline{a}_{M^{n+}}) + 2f\Omega / r \tag{3.6}$$

Applying equilibrium condition (3.3), we obtain,

$$-k_B T \ln(\frac{a_{M^{n+}}}{\overline{a}_{M^{n+}}}) = -\frac{2\gamma\Omega}{r} \tag{3.7}$$

So, at fixed concentration of metal cation, the equilibrium potential difference between a finite size solid and a planar solid surface is,

$$E(r,a_{M^{n+}})-\overline{E}(a_{M^{n+}})=-\frac{k_BT}{nq}\ln(\frac{a_{M^{n+}}}{\overline{a}_{M^{n+}}})=-\frac{2\gamma\Omega}{nqr} \tag{3.8}$$

For substitutional specie in a multi-component solid, the chemical potentials of the liquid phase and solid phase at $a_{M^{n+}}$ are,

$$\mu_X{}^l=\mu^l(\overline{a}_{X^{n+}})+k_BT\ln(a_{X^{n+}}/\overline{a}_{X^{n+}}) \tag{3.9}$$

$$\mu_X{}^s=\mu^s(\overline{a}_{X^{n+}})+2\overline{\Omega}_X f/r \tag{3.10}$$

Applying equilibrium condition (3.4), we obtain,

$$k_BT\ln(\frac{a_{X^{n+}}}{\overline{a}_{X^{n+}}})=\frac{2\gamma\langle\Omega\rangle}{r}+\frac{2f(\overline{\Omega}^X-\langle\Omega\rangle)}{r} \tag{3.11}$$

If we envision the M_aO_n as a M-M_aO_n "alloy" and oxygen as a "substitutional" component in the lattice, the equilibrium condition of reaction (c) is,

$$k_BT\ln(\frac{M^{n+}}{\overline{M}^{n+}})=\frac{2\gamma_{M_aO_n/M}\langle\Omega_{M_aO_n/M}\rangle}{r}+\frac{2f_{M_aO_n/M}(\overline{\Omega}_{M_aO_n}-\langle\Omega_{M_aO_n/M}\rangle)}{r} \tag{3.12}$$

In this expression, the subscript M_aO_n/M refers to the oxide-covered particle.

Since the addition of reactions (a) and (c) yields (b), the equilibrium condition for equation (b) would be the addition of equilibrium conditions for (a) and (c), which is,

$$\begin{aligned}&E_{M_aO_n/M}(r)-\overline{E}_{M_aO_n/M}\\&=\left[\frac{\gamma_{M_aO_n/M}\langle\Omega\rangle_{M_aO_n/M}}{nq}+\frac{f_{M_aO_n/M}}{nq}\left(\overline{\Omega}_{M_aO_n}-\langle\Omega\rangle_{M_aO_n/M}\right)-\frac{\gamma_M\Omega_M}{nq}\right]\left(\frac{2}{r}\right).\end{aligned} \tag{3.13}$$

Equations (3.8) and (3.13) give the size-dependent standard equilibrium potentials of reactions (a) and (c). Based on these equations, the size dependent potential-pH diagrams can be constructed if the parameter values in the equations are available.

For the case of Pt, the electrochemical and chemical equilibrium equations for bulk solid are:

(A) $Pt^{2+} + 2e^- = Pt$

$$E_{Pt/Pt^{2+}} = 1.188 + 0.0295\log(Pt^{2+})$$

(B) $PtO + 2H^+ + 2e^- = Pt + H_2O$

$$E_{Pt/PtO} = 0.98 - 0.059pH$$

(C) $PtO + 2H^+ = Pt^{2+} + H_2O$

$$\log(Pt^{2+}) = -7.06 - 2pH$$

To get the corresponding equilibrium equations for particles, several parameters are needed. γ_{Pt} , $\gamma_{PtO/Pt}$ and f_{Pt} generated by first principle calculations can be obtained from publications [41–43]. The $f_{PtO/Pt}$ was measured by a technique described in a prior publication by our group[44].

Assuming the concentration of Pt^{2+} in the electrolyte is 10^{-6} M and using the parameters given in Table 3.1, equation (3.8) and (3.13) can be numerically written as

$$E_{Pt/Pt^{2+}} = 1011 - 113(2/r_m); r(nm). \tag{3.14}$$

$$E_{PtO/Pt} = 980 - 59pH - 21(2/r_m); r(nm). \tag{3.15}$$

In pH~1 electrolyte, equation (3.15) becomes

$$E_{PtO/Pt} = 922 - 21(2/r_m); r(nm). \tag{3.16}$$

Figure 3.1 is the E-pH diagram of Pt with different sizes generated using the equations (3.14) and (3.15). Figure 3.2 shows the size dependent equilibrium potential in pH~1 electrolyte.

Table 3.1 Parameter values used in the evaluation of $E_{Pt/Pt^{2+}}$ and $E_{PtO/Pt}$ for Pt particle.

Parameter	value	Method and Measurement
γ_{Pt}	2.4 J/m^2	First Principles Calculation [41]
$\gamma_{PtO/Pt}$	0.5 J/m^2	First Principles Calculation [43]
f_{Pt}	5.6 J/m^2	First Principles Calculation [42]
$f_{PtO/Pt}$	3.0 J/m^2	Measured by wafer curvature
Ω_{Pt}	9.09×10^{-6} m^3	Unit cell
Ω_{PtO}	14.9×10^{-6} m^3	Unit cell [45]
$\langle \Omega_{PtO/Pt} \rangle$	10.7×10^{-6} m^3	Mean value for a Pt particle 2-5 nm in radius

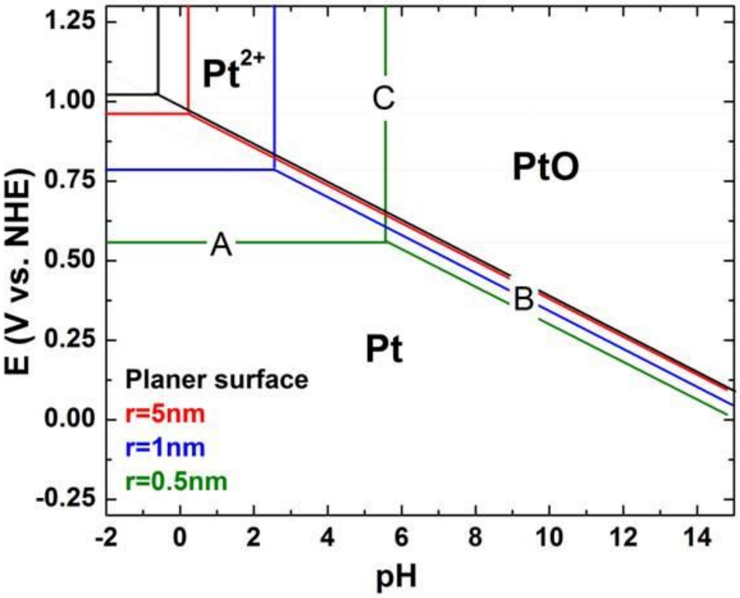

Figure 3.1. Particle-size dependent E-pH diagram for Pt/10^{-6}M Pt^{2+} [46].

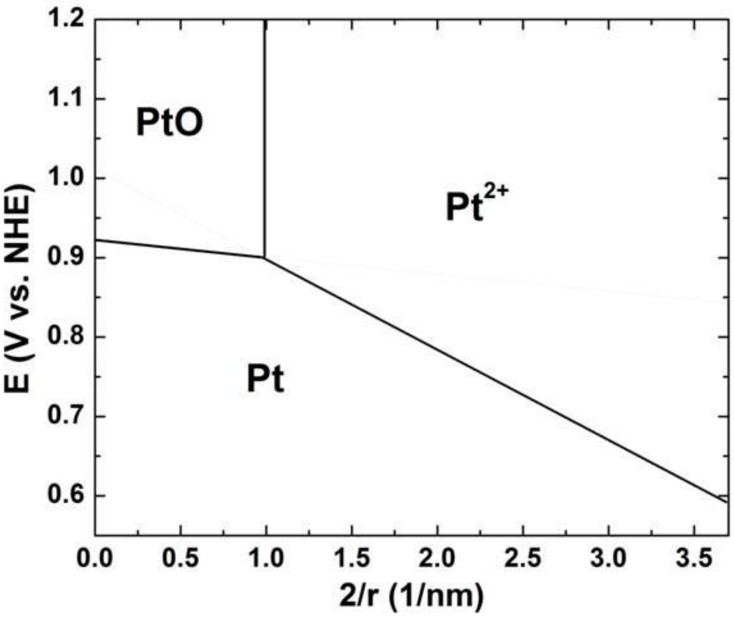

Figure 3.2. Stability of Pt particles in pH~1 electrolyte containing 10^{-6} M Pt^{2+} showing the different dissolution mechanisms for different particle sizes.

Similarly, the E-pH diagram and size dependent electrochemical equilibrium diagram for Cu and Ag could be plotted. Assuming the concentration of Cu^+ or Ag^+ in the electrolyte is 10^{-6} M and using the parameters given in Table 3.2 for Cu, equation (3.8) and (3.13) can be numerically written as

$$E_{Cu/Cu^+} = 0.16 - 0.144 \times (2/r_m); r(nm). \tag{3.17}$$

$$E_{Cu_2O/Cu} = 0.471 - 0.059pH + 0.071 \times (2/r_m); r(nm). \tag{3.18}$$

While for Ag, the equations can be written as

$$E_{Ag/Ag^+} = 0.44 - 0.133 \times (2/r); r(nm). \tag{3.19}$$

$$E_{Ag_2O/Ag} = 1.173 - 0.06pH + 0.123 \times (2/r); r(nm). \tag{3.20}$$

Table 3.2. Parameter values used in the evaluation of equilibrium potential of Cu.

Parameter	value	Method and Measurement
γ_{Cu}	1.95 J/m^2	LDA Calculation [41]
γ_{Cu_2O}	0.8 J/m^2	First Principles Calculation [47]
f_{Cu}	1.95 J/m^2	LDA Calculation [48]
$f_{Cu_2O/Cu}$	1.0 J/m^2	Estimate
Ω_{Cu}	7.1×10^{-6} m^3	Unit cell
Ω_{Cu_2O}	23.4×10^{-6} m^3	Unit cell [49][47]
$\left\langle \Omega_{Cu_2O/Cu} \right\rangle$	1.4×10^{-5} m^3	Mean value for a 2-5 nm Cu particle in diameter

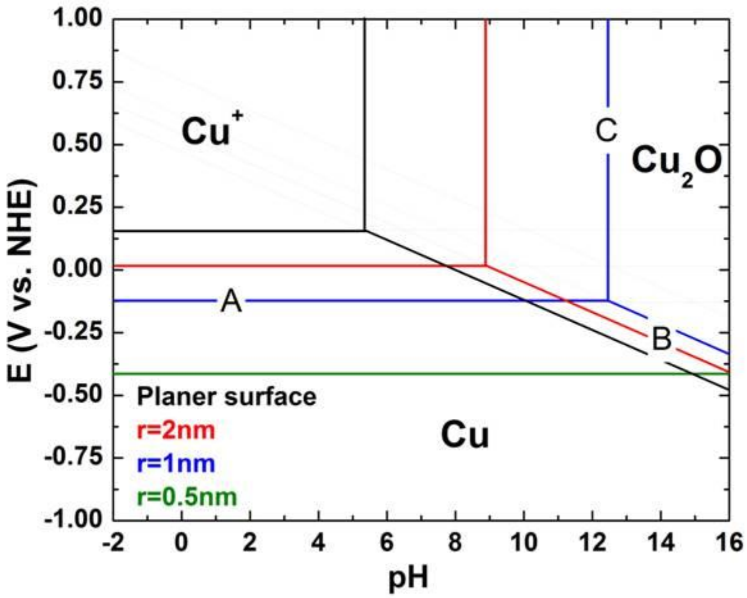

Figure 3.3. Particle-size dependent E-pH diagram for Cu/10^{-6}M Cu$^+$.

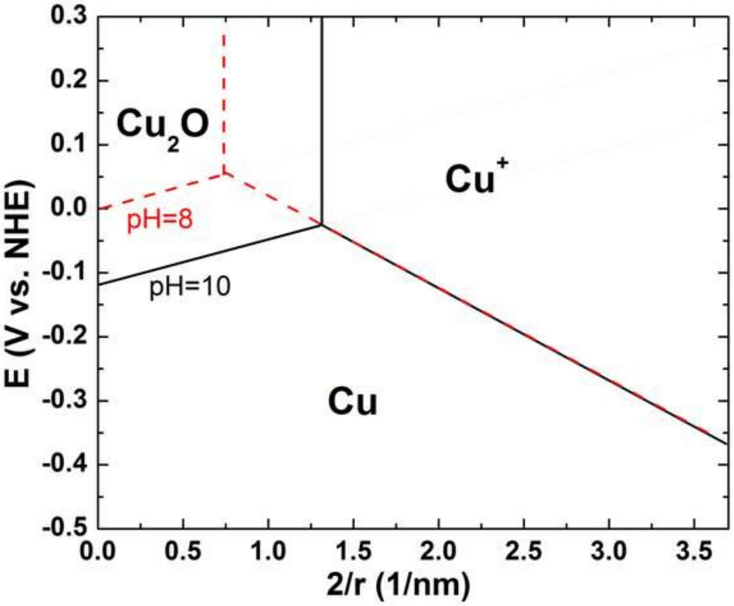

Figure 3.4. Stability of Cu particles in pH = 10 (solid lines) and pH = 8 (green dash lines) electrolyte containing 10^{-6} M Cu$^+$.

Table 3.3. Parameter values used in the evaluation of equilibrium potential of Ag.

Parameter	value	Method and Measurement
γ_{Ag}	1.25 J/m^2	DFT Calculation [50]
γ_{Ag_2O}	0.5 J/m^2	Estimate
f_{Ag}	1.7 J/m^2	[51]
$f_{Ag_2O/Ag}$	1.0 J/m^2	Estimate
Ω_{Ag}	10.27×10^{-6} m^3	Unit cell
Ω_{Ag_2O}	31.6×10^{-6} m^3	Unit cell [49]
$\langle\Omega_{Ag_2O/Ag}\rangle$	15.5×10^{-6} m^3	Mean value for a 2-5 nm Ag particle in diameter

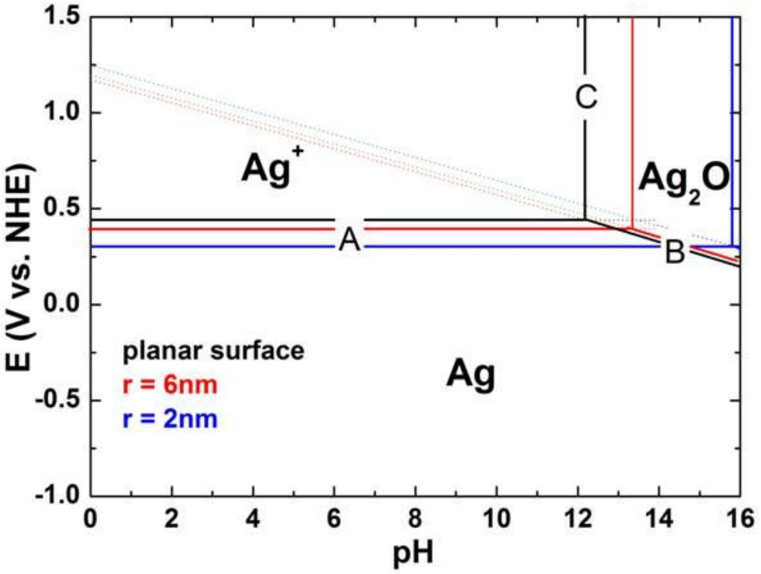

Figure 3.5. Particle-size dependent E-pH diagram for Ag/10^{-6}M Ag^+.

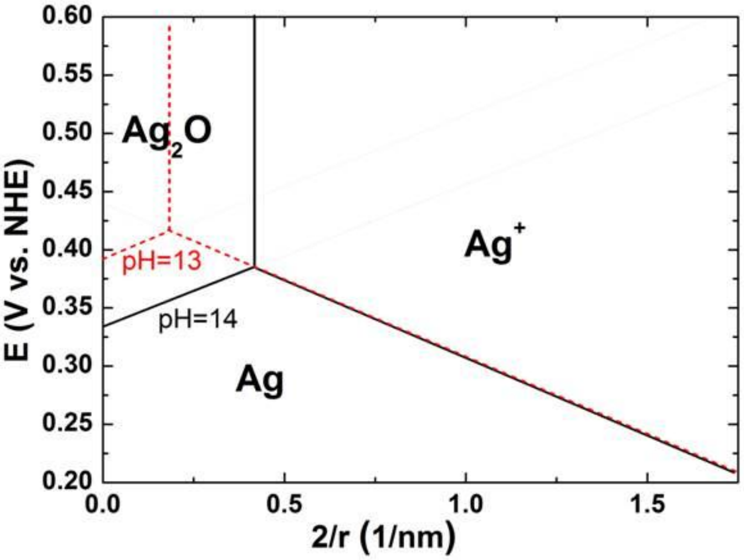

Figure 3.6. Stability of Ag particles in pH=14 (black lines) and pH=13 (red dash lines) electrolyte containing 10^{-6} M Ag^+.

3.2 Experiment

The electrochemical stability of individual Pt particles with a radius in the range of 0.6 – 1.5 nm has been investigated using Electrochemical Scanning Tunneling Microscope (ECSTM) in a prior paper by our group [36]. The results fit well with the theoretical anticipation. Here we carried out a similar set of experiments over a larger range of particle size [46].

The working electrolyte used for the ECSTM experiment was 0.1 M H_2SO_4 (GFS Chemicals, VERITAS® DOUBLE DISTILLED), which was prepared using Barnstead Nanopure (18 MΩ cm) water. A freshly prepared hydrogen loaded palladium wire was used as a reference electrode. All potentials quoted unless otherwise noted are with respect to the reference electrode. The stability of the reference electrode was checked against a MSE and was found to be better than ±10 mV over 24 hours. The counter electrode was a Pt wire.

$Au_{0.95}Ag_{0.05}\{111\}$ film was used as substrate for the particles in ECSTM experiments. The particles in the solution were diluted in isopropyl alcohol and sprayed onto a fresh $Au_{0.95}Ag_{0.05}$ film. The concentration of the particles was adjusted to get ~ 20 particles in a 100×100 nm area.

3.3 Result and analysis

Figure 3.7 shows a series of ECSTM images of Pt particles on $Au_{0.95}Ag_{0.05}$ $\{111\}$ surface in an air saturated 0.1 M H_2SO_4 solution. The starting voltage on the working electrode was 550 mV and the particles were stable for more than 30 minutes of scanning which implied that tip induced dissolution effects was not an observable phenomenon in this experiment. Then the potential was increased in a stepwise fashion by 50 mV increments until 1.2 V and held for several scans at each potential. Finally the potential was pulsed back to 650 mV. The potential-time protocol of the experiment is shown in Table 3.4. All the images shown in Figure 3.7 correspond to the last scan at that potential. Figures 3.8-3.11 show the zoomed views of frame 1-4 of Figure 3.7. Smaller particles almost always disappeared in one scan (~150 s) while larger particles survived for much longer times. It was observed that the dissolution potential of the particles increased with increasing particle size for particles larger than ~ 2 nm in radius, which is expected to be the boundary of two different dissolution mechanisms. As shown in Figure 3.7, the largest particles still present even after ~ 30 minutes at 1200 mV. It was observed that the particle 3 in Figure 3.11 developed well-defined facets during dissolution which can be explained that this family of step orientations has the lowest energy and therefore dissolves slowest.

Table 3.4. Potentials hold times for the ECSTM experiment

Voltage (V, vs NHE)	Hold Time (min)
0.7	4
0.75	4
0.8	4
0.85	5
0.9	15
0.95	17
1.0	13
1.05	40
1.1	58
1.15	28
1.2	33

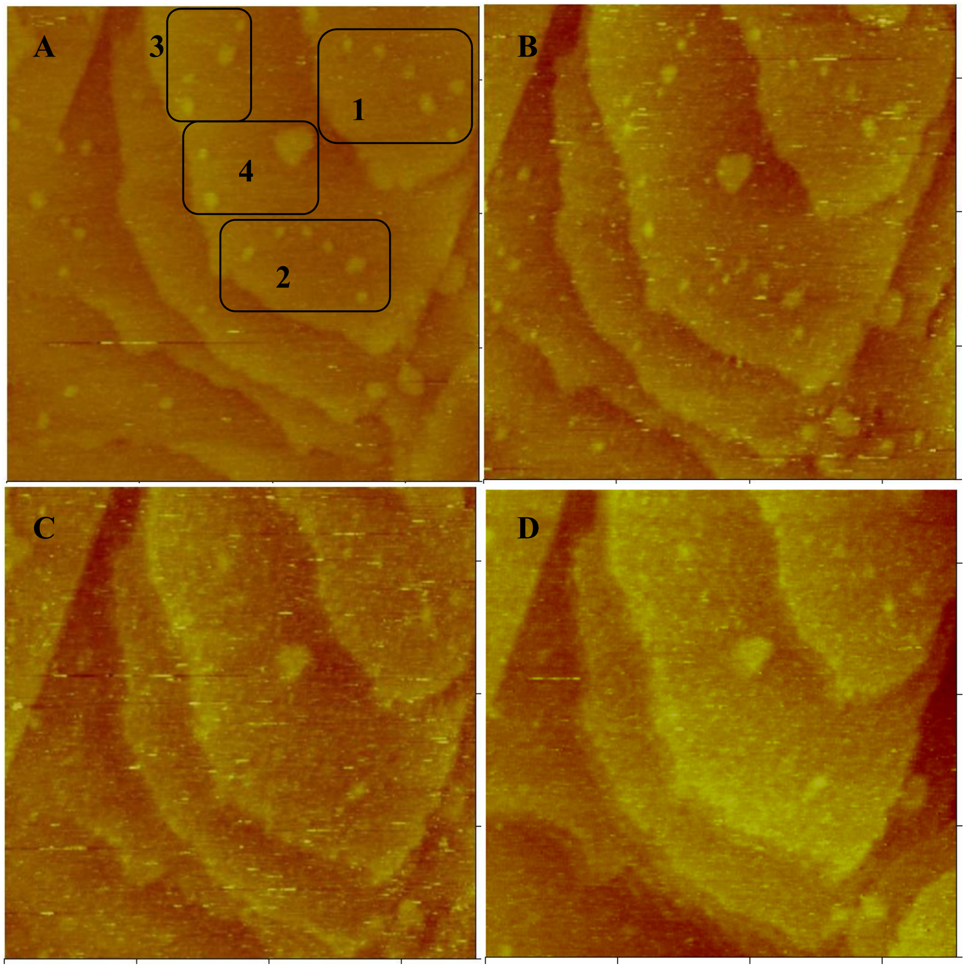

Figure 3.7. ECSTM topographic height mode images showing Pt-black particles on $Au_{0.95}Ag_{0.05}$ {111} surface in 0.1 M H_2SO_4. Images show the sample over a scan size of 178 ×178 nm at potentials of (A) 650 mV. (B) 950 mV. (C) 1200 mV and (D) 650 mV after the potential step protocol shown in Table 3.4.

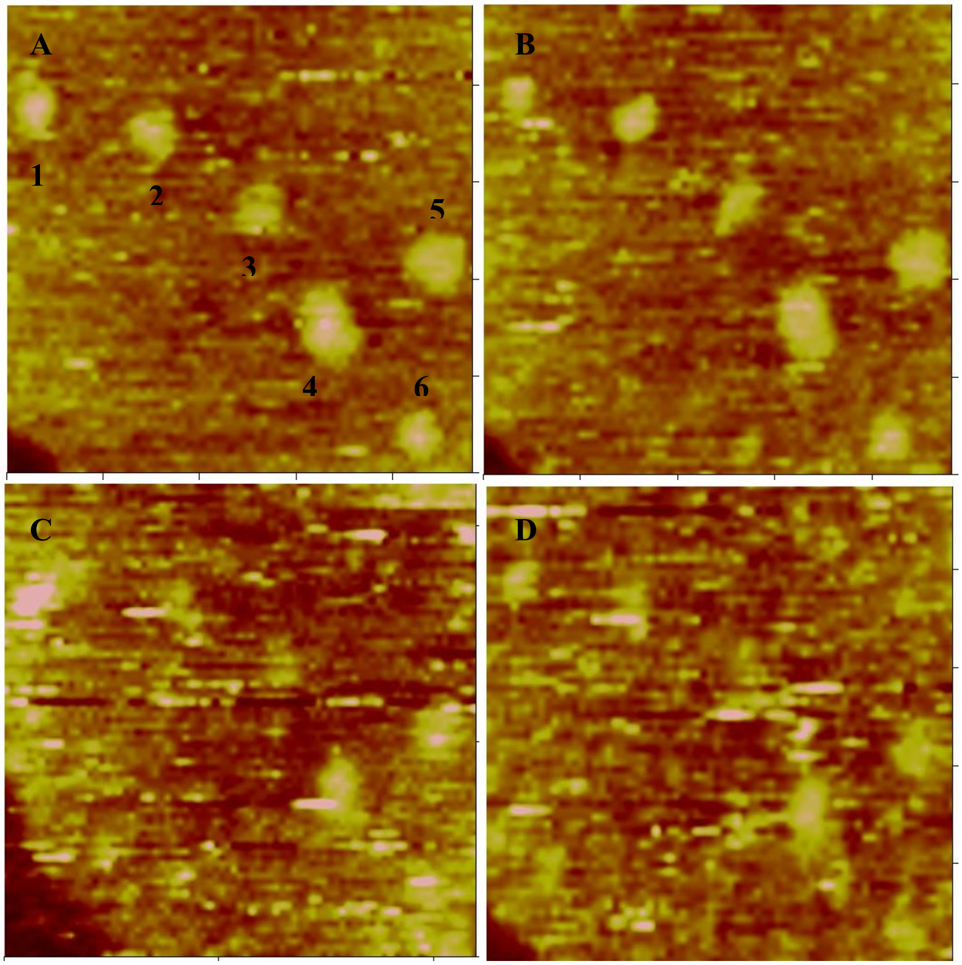

Figure 3.8. Zoomed images of the frame 1 in Figure 3.7. Scan size 50 ×50 nm. (A) 650 mV: The mean radii of the particles present in this image are: particle 1, r_m = 2.05 nm; particle 2, r_m = 2.33 nm; particle 3, r_m = 2.21 nm; particle 4, r_m = 3.08 nm; particle 5, r_m = 2.70 nm; particle 6, r_m = 2.10 nm. (B) 900 mV: Particles 1 and 3 are dissolving. (C) 1100 mV: Particles 1, 2, 3 and 6 are almost gone. Particle 4 is becoming smaller. (D) 1200 mV: Particle 5 is much smaller than original size.

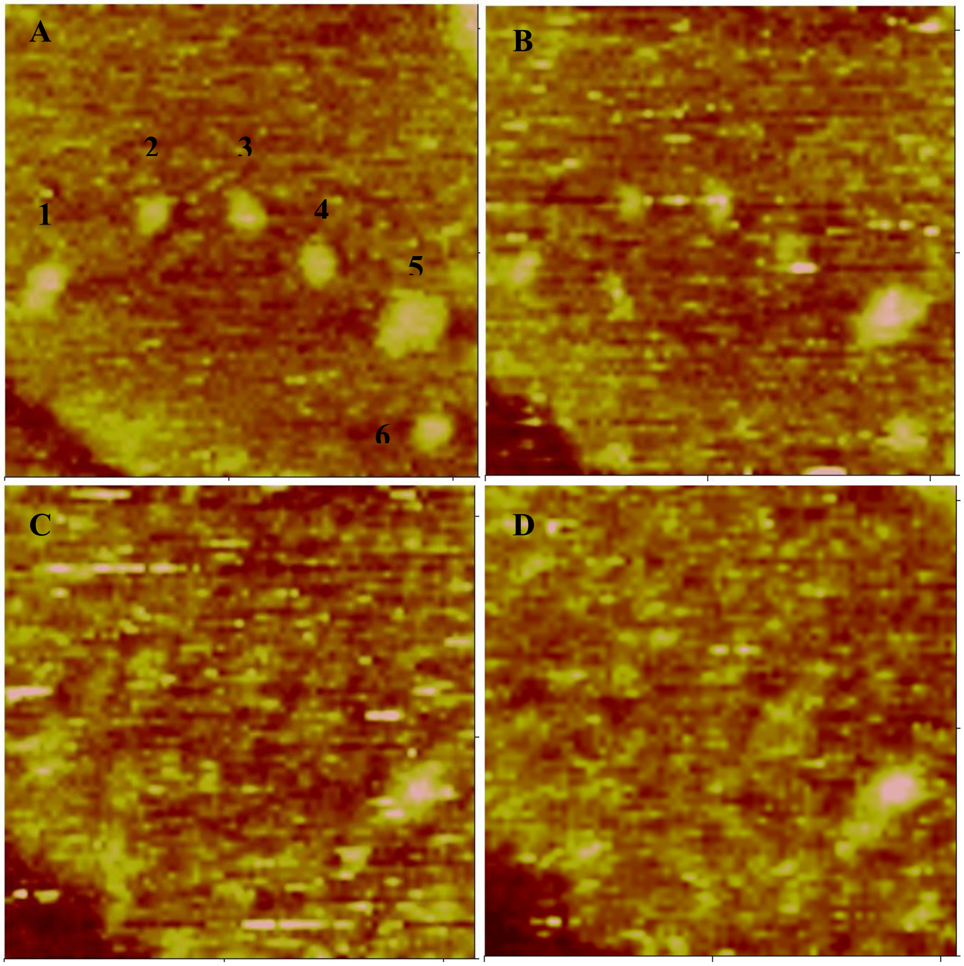

Figure 3.9. Zoomed images of the frame 2 in Figure 3.7. Scan size 52 ×52 nm. (A) 650 mV: The mean radii of the particles present in this image are: particle 1, r_m = 2.22 nm; particle 2, r_m = 1.90 nm; particle 3, r_m = 2.10 nm; particle 4 r_m = 2.13 nm; particle 5, r_m = 3.27 nm; particle 6, r_m = 1.94 nm. (B) 1000 mV: Particles 1-4 are dissolving. (C) 1200 mV: Particle 5 is becoming smaller. (D) 650 mV: Particles 1, 2, 3, 4 and 6 are almost gone.

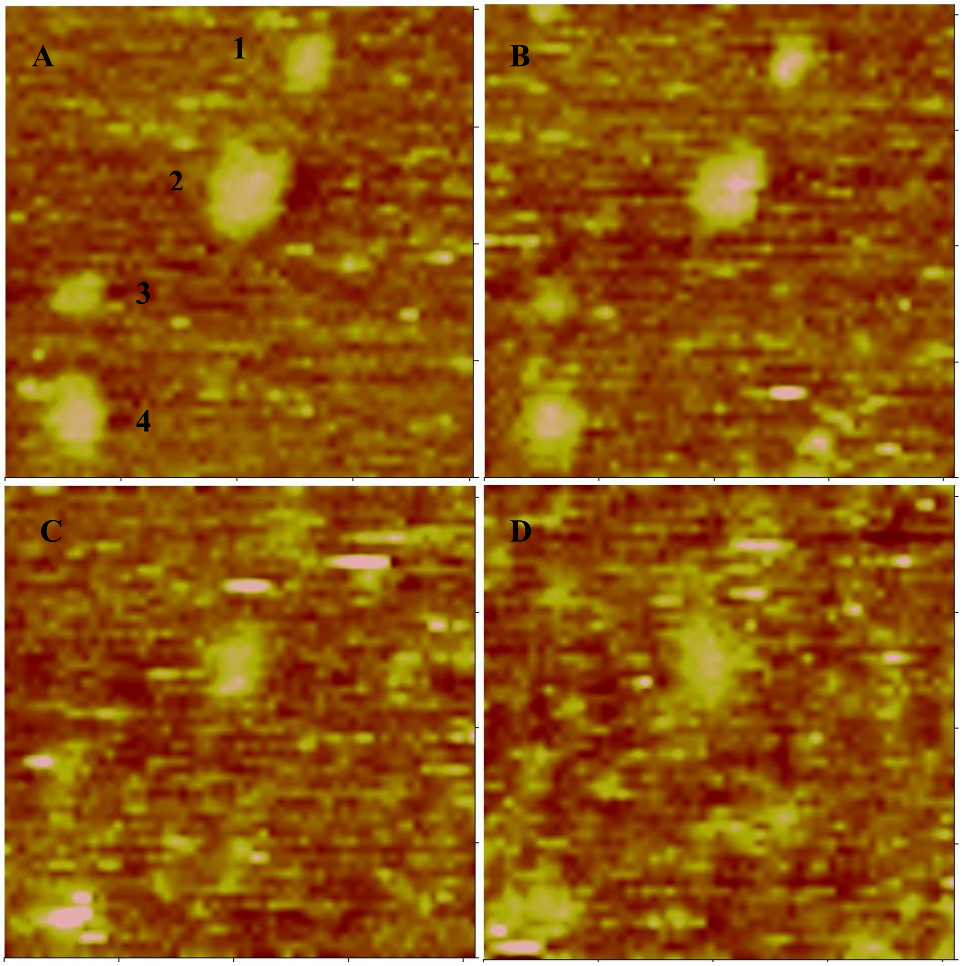

Figure 3.10. Zoomed images of the frame 3 in Figure 3.7. Scan size 41 × 41 nm. (A) 650 mV: The mean radii of the particles present in this image are: particle 1, r_m = 2.08 nm; particle 2, r_m = 3.23 nm; particle 3, r_m = 1.96 nm; particle 4, r_m = 2.80 nm. (B) 900 mV: Particles 1 and 3 start dissolving while 2 and 4 are stable. (C) 1100 mV: Particles 1 and 3 disappear. Particles 2 and 4 are becoming smaller. (D) 1200 mV.

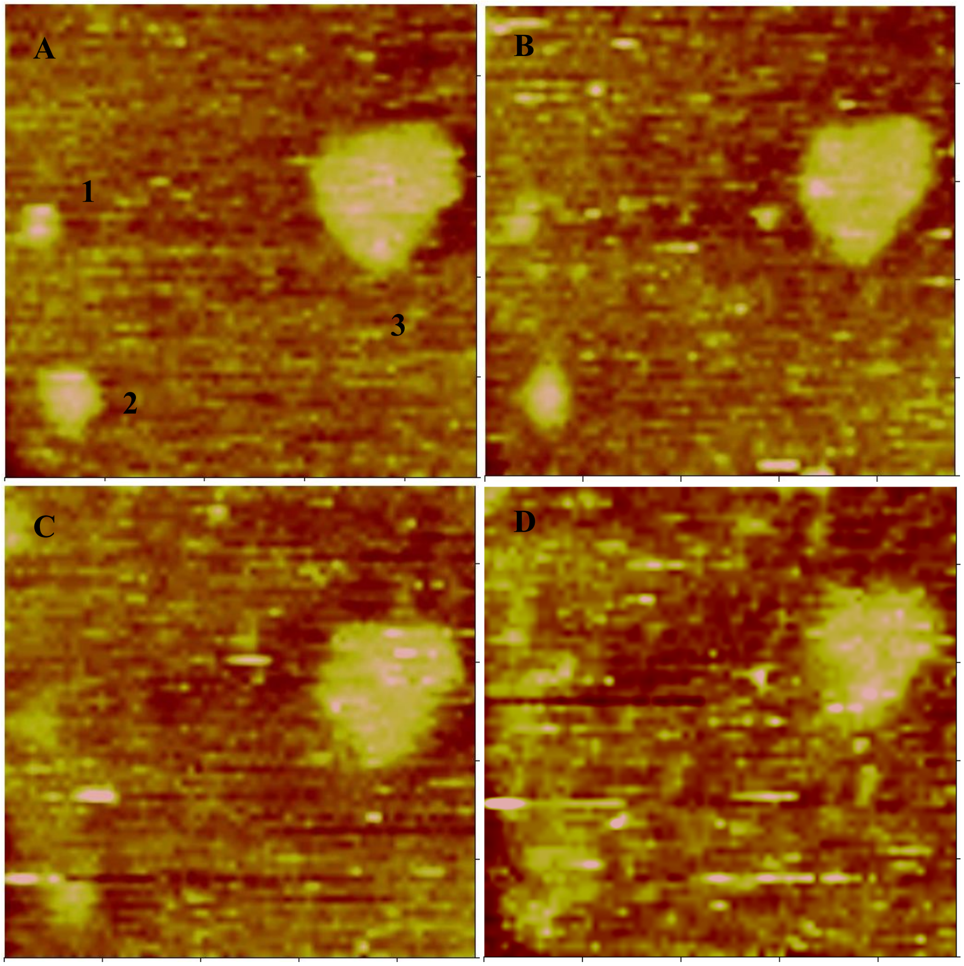

Figure 3.11. Zoomed images of the frame 4 in Figure 3.7. Scan size 48 × 48 nm. (A) 650 mV: The mean radii of the particles present in this image are: particle 1, r_m = 1.88 nm; particle 2, r_m = 2.79 nm; particle 3, r_m = 7.2 nm. (B) 950 mV: Particles 1 and 2 are dissolving while no obvious change for particle 3. (C) 1050 mV. (D) 1200 mV: particles 1 and 2 have disappeared while particle 3 is still present.

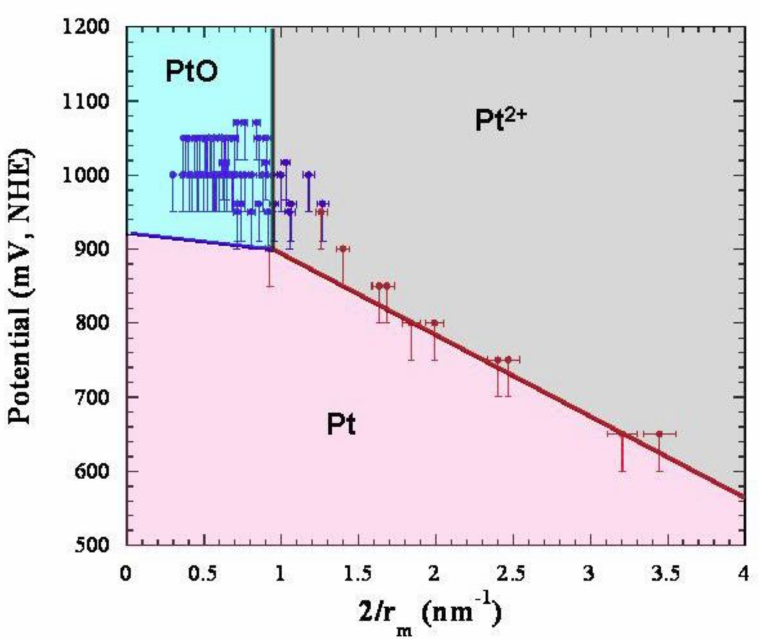

Figure 3.12. Influence of the Pt particle size ($2/r_m$) on the dissolution and oxidation potentials. A linear fit to the data (red points) yields $V_{diss} = 1051–122(2/r_m)$ which should be compared to equation (3.14). The blue points correspond to those particles that formed an oxide and followed a chemical dissolution route.

Figure 3.12 shows the influence of particle size on dissolution and oxidation potentials. The blue and red spots correspond to the experiment data and the lines correspond to equation (3.14) and equation (3.16). The data set from our prior publication [36] is also included in this figure. Particle radius were calculated by $2/r_m=1/r_1+1/r_2$, in which r_m is the mean radius of the particle, and r_1 and r_2 correspond to half the length of the major and minor axis of the ellipsoid-shaped particle measured by STM software. The potential at which there was an obvious size decrease for the particle was recorded to be the dissolution potential. It can be seen that the experiment result agrees well with the thermodynamic prediction. Several potential sources of errors are discussed as follows.

The major source of experimental error results from determining the oxidation potential of large particles. In our data analysis, we assume that the potential at which a particle gets smaller is strongly correlated to the oxidation potential given by equation (3.16), however, this is only valid when chemical dissolution is not a rate-limiting step, which means PtO dissolves chemically as soon as it is formed. So the potential at which obvious size change is observed corresponds to an upper bound for the oxidation potential. According to equation (3.12), the solubility of PtO for a r_m = 6 nm particle in a pH = 1 electrolyte is about 10^{-8} M. For a PtO particle of 2 nm in radius, the solubility is about 10^{-6} M. Assuming there are 30 Pt particles of 3 nm in radius in 180×180 nm area and the particle density is uniform on the substrate, the Pt^{2+} concentration is 3×10^{-7} M if all the particles form oxide and dissolve chemically. This concentration is an upper limit because the oxide only forms on the surface for a lot of particles. It is apparent that the larger the particle is, the more difficult the dissolution of the oxide is.

Two other possible sources of error exist in the thermodynamic calculation. One is the accuracy of the first principle calculation for γ_{Pt} , $\gamma_{PtO/Pt}$ and f_{Pt}. Depending on the approximation in the calculation, the results can vary by as much as 15%. The $f_{PtO/Pt}$ is calculated using f_{Pt} and the experimentally measured Δf upon forming a monolayer of PtO on Pt(111). The Δf measurement is within ~10% of that calculated by Feibelman for 1/4 of an adsorbed oxygen monolayer on Pt(111) [52]. The second source of error is from assuming a stoichiometric PtO oxide with a bulk PtO crystal structure. However, the surface energies of various platinum oxide forms are calculated to be 0.5 ± 0.15 J/m^2 [43].

3.4 Summary

The electrochemical stability of elemental metal nanoparticles was studied and presented in this chapter. A thermodynamic derivation based on the Gibbs Thomson equation was carried out on metal particles and particle size dependent electrochemical potential-pH diagram were constructed. Since the construction of E-pH diagram for metal particles needs the data for surface energy and surface stress for metal oxide, which is presently not available for many metals, the E-pH diagram was only constructed for Pt, Ag and Cu particles. Accordingly, the electrochemical stability of Pt particles with a diameter ranging from 1 to 10 nm in 0.1 M H_2SO_4 was experimentally studied by in-situ ECSTM. The experiment results agree well with the thermodynamic expectation. Pt particles of diameter less than ~ 4 nm dissolve via a direct electrochemical pathway, while larger particles form oxide, which chemically dissolves.

Chapter 4

DEALLOYING OF ALLOY PARTICLES

4.1 Background

4.1.1 Dealloying behavior of bulk alloy

Dealloying refers to the selective dissolution of one or more components from an alloy. This process can be electrochemically driven in systems where a large electrochemical potential difference exists between the elemental standard potentials. The voltage onset of the selective dissolution in an alloy is conventionally defined as the critical potential, which marks the transition from a “passivated” alloy surface to selective dissolution. Below the critical potential only surface dealloying occurs and the surface remains macroscopically flat. Above the critical potential the less noble component is selectively dissolved resulting in the production of nanoporous structures with a completely interconnected ligament-void structure as shown in Figure 4.1 [5]. Initially, nanoporous structures were observed in stress corrosion cracking [14,15]. Later, interests extended to the creation of skeletal structures for advanced applications [10–13,53–56]. It is recognized today that selective dissolution results in nanoporosity formation in many alloy systems [8,15,57–60].

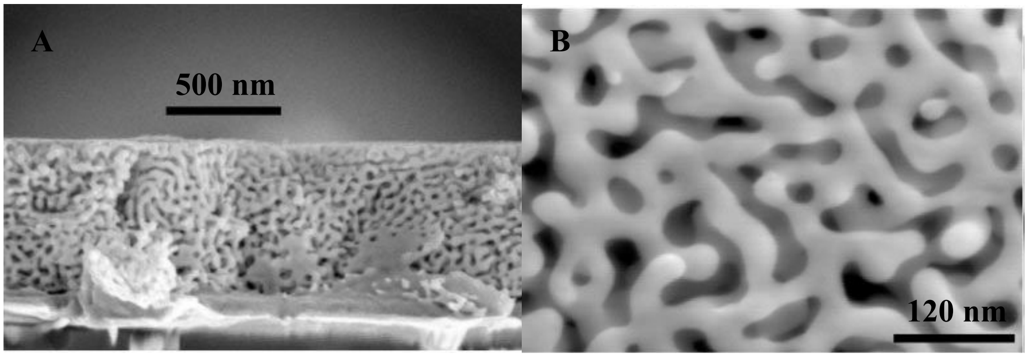

Figure 4.1. SEM images of nanoporous gold made by selective dissolution of silver from AgAu alloys: (A) Cross-section of dealloyed AuAg thin film; (B) Plan-view of dealloyed AuAg [5].

Experimentally, there are two typical ways to determine the critical potential, which are, polarization and the current decay method. In the polarization method, the critical potential is determined as the potential corresponding to a fixed, (arbitrarily) prescribed current density by analyzing the electrochemical polarization data. A schematic illustration of a polarization curve for dealloying is shown in Figure 4.2. In polarization data since the critical potential is associated with the knee in the curve, it can be seen that this is not sharply defined. The shape of the knee is affected by sweep rate, alloy, and electrolyte composition. The ambiguity in defining a critical potential is further shown in Figure 4.3.

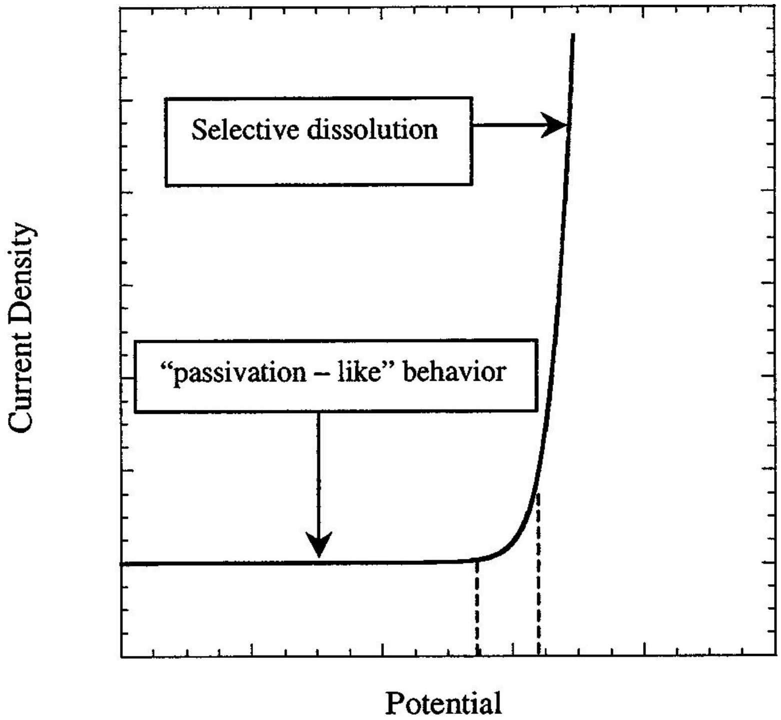

Figure 4.2. Schematic illustration of the polarization behavior of dealloying. The current rise is not sharp which results in ambiguity in the determination of the critical potential [6].

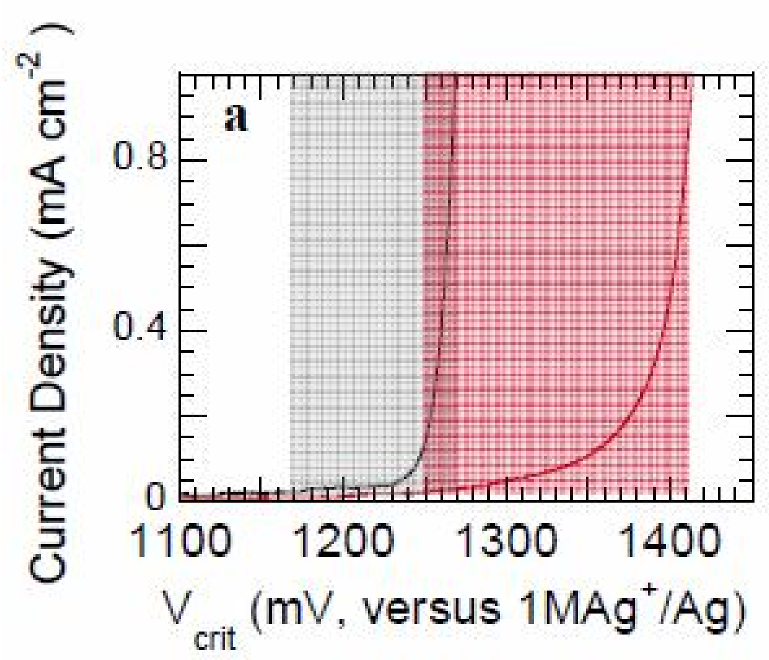

Figure 4.3. Current-voltage behavior for the dealloying of a $Ag_{0.72}Au_{0.22}$ alloy in an electrolyte containing 1 M dissolved Ag^+ (black line) and 0.001M Ag^+ (red curve). The shaded regions correspond to the range in critical potentials that can occur depending on how V_{crit} is measured [9].

For the current decay method, the critical potential represents the potential marking the transition from current decay to steady-state current in a series of potential hold measurements. Corcoran has done some systematic work on determining the critical potential for AuAg and PtCu alloys using this method [8,61]. The SEM images of the dealloyed surface showed that porosity could be formed when the dealloying potential is above the critical potential determined by current decay. Figure 4.4 is an example of the current decay experiment for $Ag_{0.7}Au_{0.3}$ alloy. Table 4.1 compares the critical potential measured by current decay method and polarization method. Column 1 is determined by measuring the potential necessary for the current to reach a value of 1.0 mA/cm^2 [6] and column 2 gives the critical potential values as determined by the potential hold data [61]. It can be seen that the current decay method provides a more conservative determination of the critical potential. The critical potential measured by polarization method can be 200-300 mV higher than that found by the current decay method.

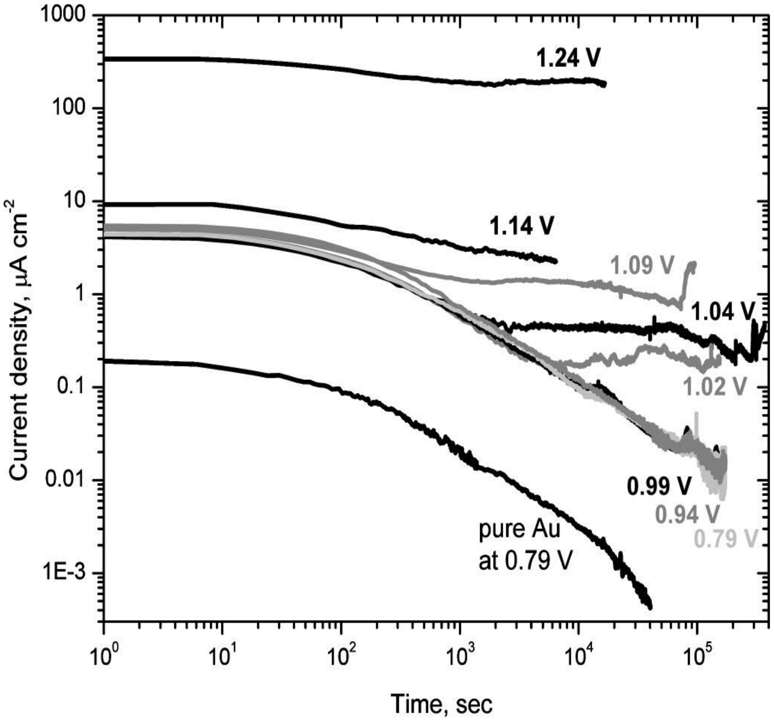

Figure 4.4. An example of the current decays method showing current response of $Ag_{0.7}Au_{0.3}$ in 0.1 M $HClO_4$ held at the indicated potentials [61].

Table 4.1. Critical potential values (V vs. NHE) vs. alloy composition determined by the indicated methods [61].

Alloy composition	Ecrit(Fixed current)	Ecrit (Potential hold)
$Ag_{80}Au_{20}$	1.09	0.79~0.82
$Ag_{75}Au_{25}$	1.16	0.93~0.94
$Ag_{70}Au_{30}$	1.22	0.99~1.02

In an ideal A_pB_{1-p} binary alloy where A is the less noble element, the dissolution of A on the surface results in vacancy cluster formation. The initial size of the vacancy cluster is determined by an intrinsic length scale which is given by $\xi_a = a(1+p)/(1-p)$, where a is the nearest neighbor spacing [62]. Thermodynamically, dealloying starts from the dissolution of the largest less noble metal clusters on the surface of a solid solution alloy. Assuming the void-cluster is a cylindrically shapped "pit", the dissolution overpotential would be

$$\Delta V = V_{crit} - V_{A/A^+} = 4(\gamma_{B/elec} - \gamma_{B/A})\Omega / nq\xi_a - kT \ln a_A \tag{4.1}$$

This number should be a lower limit for bulk dealloying. Considering the case for a AuAg alloy in the composition range of 70%~95% Ag, $\gamma_{Au/elec} >> \gamma_{Au/Ag}$ and $kT\ln a_{Ag}$ is in the range of 0-20mV. The critical potential is plotted vs. the reciprocal of the intrinsic size of Ag clusters in Figure 4.5.

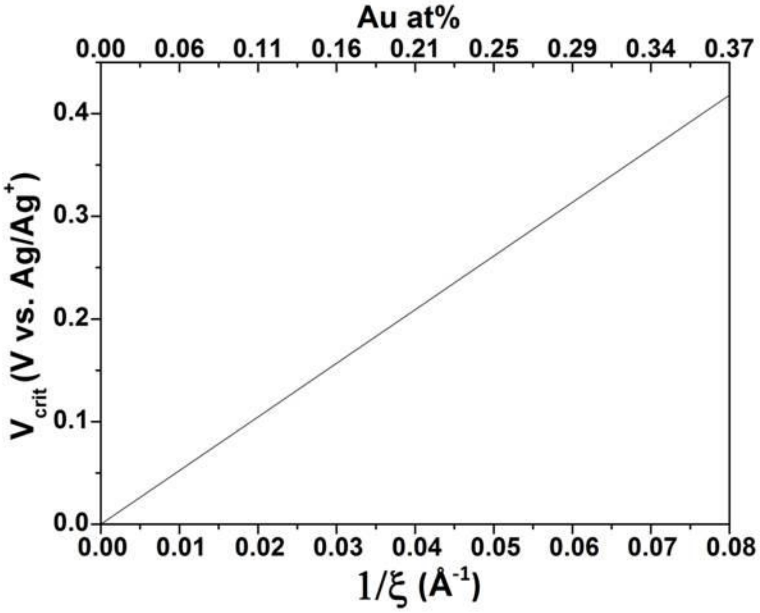

Figure 4.5. V_{crit} as a function of inverse length scale for the AuAg alloy. For $Au_{20}Ag_{80}$ alloy, the overpotential is ~0.2V vs. Ag/Ag^+. If assuming $[Ag^+]$ is 10^{-6} M, the critical potential would be 0.64 V.

To describe and explain the dealloying process, a kinetic model was developed to calculate the critical potential by Sieradzki [6]. It is believed that critical potential results from a competition between dissolution of the less noble component, (which results in surface roughening porosity formation), and surface-diffusion induced smoothening of the more noble component (assumed to be potential independent which causes the surface to passivate). The critical overpotential, $\eta_{crit} = E_{crit} - E$, for selective dissolution of A is given by [6]

$$\eta(p)_{crit} = \frac{4}{\xi_a}\delta + \frac{2k_BT}{nq}\sinh^{-1}\left(\frac{\pi^2}{nq\delta}\frac{D_sN_s\gamma\Omega}{J_0}\frac{1}{\xi_a^2}\right), \tag{4.2}$$

where ξ_a is the intrinsic length scale, $\delta = \beta - \gamma\Omega / nq$ is the coefficient of a composition modulated curvature effect in which β is a measure of a local composition fluctuation, D_s is the surface diffusivity and N_s is the number of atoms per unit area. The first part of Equation (4.2) represents the dissolution overpotential resulting from a local composition modulated curvature effect, which is a thermodynamic term. The second part corresponds to the kinetic overpotential, related to diffusional covering.

The microscopic detail of porosity formation during dealloying was modelled by kinetic Monte Carlo simulations which incorporated site coordination-dependent surface diffusion of all alloy components and site coordination-dependent dissolution of the less noble atoms [63]. The type of atom is assigned in a 3D lattice at random based on a probability determined by the composition. The time evolution of the system is governed by the KMC algorithm. If there are N total events that can occur and the rate constant is k_i for the i^{th} event, then there would be a finite probability of an event occurring in a period of time. The simulations progress by picking a random event according to its probability and then the time in the simulation advanced according to the rate constant of that event. In the dealloying process of a AuAg alloy, two events are considered: the diffusion of the two types of atoms and dissolution of less noble atoms. The rates of diffusion and dissolution of an atom with n neighbors are expressed as:

$$k_n^{diffusion} = \upsilon_D \exp(-nE_b / k_B T) \tag{4.3}$$

$$k_n^{dissolution} = \upsilon_E \exp(-(nE_b - \phi) / k_B T) \tag{4.4}$$

where E_b is near-neighbor bond energy, ϕ is the dissolution potential, υ_D and υ_E are the attempt frequencies. E_b is set as 0.15 eV, υ_D is 10^{13} s^{-1} and υ_E is 10^4 s^{-1}. Assuming the exchange current for $Ag/10^{-6}Ag^+$ is 0.1 mA/cm^2, the "standard" potential of Ag/Ag^+ sits near 0.7 eV.

This model successfully reproduced the classical phenomenology of dealloying, such as the polarization curve behavior and porosity formation above the critical potential. However, since the dissolution rate is expressed as an exponential function of the potential instead of the hyperbolic sine behavior of the Butler-Volmer (BV) equation, this expression is only valid in a potential range away from the equilibrium potential. The critical potential is defined as the potential at which there is a continuous steady dissolution flux and corresponding porosity formation. Figure 4.6 shows the critical potential ranges determined by simulations at different compositions.

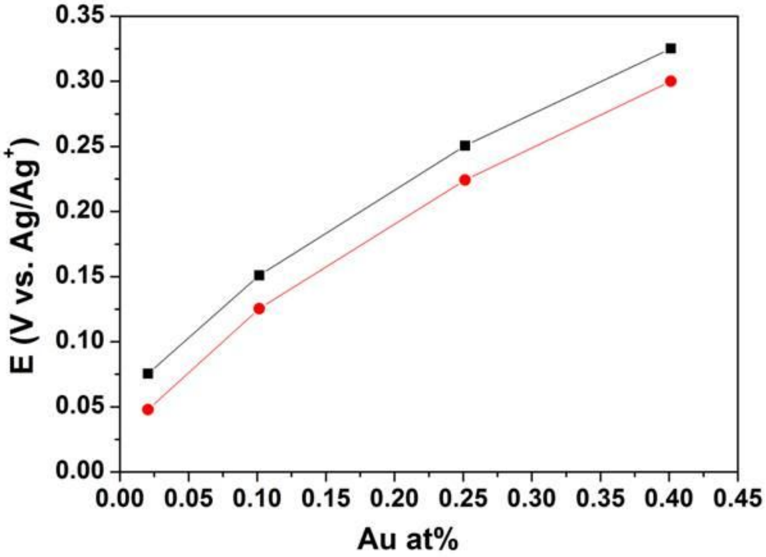

Figure 4.6. Critical potential vs. alloy composition by current decay method. The black squres correspond to the upper bound for the critical potential above which porosity forms. The red round dots corresponds to the lower bound below which the surface passivates [63].

4.1.2. Dealloying behavior of alloy nanoparticles

As described previously, there we two particle size ranges examined in our experiments. For particles between 20 nm to 100 nm at which Gibbs-Thomson effect is not observable, the dealloying behavior is expected to be similar to bulk materials. For a size range between 2 nm to 10 nm in diameter, the crystal structure is still identical to the corresponding bulk solid and quantum size effects are not apparent [64,65].

The difference between chemical potentials of the liquid and solid phase for substitutional specie in a finite size multi-component solid has been shown in equation (3.11) in Chapter 3. For A_pB_{1-p} binary alloy, component A can be envisioned as a substitutional specie, so the difference between equilibrium potential for in nanoscale and that for bulk is given by

$$E(r) - \overline{E}(\infty) = \frac{k_B T}{nq} \ln(\frac{a_{A^{n+}}}{\overline{a}_{A^{n+}}}) = \frac{2\gamma_{alloy} \langle \Omega \rangle_{alloy}}{nqr} + \frac{2 f_{alloy} (\overline{\Omega}_A - \langle \Omega \rangle_{alloy})}{nqr}. \quad (4.5)$$

Here f_{alloy} is the surface stress of the alloy, γ_{alloy} is the solid/liquid interfacial free energy, $\langle \Omega \rangle_{alloy}$ is the average atomic volume of the solid, and $\overline{\Omega}_A$ is the partial atomic volume of the A component in the alloy. This equilibrium potential corresponds to the surface dealloying potential in nanoscale structures.

"Bulk" dealloying at the nanoscale, it is still an open question. Firstly, since smaller particles have a larger specific area, (e.g. ~200 atoms on the surface out of 300 atoms in total for a particle of 1nm in radius), it is expected that the dealloying behavior is more like surface dealloying and the dealloying potential will be closer to the thermodynamic equilibrium potential for the less noble metal. Secondly, as particle size goes down, the diffusion term that was negligible for the case of bulk AgAu alloys may contribute significantly to surface passivation, owing to the lower melting point for nanoparticles [21]. The melting point for a gold particle with 3 nm in diameter is about 70% of the melting point for bulk gold. The surface diffusivity of the bulk gold is about 10^{-18} m^2/s in 0.5 M H_2SO_4 in air [66], while the diffusivity of 3 nm gold particle is about 10^{-14} m^2/s because of the melting point reduction. Curvature effect for nanoparticles facilitates the dissolution of Ag, while the higher diffusivity of Au in nanoparticles accelerates the surface passivation process. Thirdly, the intrinsic length scale defined in percolation theory is also size-dependent [62], which might have an effect on the dealloying parting limit and critical potentials.

KMC simulations were also applied to examine the dealloying behavior of nanoparticles [67]. The particles with 4~17 nm in diameter in the composition range between 65% and 85% Ag were examined. It was found that as the electrochemical potential increased, the propensity for porosity evolution increased. The critical potential was “defined” as the potential at which the probability of getting a porous particle was ~50%. It was explained that the diffusion induced passivation became more dominant as the particle size decreases, so the porosity evolution actually required a higher electrochemical potential.

There have been several groups that have published some experimental results about Pt alloy nanoparticle dealloying [17,18,63–69]. In most papers, before the chemical or electrochemical dealloying, the alloy nanoparticles are annealed, forming a surface segregated Pt layer. Different composition and morphologies of the dealloyed products are reported depending on the size and the composition of the alloy nanoparticles. When the composition of the less noble metal is lower than 50% ~ 60%, only surface dealloying occurs and core-shell structures finally form [73]. In the case of Pt alloy particles, when the composition of the less noble metal is higher than some threshold composition, a porous structure is observed for particles larger than 10 nm in diameter, and core-shell structure is observed for smaller particles [17,68,72,74]. The pore size is about 1~2 nm for Pt based alloy particles and coarsens to about 3~5 nm after extended voltage cycling. The residual composition of the less noble metal after dealloying is generally lower for the porous structure than the core-shell structure [73].

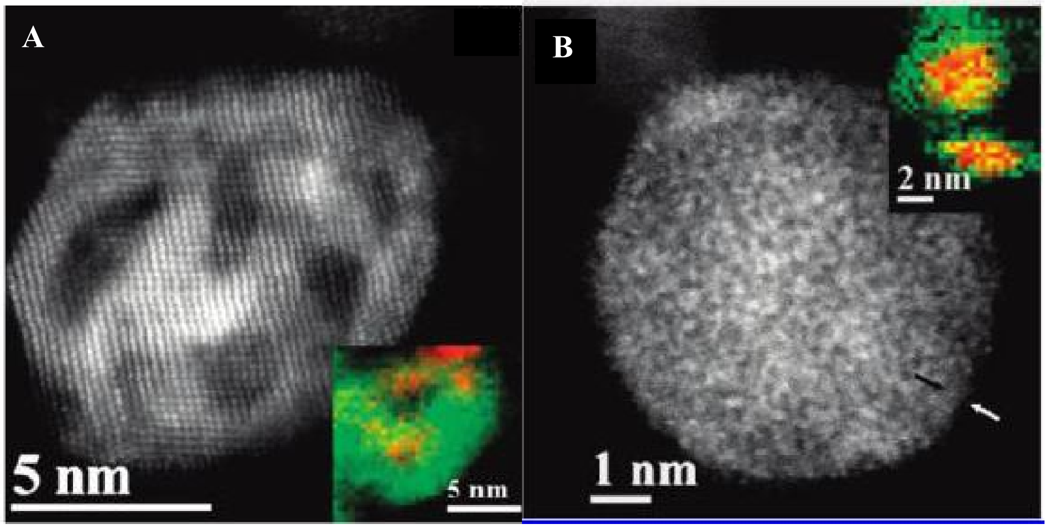

Figure 4.7. (A) Porous structure of a dealloyed PtCu particle (~12nm in diameter) and corresponding EELS map. The green color corresponds to Pt and the red color corresponds to Cu. The contrast differences in the HAADF image on the particle could result from atomic number difference or thickness difference. However, the contrast differences couldn't be so large if there was only composition variation. So, it is considered that this is a porous structure. (B) Core-shell structure of a dealloyed PtCu particle (~ 8nm in diameter) and corresponding EELS map [68].

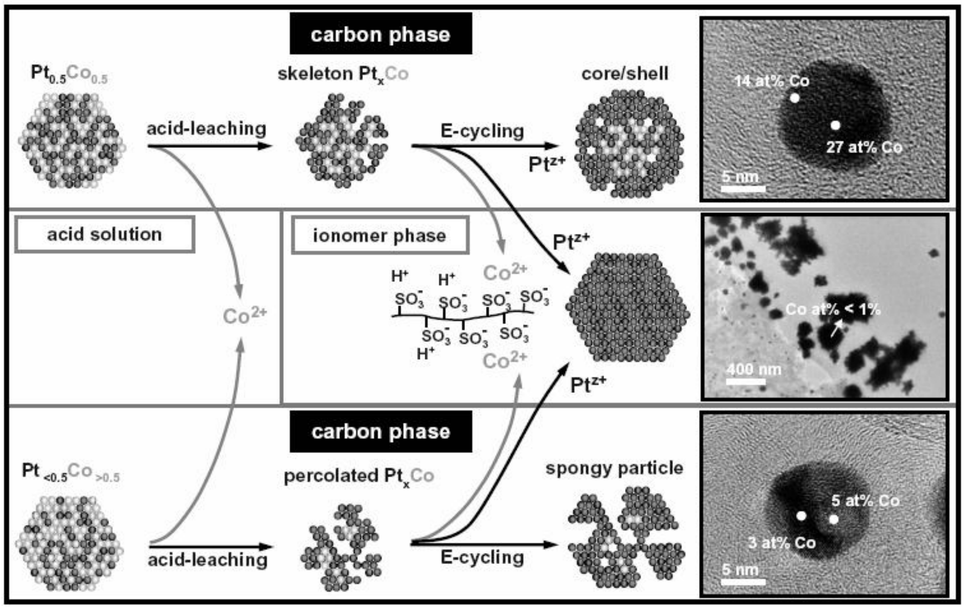

Figure 4.8. Schematic description of the evolution in morphology and composition of a $Pt_{0.5}Co_{0.5}$ cathode catalyst caused by acid leaching and voltage cycling. The upper panel represents skeleton Pt_xCo particles obtained after acid leaching and transforming via Ostwald ripening into core/shell particles. The lower panel is a proposed mechanism for the formation of percolated Pt_xCo alloy particles deriving from precursors with higher than average Co content ("$Pt_{<0.5}Co_{>0.5}$") and resulting in Pt-rich spongy particles. TEM bright-field images and spot-resolved EDS compositions of the various types of aged nanoparticles are shown on the right-hand side [73].

4.1.3. Nanoparticle Synthesis

Particle synthesis and properties have been well documented in many review articles [75–80]. In principle, there are two different approaches to synthesize nanocrystals: the "top-down" approach, which utilizes physical methods, and the "bottom-up" approach, which employs solution-phase colloidal chemistry [78]. Most physical methods have advantages in obtaining nanoparticles with high purity while it is hard to get uniform size particles. The chemical methods, based on solution-phase colloidal chemistry, can be used to obtain nanoparticles with narrow size distribution and well-controlled shape. However, in order to get isolated stable nanoparticles, this kind of method always needs protective coating shells which must be removed in order to interrogate their electrochemical behavior. The representative chemical methods for metal nanoparticle synthesis are: chemical reduction of metal salts, electrochemical reduction and controlled decomposition [81].

The chemical reduction of the metal salts in solution is the most widely practiced synthesis method. Common reducing agents used include alcohols, sodium citrate, sodium borohydride and hydrogen. Because of the large specific surface area for small size particles, a surface stabilizer is needed to avoid particle agglomeration. Basically, depending on the interaction between the particles and the capping layers, the stabilization can be achieved by three methods: electrostatic stabilization (such as sodium citrate), steric stabilization (vinyl polymers, such as PVP and PVA), and ligand molecules (amines, phosphines, thiols) forming covalent interactions with particles.

The electrochemical reduction usually contains two steps. Firstly, metal ions are formed by anodic dissolution. Secondly, the metal ions are reduced at the cathode, where nucleation and growth occur. Capping agents are also needed to get stable particles with well controlled sizes [75].

The controlled decomposition method is based on the fact that some organometallic compounds can decompose thermally to their respective metals under relatively mild conditions. For example, the thermolysis of precursors such as palladium acetate, palladium acetylacetonate and platinum acetylacetonate in high-boiling organic solvents such as methylisobutylketone can generate organosols of palladium and platinum [81].

4.2 Dealloying of 4nm AuAg alloy nanoparticles

Two directions of study were carried out for the dealloying behavior of small AuAg alloy particles: in-situ ECSTM experiments and ex-situ dealloying experiments. For the in-situ experiment, similar experimental protocols as that conducted on Pt particles was carried out. Successively higher potentials were applied on alloy electrodes and ECSTM images were taken to record the size and morphology change of the particles at different potentials. The dealloying potential corresponded to the potential at which the electrode changed size. For ex-situ experiments, dealloying was carried out by chronoamprometry. The dealloyed sample was then characterized using electron microscopy, EDX and EELS, and compared with the original particle size and composition.

4.2.1 AuAg alloy nanoparticle fabrication and synthesis

4.2.1.1 Nanoelectrode fabrication by drilling holes

The first method that was tried to fabricate nanoelectrodes for in-situ ECSTM experiments is a physical method that was developed based on a technique introduced by a group in Delft University of Technology [82,83]. Briefly, nano-sized holes were drilled in silicon nitride (SiN) membrane followed by vacuum-based metal deposition from the bottom. Then SiN was removed afterward and nanoelectrodes were generated. Figure 4.9 is a schematic diagram of this fabrication technique. The detailed experiment process is shown as follows.

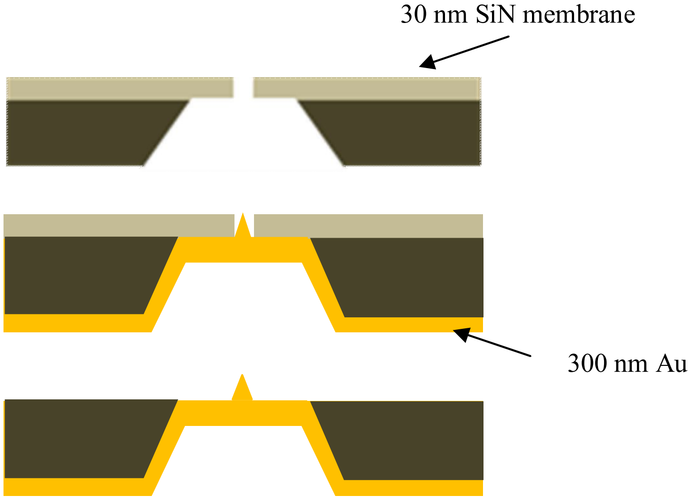

Figure 4.9. Main steps of the nanoelectrode fabrication. (A) Hole drilling in the SiN membrane with a focused electron beam; (B) E-beam deposition of gold on the bottom-side; (C) Dissolution of SiN layer by HF.

First, nano-holes were drilled in a 30 nm thick commercial SiN membrane provided by Norcada Inc. Although thinner commercial SiN membranes are available, these starting surfaces are always warped or wavy which makes AFM imaging on those films nearly impossible. Roughness of the SiN film was checked in AFM and the largest fluctuation was less than 0.5 nm. Nanopore fabrication was carried out using a JEOL 2010F field-emission TEM. To get an intense enough electron-beam intensity, the highest extraction voltage (7.6 kV) and the largest spot size (spot size 1) were used with the condenser aperture retracted. Hole-sizes from 2 nm to 50 nm as shown in Figure 4.10 can be generated by adjusting the beam intensity and the time of stay. The holes arrays were then imaged in AFM as shown in Figure 4.11(A).

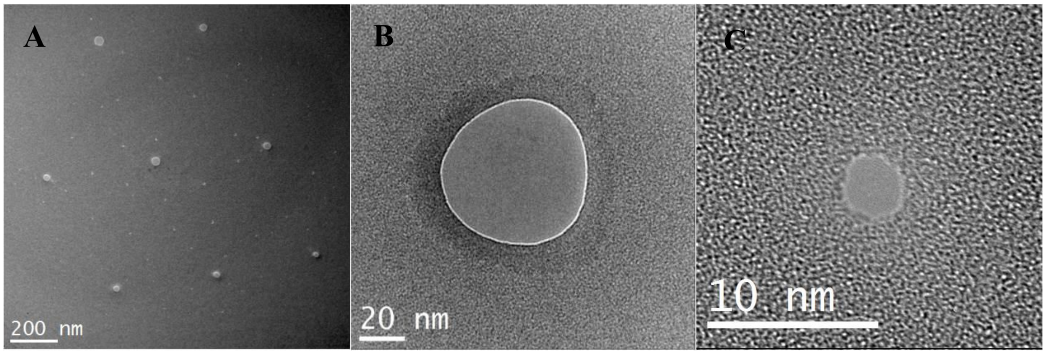

Figure 4.10. TEM images of nanopores in SiN membrane. (A) An array of holes. (B) Hole size is 60 nm in diameter. (C) Holes size is 3 nm in diameter.

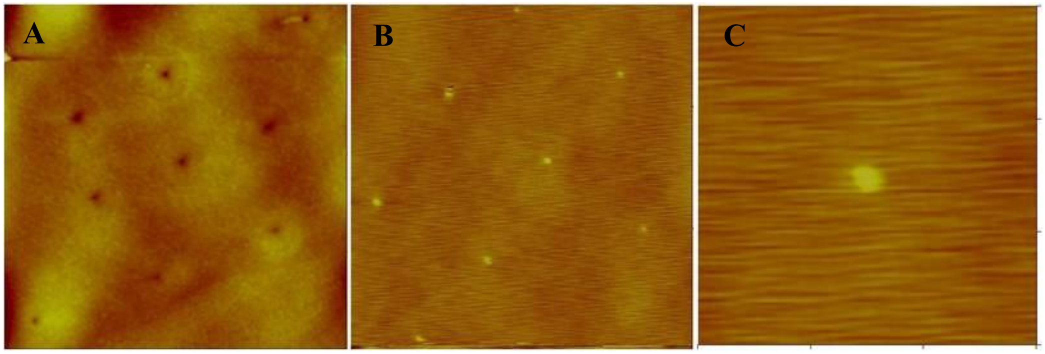

Figure 4.11. (A) AFM topography image of the nanopores before deposition. Scan size 3.5 × 3.5 µm. (B) AFM topography image of the nanoelectrodes after deposition and SiN removal. Scan size 2.8×2.8 µm. (C) Zoomed image of one electrode in (B), Scan size 600×600 nm.

According to Krapf's paper, sputtering Au to cover one side of a pore results in an inverted pyramid geometry [83]. The top side of the pore was covered by a 0.35 nm Cr adhesion layer followed by a 150 nm Cu by e-beam evaporation. It was expected that a Cu pit structure similar to reference [83] could be obtained. Next the membrane was turned over and a 0.35 nm Cr layer followed by a 150 nm Au was deposited from the back side of the membrane. The base pressure of the e-beam evaporization was 10^{-7} Torr. Finally, the Cu layer was dissolved by HNO_3. The sample was then checked in AFM, however, the nanoelectrode structures reported by Krapf were not found on our samples and only holes were seen. At first, it was thought Au did not penetrate through the holes, however, even for 50 nm holes, no electrode was seen in AFM. It was guessed that maybe the Cu layer did not form a concave structure, while instead, it partially filled the holes. So the step of Cu deposition on the top side was discarded and only a 0.35 nm Cr layer followed by a 150 nm Au was deposited from the back side of the membrane. Then the SiN membrane was removed by HF acid. After that, the sample was examined in AFM and arrays of nanoelectrodes were visible as shown in Figure 4.11(B) (C).

Since the hole-array was located in about 1×1 μm^2 area on a TEM grid, it was difficult to locate it and engage the tip in our STM system. However, this would be a very promising technique for fabricating nanoelectrodes for in situ ECSTM experiment to study the dealloying behavior in nanoscale once we have the STM system equipped with the optical positioning system to locate the position of the electrode. Although there are lots of challenges for this technique, such as fabricating smaller electrode, how to remove the SiN film without dealloying the alloy electrode, and whether one can deposit an alloy film that is strong enough after removing the SiN and at the same time is transparent in TEM, there are still many advantages. The size and position of the electrode is well controlled. The electrical contact is much better than nanoparticles “soft landed” on a surface. The electrodes are quite reproducible. What is most important is that a post mortem analysis of the composition and morphology could be done on those fixed nanoelectrodes.

4.2.1.2 Chemical synthesis of nanoparticles and characterization

Adenosine triphosphate (ATP) coated AuAg alloy nanoparticles were synthesized by coreduction of the corresponding salts in aqueous solvent developed by Buttry D [84]. Chloroauric acid ($HAuCl_4$) and Silver nitrate ($AgNO_3$) were used as precursors of the particles. Sodium borohydride ($NaBH_4$) was used as reducing agent and ATP was added as a capping material. The molar ratio of precursors : capping : reducer was 1:1:16.7 which gave the best particle size distribution. The molar concentrations of $HAuCl_4$ and $AgNO_3$ were calculated based on the solubility of AgCl ($K_{sp} = 1.8\times10^{-10}$) to avoid the AgCl precipitation during synthesis. For $Au_{25}Ag_{75}$ particle, $HAuCl_4$ (3.87×10^{-7} mol), $AgNO_3$ (1.16×10^{-6} mol) and ATP (1.547×10^{-6} mol) were added to 100 mL nanopure water in flask under bubbling N_2, and the solution was stirred at room temperature for 15 min [84]. Freshly prepared $NaBH_4$ (5 mM, 5 mL) was then quickly added into the flask with continued stirring. The solution immediately changed to a light yellow color. Then the solution was continually stirred and bubbled for 3 hrs to allow for the growth of particles to completion. Since the concentration of the precursors was very low, the particle solution was then concentrated from 100 mL to ~2 mL on a rotary evaporator.

The color of the particle solution is dependent on the composition of the particle. A pure Ag particle solution is light yellow while a Au particle solution shows a wine red color. The color of AuAg particle is yellowish red and becomes deeper for particles containing a higher Au%. The AuAg particle solution was analyzed using Cary 50 Bio UV-Visible spectrophotometer and the UV-vis spectroscopic analysis shown in Figure 4.12 suggested that alloy particles instead of core-shell structure or other segregated structures were formed.

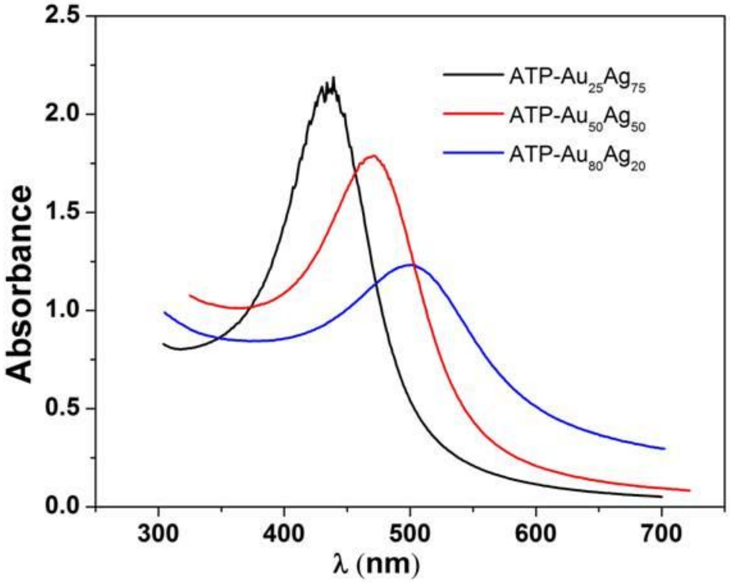

Figure 4.12. UV-vis of ATP coated AuAg nanoparticles with different compositions.

The size distrubution and composition of the particles were characterized by JEOL 2010F. A Cu grid with carbon film (Ted Pella Inc.) was plasma cleaned for 10 s to get rid of the static electricity, and then a 20 uL particle solution was dropped on the grid and air dried. Typical probe currents for EDX analysis are 0.5 nA and 1.0 nA. The imaging mode for the observation of supported nanoparticles is high angle annular dark-field (HAADF) using an efficient, low-noise scintillator-photomultiplier detector. Condenser aperture #1 (120 μm) was used to give more X-ray signal. The X-ray collection angle of the Si(Li) detector is 0.12 sr. To get more X-ray signal, the sample holder was tilted 15 degree towards the detector. To get rid of the C contamination, beam flooding was carried out by showering the sample for about 15 min using a strong beam current (anode extraction voltage: 7.6 kV) in TEM mode at low magnification (3000X) with no condenser aperture. A hard X-ray aperture located between a condenser lens and an objective lens was inserted to adsorb spurious X-rays that generated by high-energy bremsstrahlung X-rays and uncollimated electrons.

Since there are a relatively small number of atoms in one particle (e.g. there are only ~ 500 atoms in a d = 2 nm particle), the generated X-ray signal is extraordinarily weak and long acquisition times are required for high statistical precision. Secondly, beam damage is a serious problem, especially for Ag when a longer collecting time is used. In principle, there are three kinds of beam damage mechanisms [28], which are ionization damage, knock-on damage (or sputtering) and heating. Ionization damage happens when inelastic scattering (mainly ionization) breaks the chemical bonds of the materials. The ionization cross-section increases as the electron energy decreases. Knock-on damage is the displacement of atoms from the crystal lattice which creates point defects. The higher the beam energy, the easier this can happen. The beam damage of AuAg nanoparticles was studied by Braidy [85] and the main damage mechanisms were discussed. It was calculated that the minimal knock-on threshold incident electron energies for Ag and Au are ~127 keV and ~ 216 keV. Their experiment showed that the damage of Ag was almost reduced to zero when the beam energy was lowered from 200 keV to 100 keV with the same current density, so it was concluded that knock-on damage was the main mechanism that caused Ag loss.

The EDX analysis was made by scanning a small raster over a single particle instead of using the spot mode. This scanning mode can reduce the beam damage problems, and sample drift problems could be avoided by adjusting the position of the raster to trace the particle [86]. Because there might be beam damage problems, a sequence of spectra with different collecting times were recorded. HAADF images were taken for each particle both before and after the EDX acquisition to record size change of the particle.

Each EDX spectrum was exported and re-plotted in Origin. The background intensity is found by averaging the bremsstrahlung intensity on the left and right of the characteristic peak, then integrating the intensity in two identical windows on either side of the peak. The peak intensity of Au Lα and Ag Lα peaks were calculated by integrating the number of counts N in the peaks above the background. The intensity errors (defined as the relative deviation of the peak intensity) were calculated by $3\sqrt{N}/N$. Whether the spectrum is good enough to yield a satisfactory quantification is decided by a determination limit [28]:

$$I_{peak} = 50\left\{1 + \left(1 + I_b/12.5\right)^{1/2}\right\} \tag{4.6}$$

In this equation, I_b is the background intensity. Once equation (4.6) is satisfied, the atomic ratio of Ag and Au can be calculated by the Cliff-Lorimer equation [28]:

$$\frac{C_A}{C_B} = k_{AB}\frac{I_A}{I_B}, \tag{4.7}$$

where k_{AB} is called Cliff-Lorimer factor and this number is given by the Genesis EDAX. For thin samples, X-ray fluorescence and absorption effects can be neglected. The errors of the Ag and Au atomic fraction of each spectrum are calculated from the intensity errors.

About 100 EDX spectra were taken for ATP coated AuAg particles. The atomic percent of Au was 24.5% ± 2%, and the dispersion resulting from counting error for each spectrum was within ± 4%.

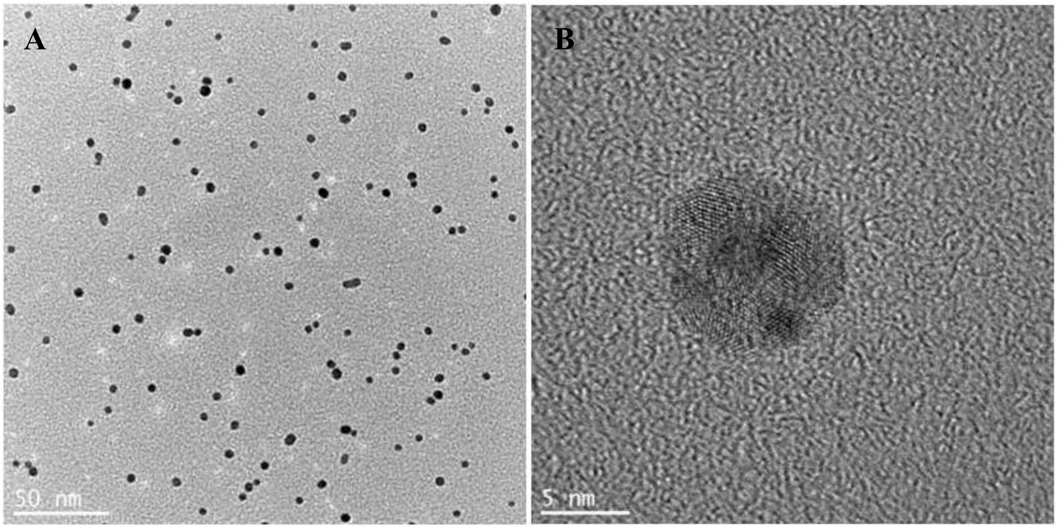

Figure 4.13. TEM images of ATP coated AuAg particles.

4.2.2 In-situ ECSTM experiment of AuAg nanoparticles

The dealloying behavior of chemically synthesized alloy AuAg particles with a diameter of 3~6 nm was studied with in-situ ECSTM in 0.1 M H_2SO_4. Since ATP coated AuAg particles was dispersed in water and the adhesion between particle and Au thin film substrate was not great, the particle might disperse into water when it was exposed to the electrolyte during ECSTM experiment. To avoid this problem, ligand exchange was done to transfer the particles from aqueous to organic phase with a modified method described in literature [87]. Briefly, 0.5 mL dodecanthiol (DDT) and 2 mL acetone were added into 1 mL particle solution. Particles were extracted into DDT by swirling the solution for a few seconds. It could be observed that the color went to the organic phase from the aqueous phase which indicated that particles had been transferred into DDT. Then two phases were separated and the excess DDT in the organic phase was washed by diluting in 1 mL toluene and 3 mL methanol, and then spun down and re-suspended in 1 mL hexane. The TEM and STEM-EDX results showed that there was no observable change on composition for the particles after ligand exchange. The average composition of this batch of particles is 42% Au±3%, and the dispersion resulting from counting error for each spectrum was within ±5%. Figure 4.14 showed the TEM images of the AuAg particles before and after ligand exchange.

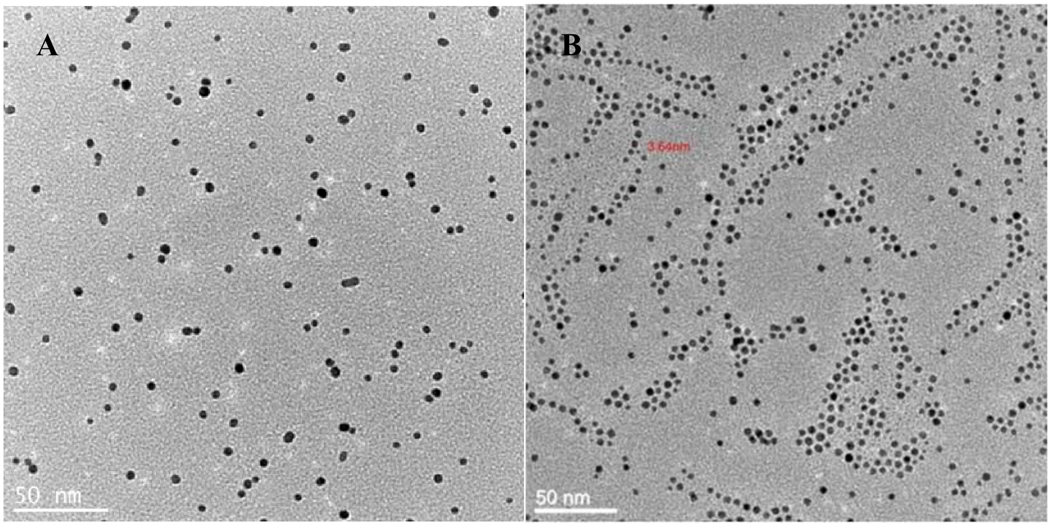

Figure 4.14. (A) ATP coated AuAg particles. (B) DDT coated AuAg particles.

The DDT coated $Au_{40}Ag_{60}$ particles were sprayed onto a piece of Au (111) thin film. Then the thiol coating was removed by either heating in forming gas (N_2/5%H_2) at 250°C for 30 min [88] or reductive desorption in NaOH [89,90]. The dealloying of the particles was examined in an air saturated 0.1 M H_2SO_4 solution with a Pd-H wire as reference electrode by in situ ECSTM. The starting voltage applied on the working electrode was 200 mV vs. NHE. Then the potential was increased in a stepwise fashion by 50 mV increments until 900 mV. Since the particle density was very low, this experiment was carried out on several samples. The ECSTM height mode images at different potentials for one sample were shown in Figure 4.15. Dealloying potential is defined as the potential at which there is an observable size change of the particles and it is plotted vs. the particle sizes including all the experimental data as shown in Figure 4.16.

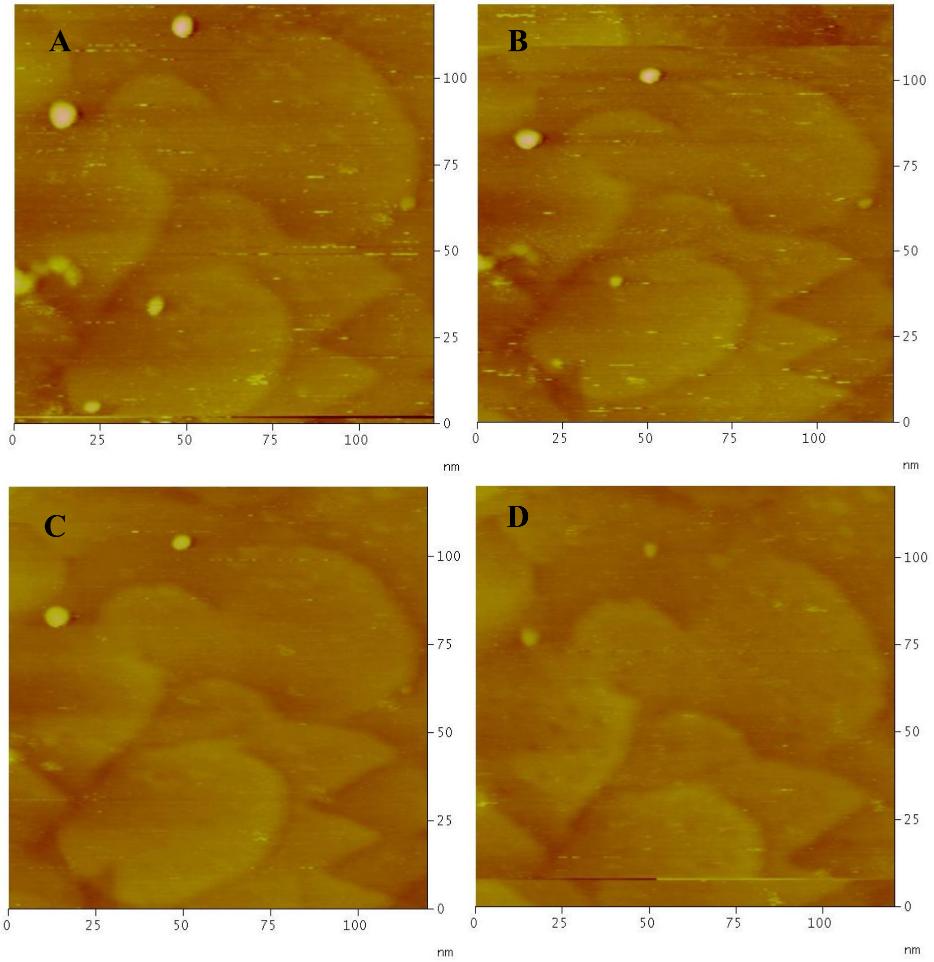

Figure 4.15. ECSTM topographic height mode images showing AuAg particles on Au {111} surface in 0.1 M H_2SO_4. Images show the sample over a scan size of 122 ×122 nm at potentials of (A) 230 mV. (B) 290 mV. (C) 390 mV and (D) 540 mV.

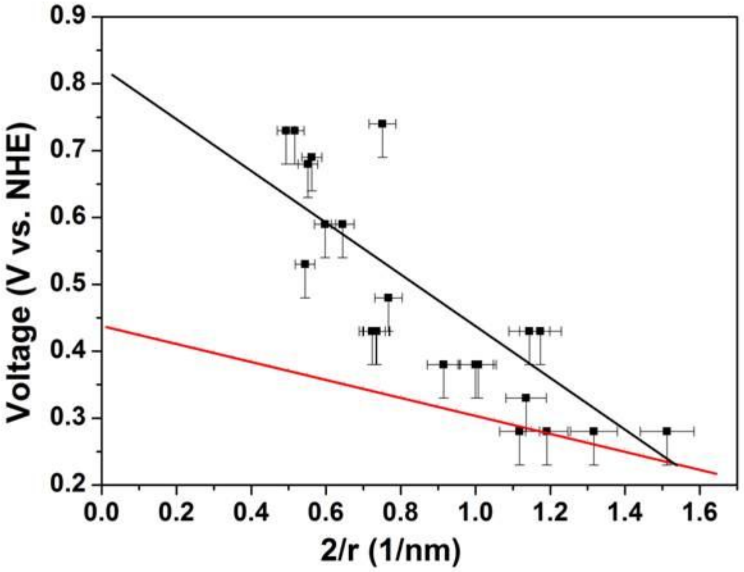

Figure 4.16. Influence of particle sizes on the dealloying and dissolution potentials. Red line: Ag particle dissolution potential with 10^{-6} M Ag^+ calculated by Gibbs Thomson equation, the slope is 0.133 V·nm; Black spot: In-situ ECSTM experimental data for $Au_{40}Ag_{60}$ particle dealloying, the slope is 0.4 V·nm. Vertical error bars correspond to -50 mV, and horizontal error bars indicate measurement errors of ~5%.

According to Gibbs-Thomson equation

$$\Delta V = \frac{2\gamma\Omega}{nqr}, \tag{4.8}$$

in which ΔV is the dissolution potential difference between the bulk alloy and finite size particle, γ is surface energy, Ω is the atomic volume (10.21 cm^3 for Au), q is charge of one electron, n is charge transferred and r is the size of the particles. This equation can be re-written as

$$\Delta V \Big/ \frac{2}{r} = \frac{\gamma\Omega}{nq}. \tag{4.9}$$

For pure Ag particle, $\Delta V \Big/ \frac{2}{r}$ is 0.133 V·nm, which is the slope of the red line in Figure 4.16. While the slope for the dark spots in Figure 4.16 is 0.4 V·nm and the intercept with the y axis is 0.83 V which corresponds to the dealloying potential for the bulk sample. Based on the slope of the fit to the data, the surface energy is 3.78 J/m^2. It can be seen that the dealloying potential of AuAg particle is close to the Ag particle dissolution potential for smaller particles, and the discrepancy becomes larger when the particle size increases. Considering a $Au_{40}Ag_{60}$ particle with diameter of 3 nm, there are 830 atoms in total and 430 atoms are on the surface. Only surface dealloying would make the particle size shrink to ~2.3 nm in diameter. So the potential at which there was observable size change for small particle would be more close to the Ag/Ag^+ equilibrium potential. However, for larger particles, the size change must correspond to a certain degree of bulk dealloying, which happens at least 400 mV higher than the Ag/Ag^+ equilibrium potential for $Au_{40}Ag_{60}$ alloy according to thermodynamic calculation as shown in Figure 4.5.

There are several phenomena that need to be addressed. During the ECSTM experiment, for the particles smaller than 4 nm in diameter, most of them finally disappeared. This may be because that a more open structure was formed during dealloying and the tip effect just accelerated the Au surface diffusion. A comparison experiment was carried out by scanning an area including several particles with the same experimental conditions at 0.2 V for a long time and it was found that the size of the particles also shrank as time increased which should be from the tip effect, however the decay rate was much slower. It is suspected that the size change in a short time during the ECSTM experiment on AuAg particle dealloying should be mainly ascribed to the Ag dissolution, while in a long range of time, the size decay should result from a combination of dealloying and Au atom surface diffusion.

4.2.3 Ex-situ dealloying experiment of AuAg nanoparticles

Chemically synthesized ATP coated AuAg nanoparticles were also used for the ex-situ dealloying behavior study in nanoscale. A TEM grid was used as the substrate for particles in the dealloying experiment since post TEM characterization on the composition and morphology of particles would be carried out and it was not easy to transfer the particles to a TEM sample holder after dealloying. For grid selection, two factors had to be considered. Firstly, the grid must be conductive and stable enough during the particle dealloying experiment. Secondly, to get a reliable EDX result, the X-ray peaks of the grid materials should not overlap with the peaks of Au and Ag from particles. So, Au, Pt and Pd are not good candidates. For W, the Lβ line has some overlap with the Au Lα line. A Ni grid was considered as the best possible substrate. Although the equilibrium potential for Ni is very low, we determined that a Ni grid could survive within a certain amount of time for potential holding since there is an oxide layer on the surface.

ATP coated $Au_{25}Ag_{75}$ alloy nanoparticles with diameter ~4 nm were dispersed on C film coated Ni grid (Pacific Grid-Tech). The dealloying experiment was carried out in 0.1 M H_2SO_4(GFS Chemicals, VERITAS® DOUBLE DISTILLED), which was prepared using Barnstead Nanopure water. MSE was used as reference electrode. All potentials quoted are with respect to the normal hydrogen electrode (NHE). The counter electrode was a PtIr wire. The Ni grid with particles was held on a piece of Au film by Au wires and dipped in the electrolyte. The particles were dealloyed by chronoamperometry with a series of potentials ranging from 0.1 V to 1.4 V. For dealloying at potentials above the open circuit potential of Au substrate (~0.75 V), the dealloying time was 30 s and after that the sample was quickly washed in nanopure water. While for dealloying at potentials lower than the open circuit potential, to avoid the OCP dealloying, the electrolyte was diluted gradually by 10^5 times with nanopure water while the potential was held on the sample. The particles were also dealloyed at 0.9 V with different length of time: 30 s, 2 min and 10 min.

The composition and morphology of the dealloyed particles were checked in TEM and STEM-EDX. There was no observable difference on the composition for the sample dealloyed at 0.9 V for different length of time, which indicates that 30 s is long enough for dealloying the particles ~4 nm in diameter. The average composition of 100 particles on each sample dealloyed for 30 s was plotted vs. the dealloying potential in Figure 4.17 and the error bar for each point corresponds to the standard deviation of the composition analysis. It has been reported that Ag atoms are highly enriched on the surface of AuAg alloy and the atomic percent of Ag on the surface for $Au_{25}Ag_{75}$ alloy could be around 90%~100% [91]. If assuming a surface layer of pure Ag and the 2nd layer has a Ag % less than 75% to give a total average of 75 at% Ag for a AuAg particle with a 4 nm in diameter particle, the resulting compositions of the particles vs. the number of layers dealloyed is calculated and shown in Table 4.2.

Table 4.2. Theoretical calculation for the resulting composition with different depths of dealloying

# of surface laylers dealloyed	1	2	3	4
Au at% of dealloyed particles	37%	45%	60%	78%

The Ag loss for particles dealloyed at 0.1 V is less than the 1st layer dealloying, which may result from the chemical dissolution of the surface oxide of Ag. For the particles dealloyed at 0.3V, the final average Au% is ~37% which corresponds to 1st layer dealloying. This potential is about 120 mV lower than the open circuit potential of bulk Ag in deaerated 0.1M H_2SO_4. In Figure 4.17, it could be seen that as the voltage increases, more Ag is dissolved. However, even up to 1.4V, the Au composition is ~65%, which corresponds to 3~4 ML dealloying depth.

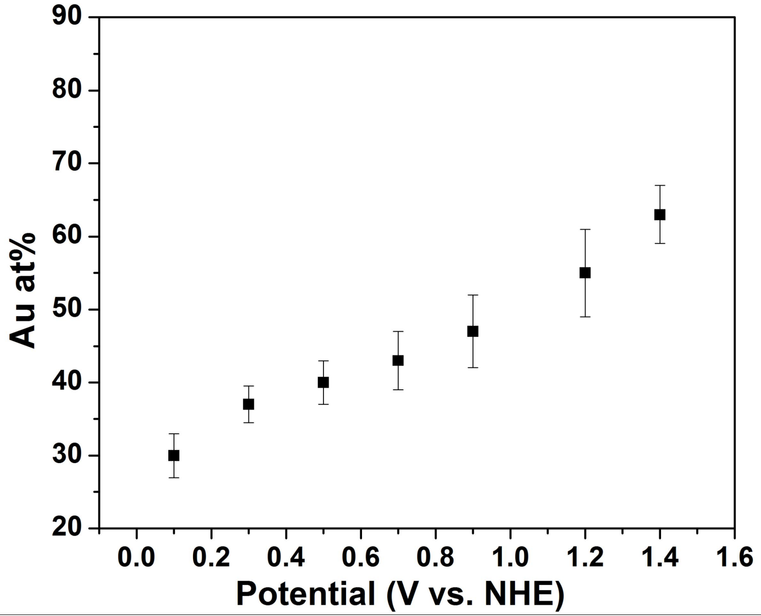

Figure 4.17. Composition of dealloyed $Au_{25}Ag_{75}$ particles vs. dealloying voltages. For each sample, ~100 spectra were taken and the standard deviations of the compositions were plotted as the error bars in the figure.

The atomic structure and composition of the particles dealloyed at 1.4V were examined in the aberration-corrected JEOL ARM200F STEM at 80 KV.

This low voltage could effectively reduce the beam damage on the particles [85]. No porous particles were observed for the dealloyed samples. The HAADF images of AuAg particles dealloyed at 1.4V are compared with the original AuAg particles shown in Figures 4.18 and 4.19, and it is observed that the dealloyed particles show a more open surface structure than the original particles. There are more single atoms around particles for the dealloyed sample compared with the original sample.

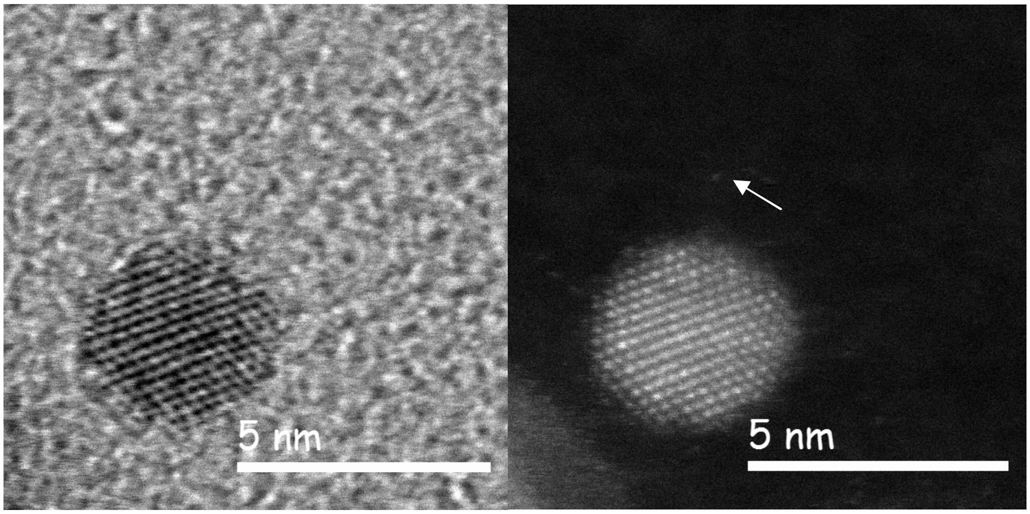

Figure 4.18. Aberration-corrected BF and HAADF images for original ATP coated AuAg particle.

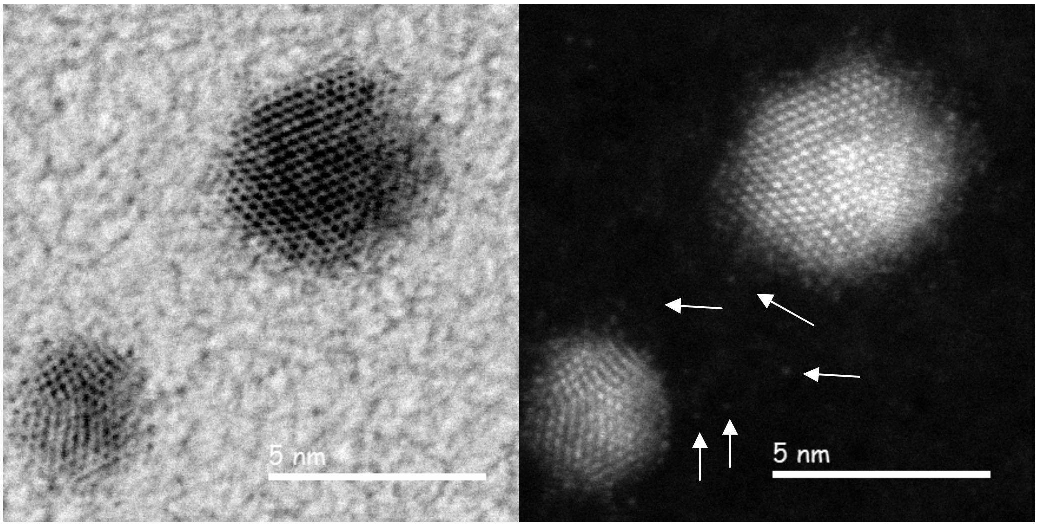

Figure 4.19. Aberration-corrected BF and HAADF images for ATP coated AuAg particles dealloyed at 1.4 V in 0.1 M H_2SO_4. Free atoms around the particles could be seen in HAADF image.

The composition distribution in individual AuAg particle dealloyed at 1.4 V was examined by a combination of HAADF image and Ag electron energy loss spectroscopy (EELS) mapping by aberration-corrected microscope, since EELS signal for Au is quite weak. Figure 4.20 is a dealloyed AuAg particle and the inset image is the overlying of Ag EELS map (red) and HAADF image (blue). The center pink area is where Ag EELS signal and HAADF image overlaps. EELS line scan on another dealloyed particle is shown in Figure 4.21, in which the green profile is the HAADF image intensity profile and the red curve is the Ag EELS line scan profile. The EELS results show that the dealloyed particles have a core-shell structure and almost no Ag is left in the outer shell.

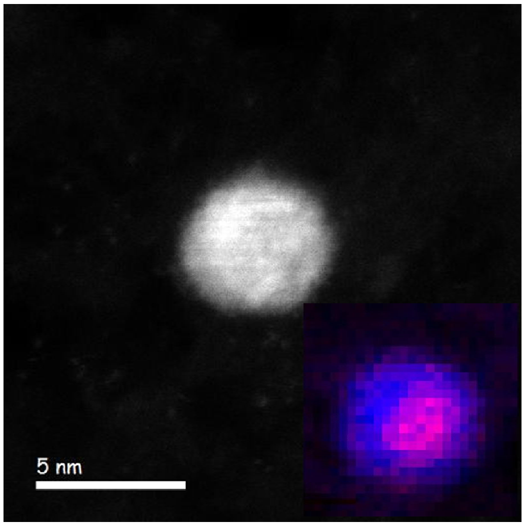

Figure 4.20. Aberration corrected HAADF image and corresponding EELS map of a AuAg nanoparticle dealloyed at 1.4 V. Blue: dark field image intensity; Red: Ag EELS intensity. It could be seen that this particle shows a core-shell structure and has almost no Ag in the shell.

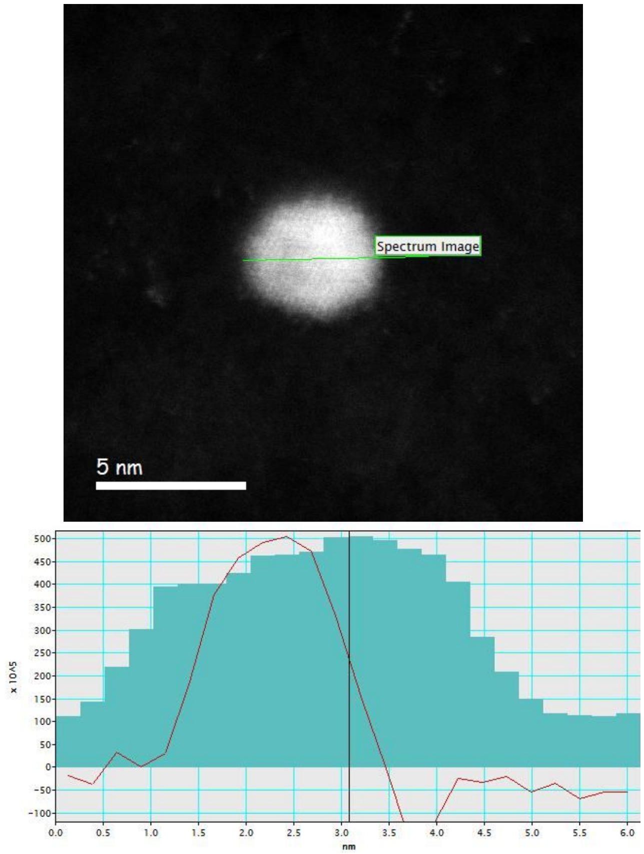

Figure 4.21. Aberration corrected HAADF image and corresponding EELS line scan of a AuAg nanoparticle dealloyed at 1.4 V. Green: intensity profile of the HAADF image; Red: EELS line profile of Ag.

4.3 Large AuAg particle dealloying

4.3.1 Particle synthesis and characterization

Citrate coated AuAg alloy nanoparticles were synthesized by a method reported by Link S et al. [92]. Briefly, $HAuCl_4$ (3.87×10^{-7} mol) and $AgNO_3$ (1.16×10^{-6} mol) were added to 100 mL nanopure water and the solution was stirred and boiled. Sodium citrate solution (1 mL, 1% by mass), as the capping and reducer, was added into the boiling solution and the solution was further boiled and stirred for 30 min. During stirring and boiling, the solution turned to a light yellow color. After the reaction, the solution was left to cool to room temperature. The flask used for synthesis should be quite clean, unless there would be precipitates formed on the wall and the yield would be quite low. Finally, the particle solution was concentrated from 100 mL to ~2 mL on a rotary evaporator. Over concentrating the solution would cause the precipitation of particles, since citrate is a capping materials working as electrostatic stabilizer which is quite weak.

As prepared particles were loaded on a carbon coated Au grid (Ted pella Inc.) and dealloyed by holding the potential at 1.2 V vs. NHE or cyclic voltammetry between 0.6 V to 1.2 V for 50 cycles with a scan rate of 50 mV/s. No obvious feature was observed for the dealloyed particles. It was speculated that the composition in individual particle might not be quite uniform. To get more homogeneous composition distribution, the particles were annealed in 400°C in forming gas (5%H_2/N_2) for an hour. The size distribution and composition of the annealed particles were characterized by STEM-EDX using JEOL-2010F at 200KV. The composition of individual particles was determined from the Au and Ag signals collected by scanning the beam in an area only containing the particle examined. The EDX spectra from about 100 particles were collected and the average composition of the AuAg particles was 22% Au ± 3%, and the dispersion resulting from counting error for each spectrum was with ± 1.5%. The HAADF STEM image showed that the z-contrast in an individual particle was quite uniform. EDX line scan across one particle was collected and the composition variation was within ± 5%.

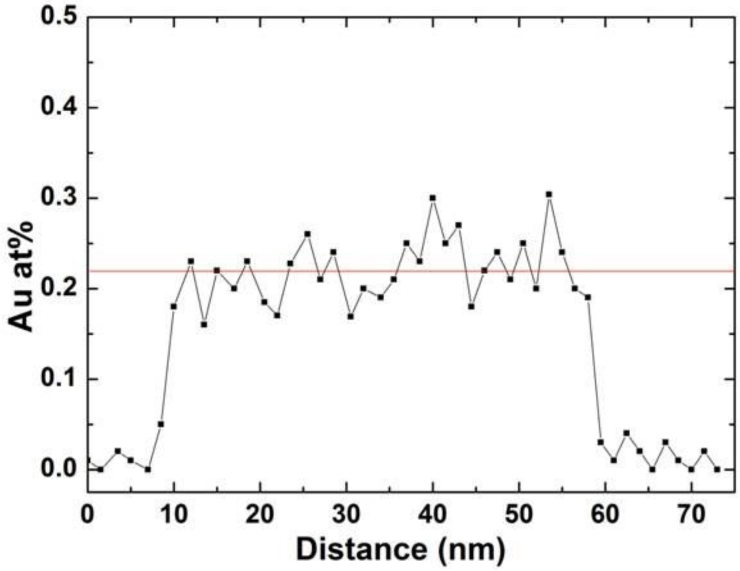

Figure 4.22. EDX line scan across a citrate AuAg particle. The average composition of this particle is 22% Au.

4.3.2 Dealloying experiment of large AuAg particles

The dealloying experiment was carried out in air at room temperature in 1 M $HClO_4$ (GFS Chemicals, VERITAS® DOUBLE DISTILLED). MSE was used as reference electrode. All potentials quoted are with respect to the NHE. The counter electrode was a PtIr wire. The C coated Au TEM grid with particles was held on a piece of Au film by Au wires and dipped in the electrolyte. The particles were dealloyed by chronoamperometry with different potentials ranging from 0.54 V to 1.3 V. The dealloying time listed in Table 4.3 was decided by aiming to get a 25 nm dealloying depth based on the charge integration from Corcoran's current decay curve [61] as shown in Figure 4.23.

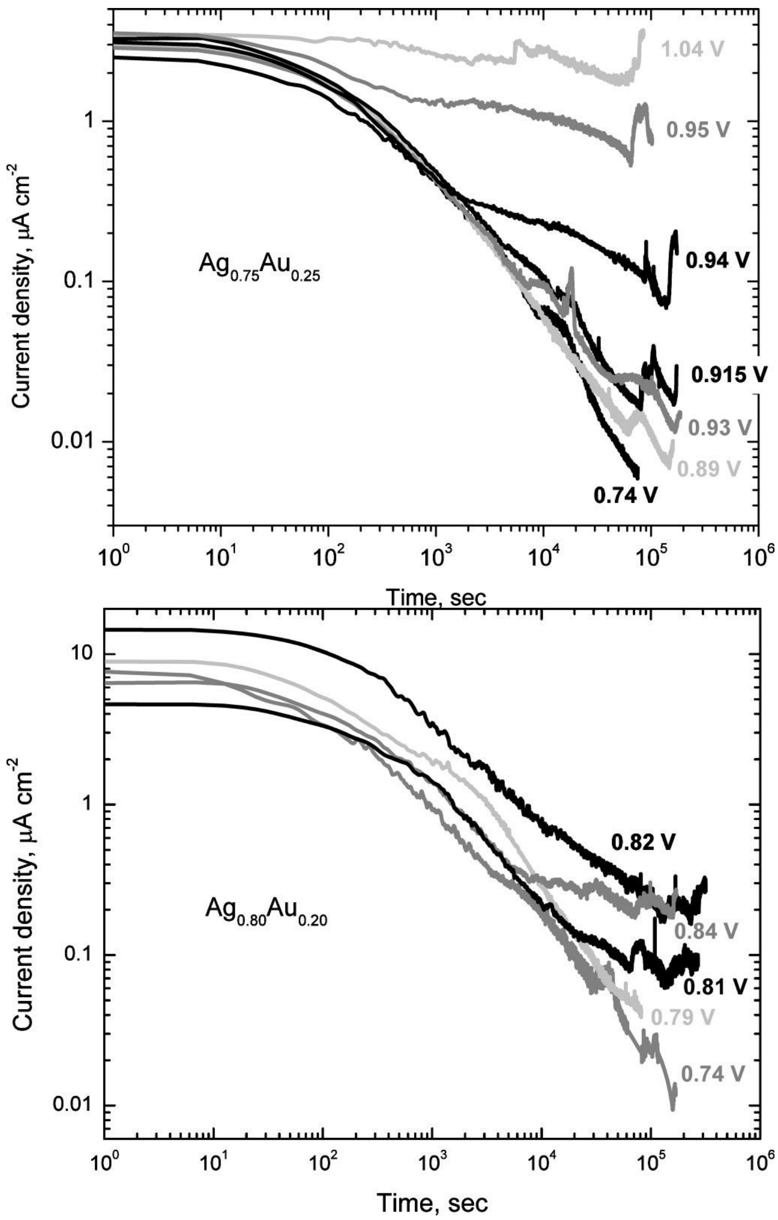

Figure 4.23. Current response of $Ag_{0.75}Au_{0.25}$ and $Ag_{0.8}Au_{0.2}$ bulk samples in 0.1 M $HClO_4$ held at the indicated potentials. All potentials are referenced to NHE [61].

Table 4.3. Dealloying time at each potential

Dealloying potential (V vs. NHE)	Dealloying time
0.54	6 hrs
0.64	6 hrs
0.74	5 hrs
0.84	30 mins
0.9	2 mins
0.9	30 mins
0.9	5 hrs
1.1	30 mins
1.3	30 mins

For samples dealloyed at potentials above 0.9 V, all the particles showed a porous structure. For sample dealloyed at 0.74 V, 35% of ~200 examined particles were porous and some particles showed some degree of surface roughing as seen in Figure 4.27. For sample dealloyed at 0.64 V, only 2~3% of ~ 200 particles were porous. There was no porous particle observed for the sample dealloyed at 0.54 V.

Comparing the samples dealloyed at 0.9 V for different times, it was found that the longer the dealloying time, the larger the ligaments size. This phenomenon could be well shown in KMC simulation for dealloying with different length of time. Figure 4.30 includes the morphologies for a $Au_{20}Ag_{80}$ particle with a radius of 45 atoms (9.6 nm) dealloyed at 1.05 eV for different length of time by KMC simulation. It can be seen that at the early stage, the surface roughing wave length is small and the particle is only partially dealloyed. As the time evolves, ligaments become larger and continuous because of Ag dissolution and Au ligament coarsening. Most particles dealloyed at 0.54 V look similar to the original particles. Compared with the sample dealloyed at 0.9 V for 5 hrs and above 0.9 V, the porous structure of the samples dealloyed at 0.64 V and 0.74 V was not as “deep” and coarsened up. One possible reason may be that the surface diffusivity of Au at lower potential is lower than that at higher potentials (i.e., potential dependent surface diffusion) so the buried Ag atoms couldn’t easily be exposed. As shown in Figure 4.32, the diffusivity at 0.84 V in 1 M $HClO_4$ could be 4~5 times of the value at 0.74 V [93]. Further experiments are needed to check the dealloying behavior and resulting morphology variation by only tuning the surface diffusivity while keeping the dissolution rate constant. An interesting phenomenon is that either the porous structure or surface roughing of order 2~3 nm was quite stable even after several days.

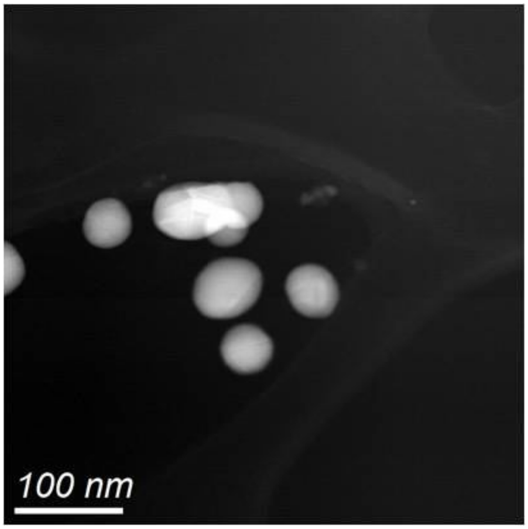

Figure 4.24. HAADF image of citrate-AuAg particles after annealing in forming gas (N_2/ 5%H_2) at 400°C for 1hr. The average size is 45 nm in diameter and average composition is 21± 3 at% Au. The contrast in individual particles is quite uniform.

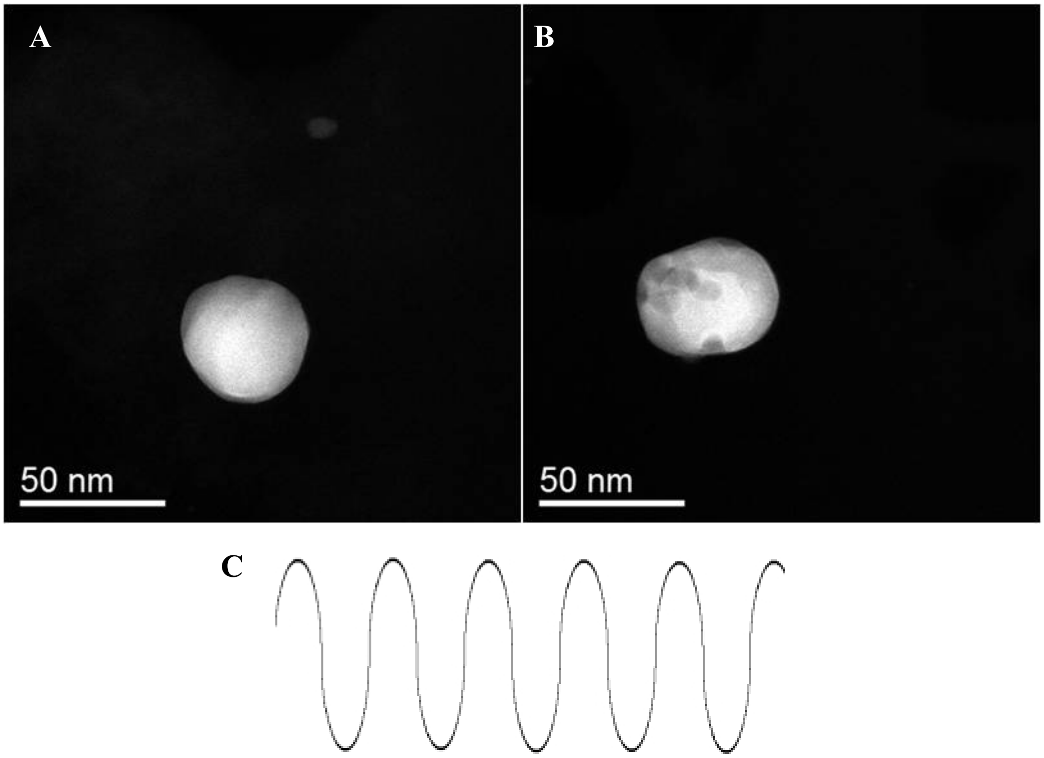

Figure 4.25. HAADF images of citrate-AuAg particles dealloyed at 0.54 V for 6 hrs in 1 M $HClO_4$ in air. (A) Most particles still looked like original particles. (B) Very few particles showed some surface roughing which is quite similar to the sine wave appeared at the initial stage of dealloying schematically described in (C).

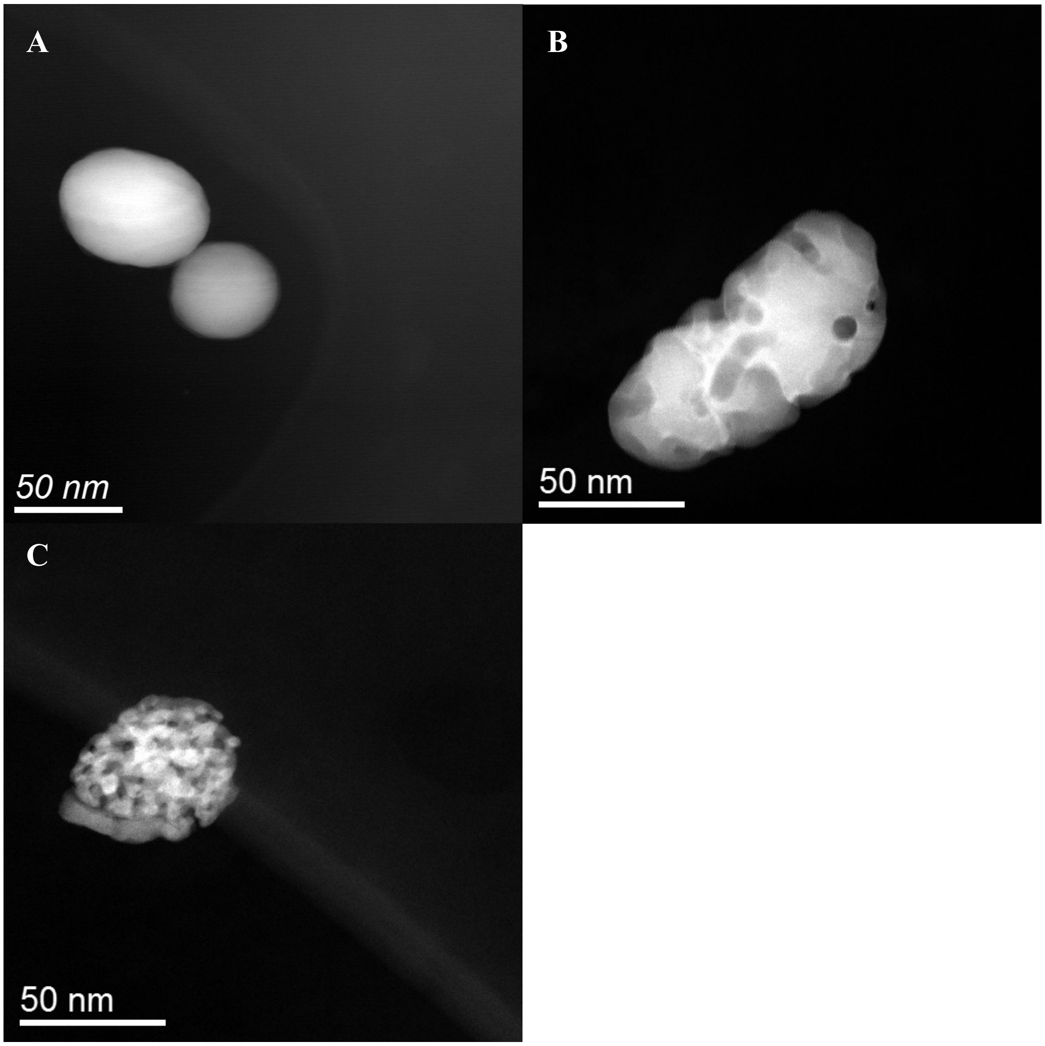

Figure 4.26. HAADF images of citrate-AuAg particles dealloyed at 0.64 V for 6 hrs in 1 M $HClO_4$ in air. (A) Most particles looked like original particles. (B) Some particles showed some surface roughing. (C) Less than 5% particles showed some porous feature based on the examination of 200 particles.

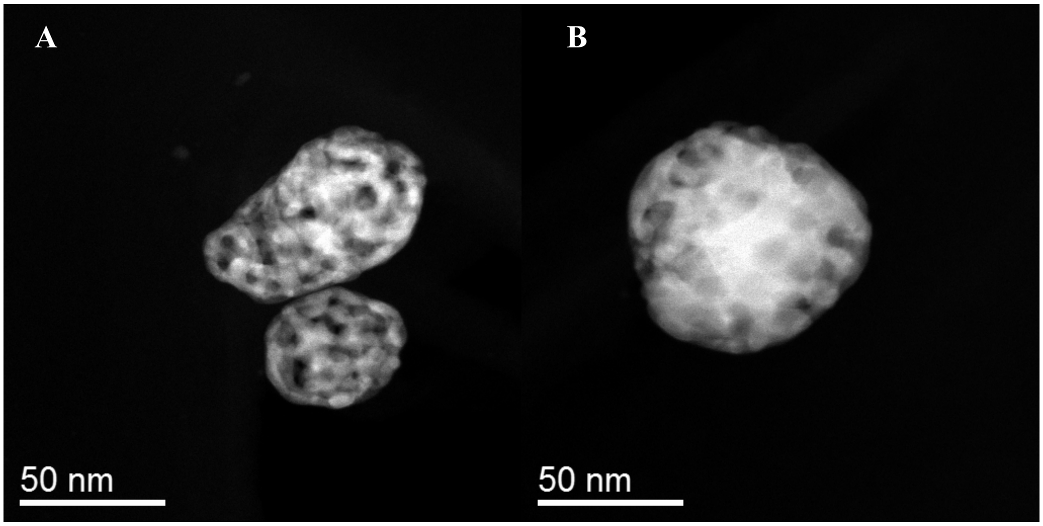

Figure 4.27. HAADF images of porous structure of citrate-AuAg particles dealloyed at 0.74 V for 6 hrs in 1 M $HClO_4$ in air. Only ~35% particles show porous structure based on the examination of 200 particles as shown in (A), and the pore size looks smaller (3~5 nm) compared with those dealloyed at higher voltage. (B) Some particles only show roughing to a certain depth. The porous structure and surface roughing are quite stable even after several days.

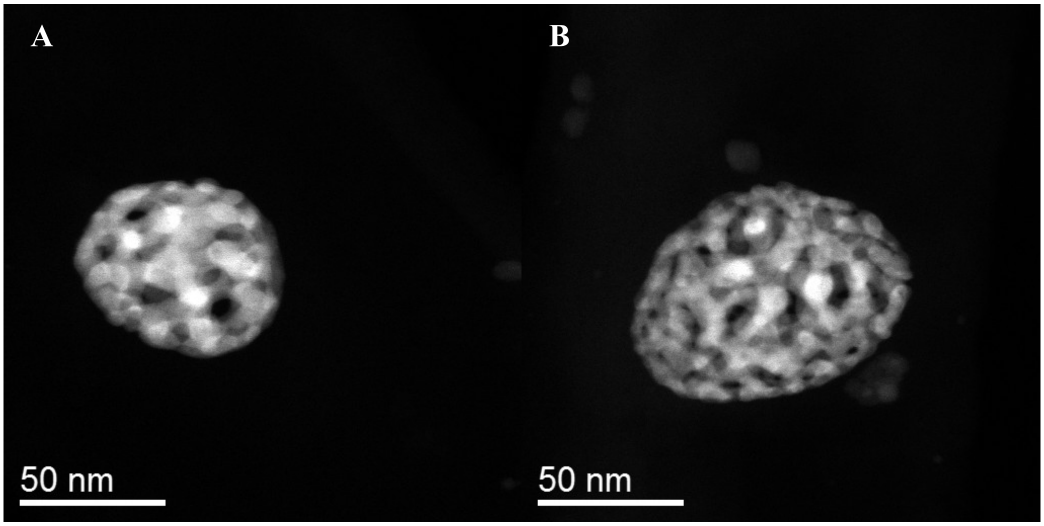

Figure 4.28. HAADF images of porous structure of citrate-AuAg particles dealloyed at 0.84 V for 30 mins in 1 M $HClO_4$ in air.

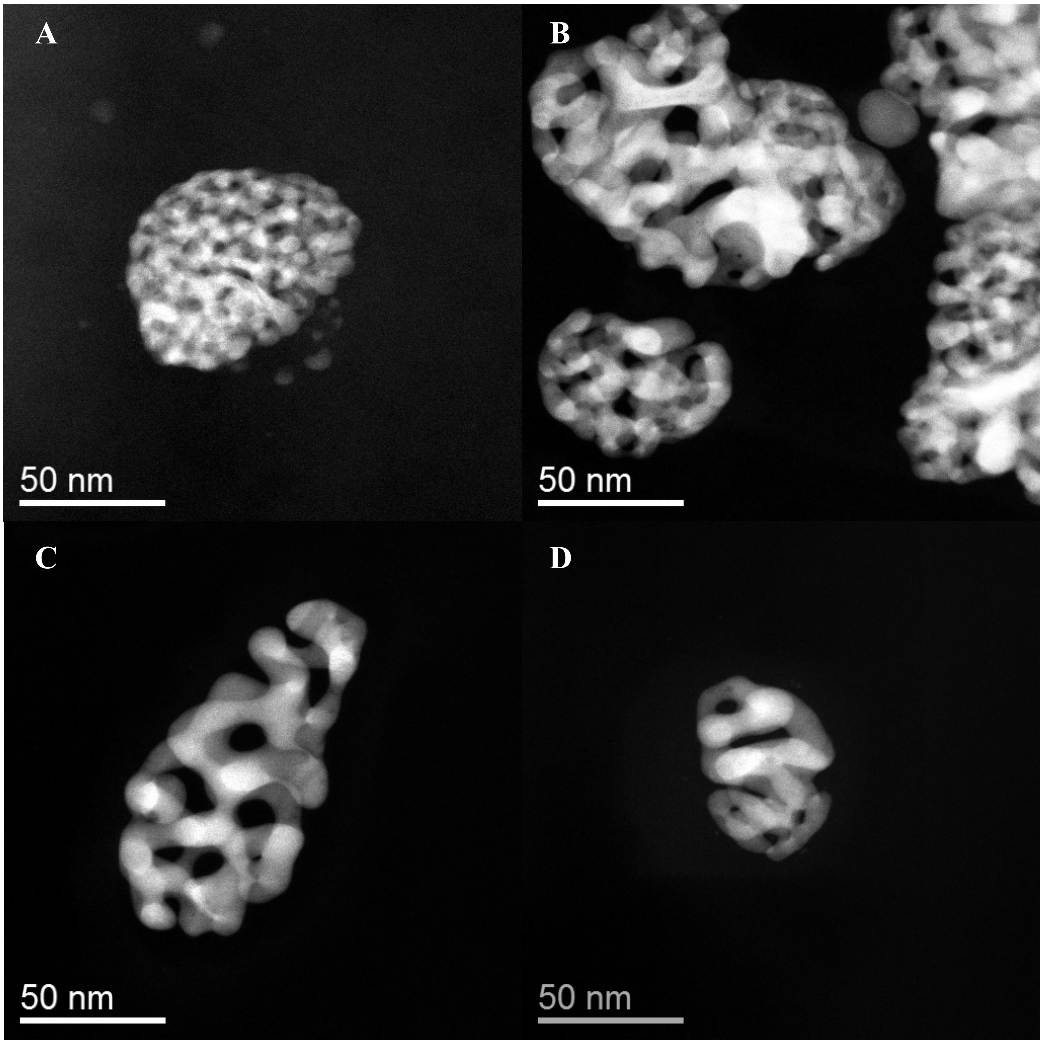

Figure 4.29. HAADF images for porous structure of citrate-AuAg particles dealloyed at (A) 0.9 V vs. NHE for 2 mins. (B) 0.9 V vs. NHE for 30 mins. (C) 0.9 V vs. NHE for 6 hrs and the ligament size is 7~8 nm. (D) 1.1V vs. NHE for 30min, the ligament size is similar to that in (C). All were dealloyed in 1 M $HClO_4$ in air. All the particles showed a porous structure.

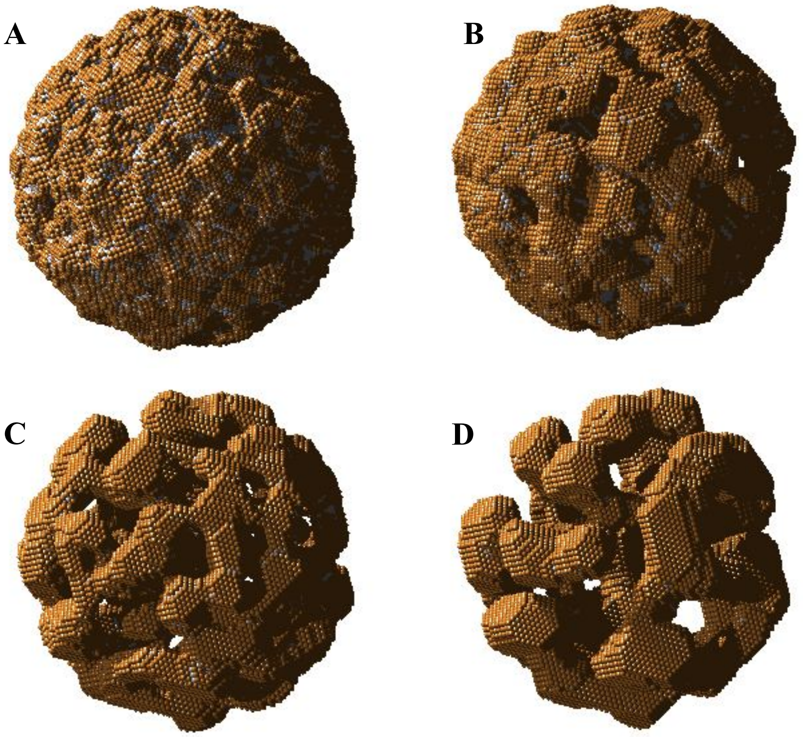

Figure 4.30. KMC simulation of $Au_{20}Ag_{80}$ particle (r=45, which is 9.6 nm) dealloying at 1.05eV for: (A) 6 s; (B) 50 s; (C) 400 s; (D) 1757 s.

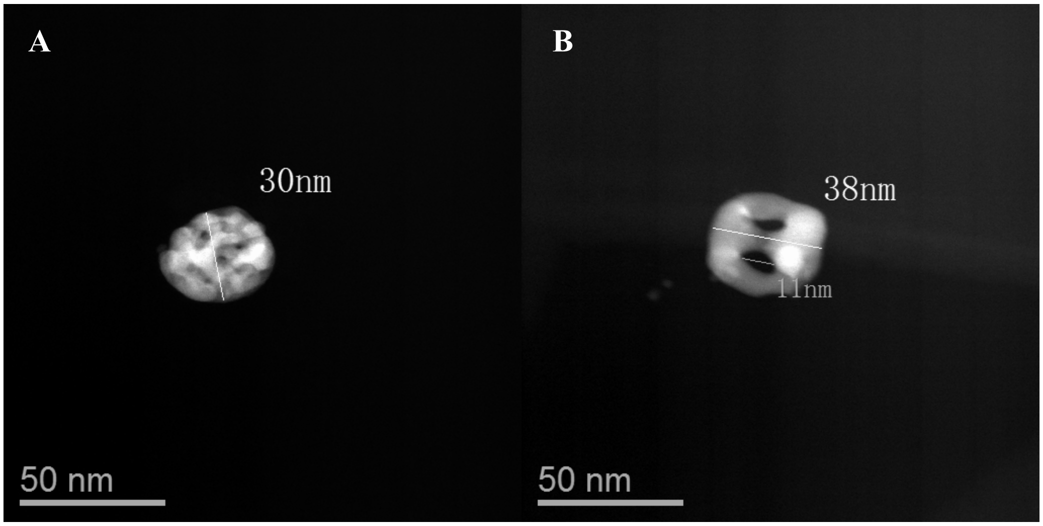

Figure 4.31. HAADF images of porous structure of citrate-AuAg particles dealloyed at 1.3 V vs. NHE for 15min in 1 M $HClO_4$ in air. (A) Most particles show a smaller pore size than particles dealloyed at lower potentials. The pore size is less than 2 nm and the ligament size is 3-4 nm. (B) Very few particles look similar to the particles dealloyed at lower potentials.

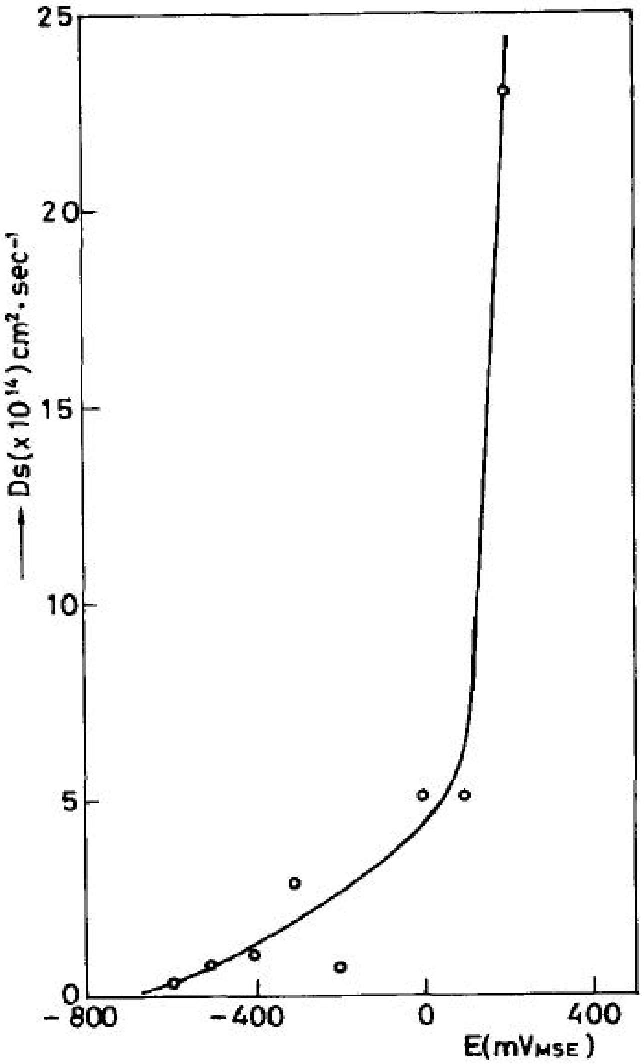

Figure 4.32. Variation of surface diffusion coefficients at different potentials for Au in 1 M $HClO_4$ at room temperature [93].

The size distribution and percent of porous particles for samples dealloyed at different potentials are shown in Figure 4.33. There is almost no size change for particles dealloyed at 0.54 V. As the dealloying voltage increases, the average size becomes smaller. For the sample dealloyed at 1.3 V, the morphology of most particles as shown in Figure 4.31(A) show a smaller pore and ligament size than the particles dealloyed at lower potentials. There are two possibilities that this structure forms. The first one is that since the dealloying rate is too high, the as formed porous structure collapses. In that case, the average size of the dealloyed particles should be much smaller than that dealloyed at 1.1 V. The second possibility is that the voltage reaches the Au oxidation region, so the surface diffusivity of Au is much slower which makes the final pore size smaller than that for the lower voltage. Based on the size distribution analysis as shown in Figure 4.33, the second explanation seems more reasonable.

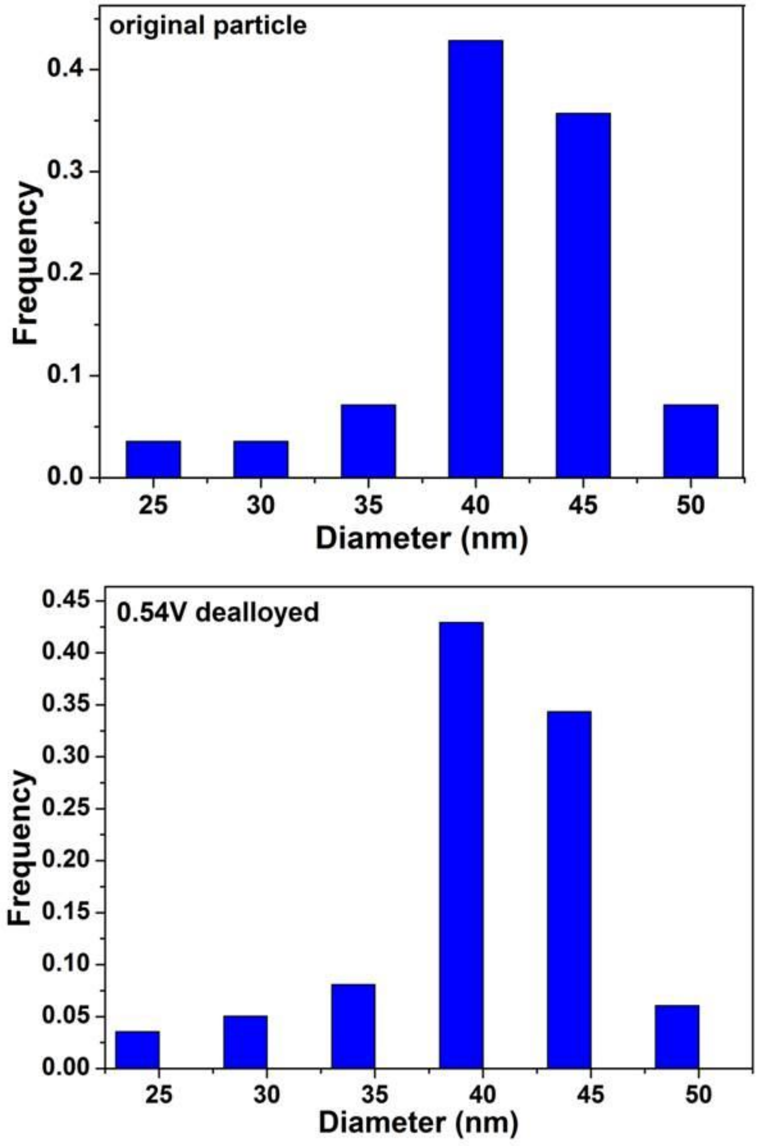

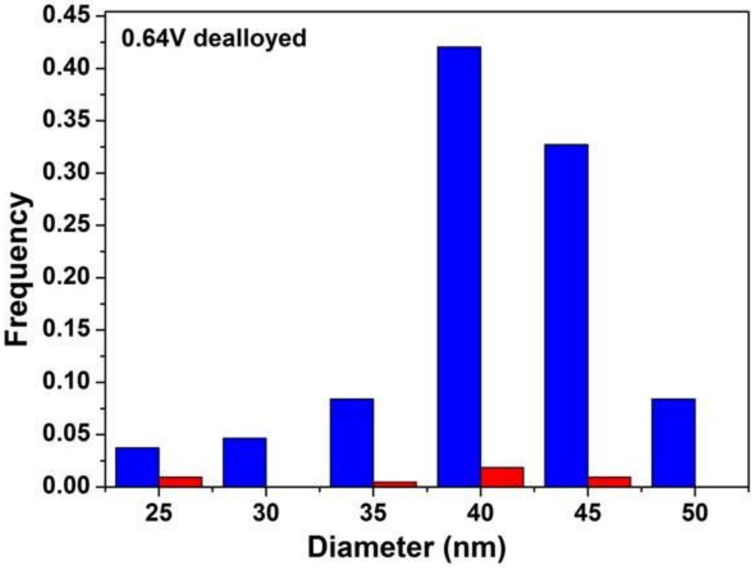
0.64V dealloyed
Frequency
0.00
0.05
0.10
0.15
0.20
0.25
0.30
0.35
0.40
0.45
Diameter (nm)
25
30
35
40
45
50

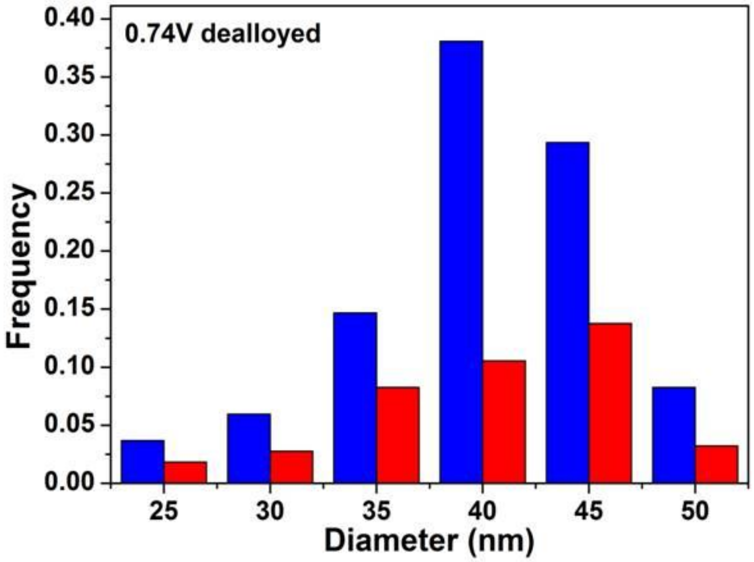
0.74V dealloyed
Frequency
0.00
0.05
0.10
0.15
0.20
0.25
0.30
0.35
0.40
Diameter (nm)
25
30
35
40
45
50

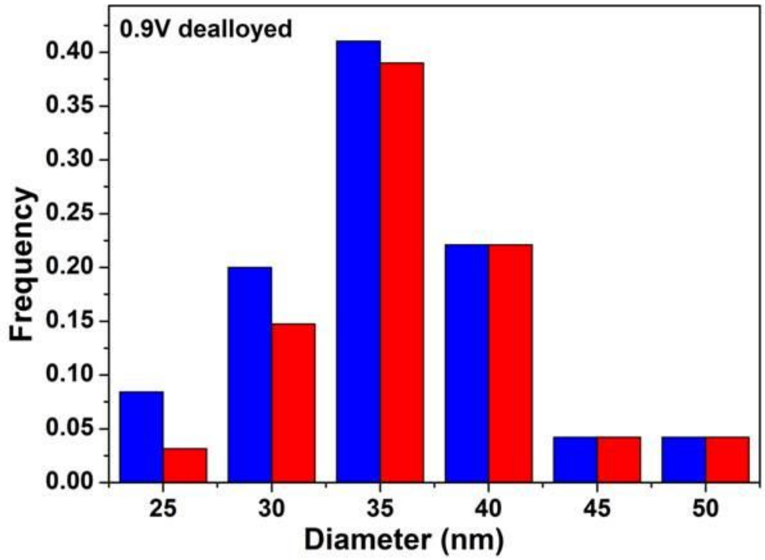
0.9V dealloyed
Frequency
0.00
0.05
0.10
0.15
0.20
0.25
0.30
0.35
0.40
25
30
35
40
45
50
Diameter (nm)

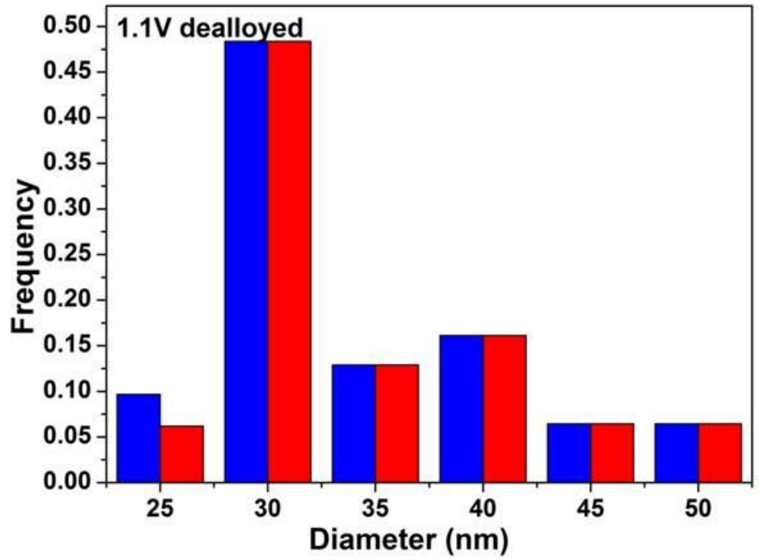
1.1V dealloyed
Frequency
0.00
0.05
0.10
0.15
0.20
0.25
0.30
0.35
0.40
0.45
0.50
25
30
35
40
45
50
Diameter (nm)

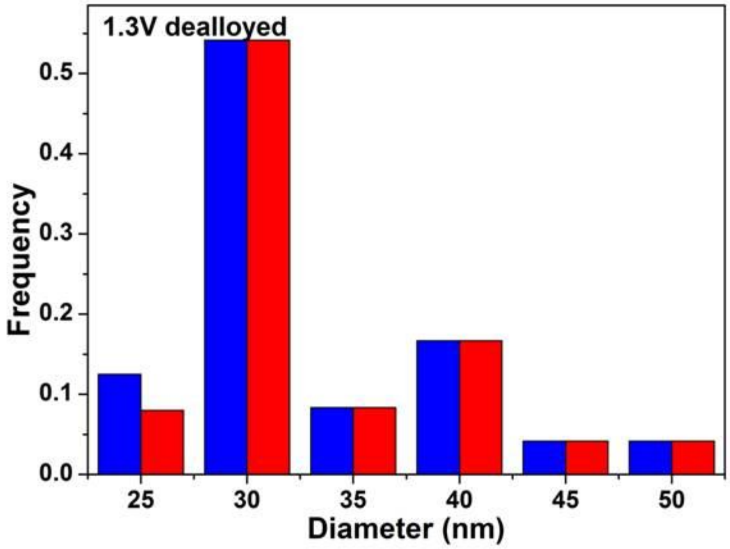

Figure 4.33. Size distribution and percent of porous particles for the original citrate-AuAg particles and the particles dealloyed at different potentials. Blue: # of particles at each size normalized by the total # of particles examined. Red: # of porous particles at each size normalized by the total # of particles examined. For particles with diameter a nm, it includes all the particles with diameter in the range between (a-2.5) nm and (a+2.5) nm. Frequency is calculated by dividing the number of particle at each diameter by the total number of particle. For each sample, 100~200 particles were examined.

Considering that the particle size is above 20 nm in diameter, no Gibbs-Thomson size effect on dealloying would be expected. If we define the critical potential as the potential at which the possibility of forming porous structure is 50%, the critical potential for AuAg particle with 79% Ag is ~0.74V, which is ~50 mV lower than the critical potential determined by current decay method for the bulk $Au_{20}Ag_{80}$ alloy [61]. Thermodynamically, if assuming $[Ag^+]$ is 10^{-6} M, the lower limit of critical potential for $Au_{20}Ag_{80}$ bulk alloy is 0.64 V according to Figure 4.5. The result from KMC simulation for $Au_{20}Ag_{80}$ bulk alloy is ~ 0.9 V [63], which is also ~ 200 mV higher than the OCP of Ag/Ag^+ 0.7 V.

To make a comparison between this particle dealloying and the bulk sample dealloying, $Au_{20}Ag_{80}$ foil (1 mm thick) was polished with sand paper

(2400 grit) and dealloyed at 0.74 V with the same procedure as the particle dealloying experiment. The dealloyed surface was checked by SEM and no obvious porous feature was observed. One possibility is that the surface is too rough and the dealloyed features are masked by surface amplitude fluctuations.

4.4 coating effect

The effect of the ATP and citrate coating on the dealloying behavior was checked on a bulk AuAg alloy. Three pieces of $Au_{28}Ag_{72}$ alloys with the same surface areas were immersed overnight in ATP solution in water (0.01 M, which is a much higher concentration than that used in particles synthesis), and citrate solution in water (1%, same concentration as that in particles synthesis). Dealloying was carried out in 0.1 M H_2SO_4 by linear sweep up to 1.5 V vs. NHE. MSE was used as reference electrode and PtIr wire was used as counter electrode. The polarization curves of the two samples were compared with a bare $Au_{28}Ag_{72}$ sample. All three samples showed similar polarization curves.

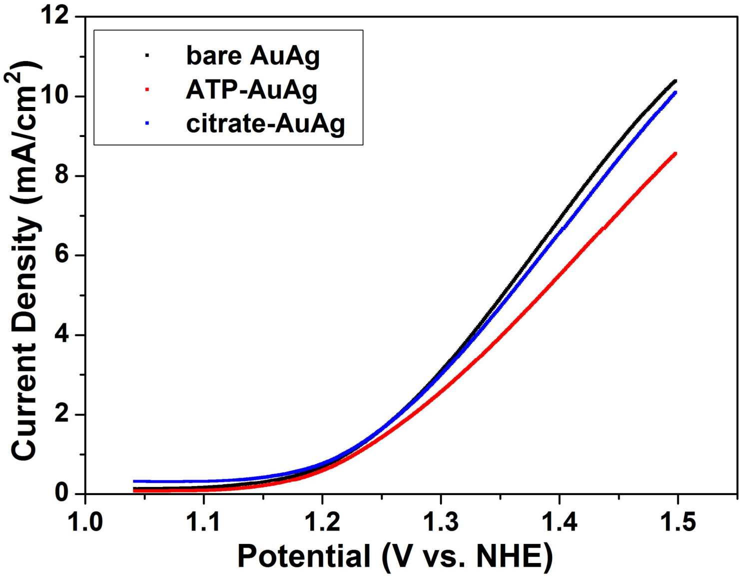

Figure 4.34. Anodic polarization curves for $Au_{28}Ag_{72}$ samples with difference coatings in 0.1 M H_2SO_4. Scan rate = 5 mV/s.

To further confirm whether the sample has been dealloyed uniformly, those three dealloyed samples were annealed in air at 250°C for 10 min (to make porosity evolution more evident) and the surfaces were checked in SEM on Nova 200 Nanolab. The citrate and ATP coated samples showed uniform porous structure similar to the bare sample as shown in Figure 4.35.

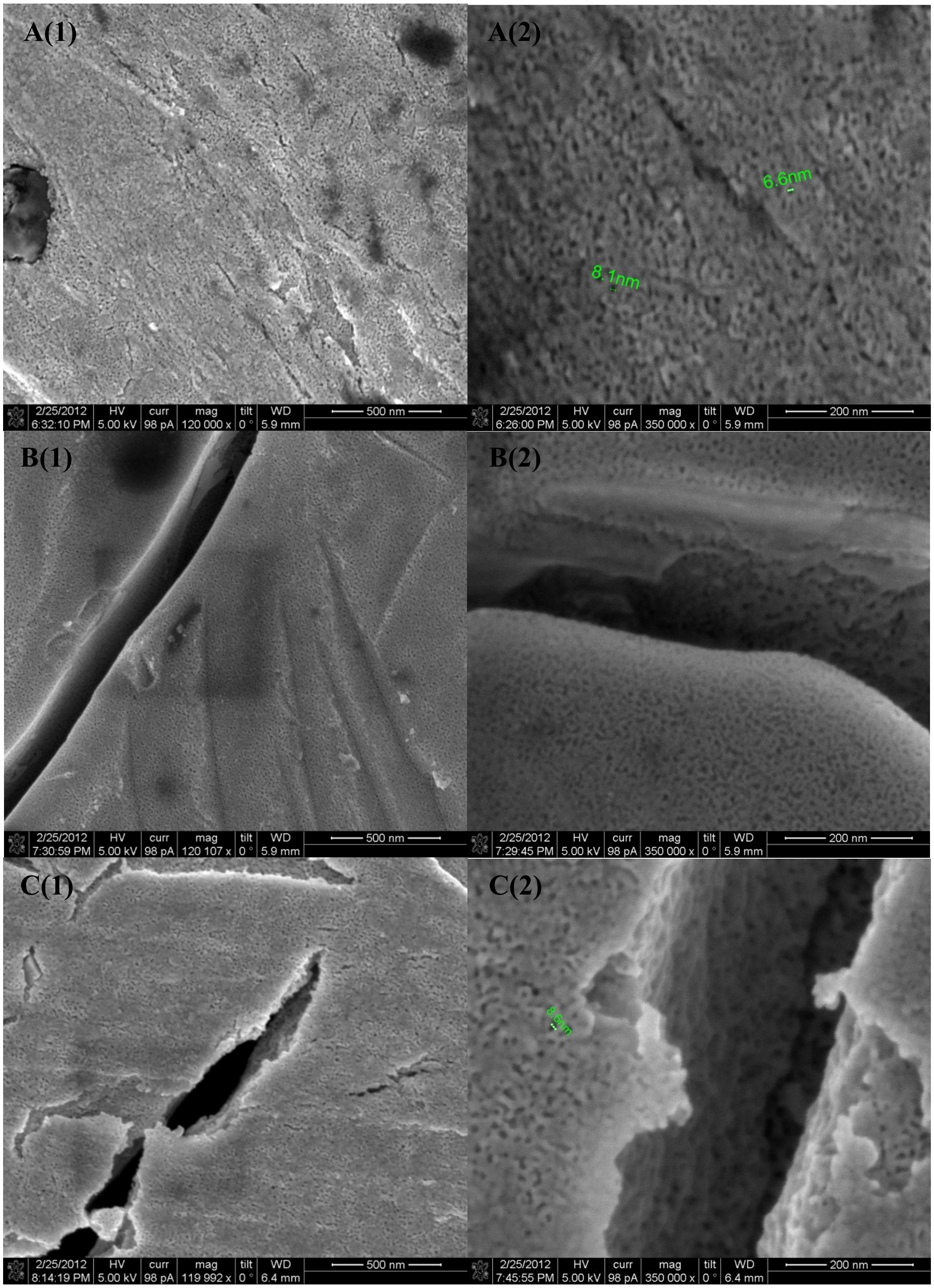

Figure 4.35. SEM images of $Au_{28}Ag_{72}$ samples with difference coatings dealloyed by linear voltage sweep up to 1.5V vs. NHE in 0.1M H_2SO_4. (A) Bare sample: (1) 120KX; (2) 350KX. (B) ATP coated sample: (1) 120KX; (2) 350KX. (C) Citrate coated sample: (1) 120KX; (2) 350KX. Since the samples were dealloyed up to 1.5V vs. NHE, Au should have been oxidized, so the pore size is quite small.

4.5 Summary

Dealloying of nanoparticles has become an important topic in various applications. The background of bulk alloy dealloying behavior and some recent work about alloy nanoparticle dealloying was introduced and summarized in this chapter. Experimentally, dealloying behavior of different size range AuAg particles were studied. The surface dealloying potential of small particles with 4 nm in diameter showed a depression resulting from a Gibbs Thomson effect and no bulk dealloying was observed for this set of small particles. Large particles ~ 45 nm in diameter dealloyed and formed porous structures at a potential quite close to the thermodynamic limit for bulk dealloying.

Small ATP coated AuAg particles ~4 nm in diameter were synthesized by chemical reduction and characterized by TEM and STEM-EDX. The size and composition distributions were quite narrow. In the in-situ ECSTM experiment, ATP coated $Au_{40}Ag_{60}$ particles was ligand exchanged by DDT into organic phase and the particles were dispersed on a Au thin film. Dealloying behavior of the particles in 0.1 M H_2SO_4 was studied by in-situ ECSTM from 0.2 V to 0.9 V vs. NHE. The dealloying behavior of ATP coated $Au_{25}Ag_{75}$ particles was studied ex-situ by STEM and EDX in 0.1 M H_2SO_4 in the potential range from 0.1 V to 1.4 V vs. NHE. The morphological and compositional analysis showed that surface dealloying started from 0.3 V, which is ~ 120 mV lower than the open circuit potential of Ag/Ag^+. This value was consistent with the themodynamic calculation based on Gibbs Thomson equation. Even up to 1.4 V, there were only less than 3~4 layers on the surface dealloyed and core-shell structure was formed for the particles in this size range which were consistant with the KMC simulation result. The high resolution HAADF image by aberration corrected STEM showed a more open surface structure for some dealloyed particles compared with original particles.

Large citrate coated $Au_{20}Ag_{80}$ particles ~45 nm in diameter were synthesized by co-reduction of Au and Ag salts in aqueous phase. The as synthesized particles were annealed in forming gas at 400°C for 1 hr to get a more homogenous composition distribution. The size and composition of annealed particles were characterized in STEM and EDX. Dealloying behavior of this particles in 1 M $HClO_4$ was studied ex-situ by STEM. The particles were dealloyed at a series of potentials from 0.54 V to 1.3 V vs. NHE. The lowest potential that porous structure could be observed was 0.64 V which is close to the thermodynamic limit for bulk dealloying at this composition. About 50% particles formed porous structure after dealloying for the sample dealloyed at 0.74 V and all particle formed porous structures for sample dealloyed above 0.9 V. The average ligament size was 7~8 nm for the particles dealloyed between 0.9 V and 1.1 V.

REFERENCES

[1] G. Tammann, “Die chemischen und galvanischen eigenschaften von mischkristallen und ihre atomverteilung,” *Z. anorg. u. allg. Chem.*, vol. 107, no. 7, 1919.

[2] K. Sieradzki, “Curvature effects in alloy dissolution,” *Journal of The Electrochemical Society*, vol. 140, no. 10, p. 2868, 1993.

[3] I. C. Oppenheim, D. J. Trevor, C. E. Chidsey, P. L. Trevor, and K. Sieradzki, “In situ scanning tunneling microscopy of corrosion of silver-gold alloys,” *Science (New York, N.Y.)*, vol. 254, no. 5032, pp. 687–9, Nov. 1991.

[4] H. Pickering, “Characteristic features of alloy polarization curves,” *Corrosion Science*, vol. 23, no. 10, p. 1107, 1983.

[5] J. Erlebacher, M. J. Aziz, A. Karma, N. Dimitrov, and K. Sieradzki, “Evolution of nanoporosity in dealloying,” *Nature*, vol. 410, no. 6827, pp. 450–3, Mar. 2001.

[6] K. Sieradzki, N. Dimitrov, D. Movrin, C. McCall, N. Vasiljevic, and J. Erlebacher, “The dealloying critical potential,” *Journal of The Electrochemical Society*, vol. 149, no. 8, p. B370, 2002.

[7] A. Dursun, D. V. Pugh, and S. G. Corcoran, “Dealloying of Ag-Au alloys in halide-containing electrolytes,” *Journal of The Electrochemical Society*, vol. 150, no. 7, p. B355, 2003.

[8] D. V. Pugh, A. Dursun, and S. G. Corcoran, “Electrochemical and morphological characterization of Pt–Cu dealloying,” *Journal of The Electrochemical Society*, vol. 152, no. 11, p. B455, 2005.

[9] J. Rugolo, J. Erlebacher, and K. Sieradzki, “Length scales in alloy dissolution and measurement of absolute interfacial free energy,” *Nature materials*, vol. 5, no. 12, pp. 946–9, Dec. 2006.

[10] H.-J. Jin and J. Weissmüller, “A material with electrically tunable strength and flow stress,” *Science (New York, N.Y.)*, vol. 332, no. 6034, pp. 1179–82, Jun. 2011.

[11] A. Wittstock, J. Biener, and M. Bäumer, “Nanoporous gold: A new material for catalytic and sensor applications,” *Physical chemistry chemical physics : PCCP*, vol. 12, no. 40, pp. 12919–30, Oct. 2010.

[12] J. Biener, A. Wittstock, L. a Zepeda-Ruiz, M. M. Biener, V. Zielasek, D. Kramer, R. N. Viswanath, J. Weissmüller, M. Bäumer, and a V. Hamza, "Surface-chemistry-driven actuation in nanoporous gold," *Nature materials*, vol. 8, no. 1, pp. 47–51, Jan. 2009.

[13] Z. Peng, S. a Freunberger, Y. Chen, and P. G. Bruce, "A reversible and higher-rate Li-O_2 battery," *Science (New York, N.Y.)*, vol. 337, p. 563, Jul. 2012.

[14] N. Dimitrov, J. a. Mann, M. Vukmirovic, and K. Sieradzki, "Dealloying of Al_2CuMg in alkaline media," *Journal of The Electrochemical Society*, vol. 147, no. 9, p. 3283, 2000.

[15] N. RC and M. A, "An AC ipedance study of the dealloying of Fe-Ni alloys, and its relevance to chloride SCC of stainless steels," *Corrosion Science*, vol. 28, no. 12, pp. 1183–1187, 1988.

[16] M. Shao, K. Shoemaker, A. Peles, K. Kaneko, and L. Protsailo, "Pt monolayer on porous Pd-Cu alloys as oxygen reduction electrocatalysts.," *Journal of the American Chemical Society*, vol. 132, no. 27, pp. 9253–5, Jul. 2010.

[17] S. Chen, W. Sheng, N. Yabuuchi, P. J. Ferreira, L. F. Allard, and Y. Shao-Horn, "Origin of oxygen reduction reaction activity on 'Pt_3Co' nanoparticles: Atomically resolved chemical compositions and structures," *The Journal of Physical Chemistry C*, vol. 113, no. 3, pp. 1109–1125, Jan. 2009.

[18] P. Strasser, "Dealloyed core-shell fuel cell electrocatalysts," *Reviews in chemical engineering*, vol. 25, no. 4, p. 255, 2009.

[19] V. R. Stamenkovic, B. Fowler, B. S. Mun, G. Wang, P. N. Ross, C. a Lucas, and N. M. Marković, "Improved oxygen reduction activity on $Pt_3Ni(111)$ via increased surface site availability.," *Science (New York, N.Y.)*, vol. 315, no. 5811, pp. 493–7, Jan. 2007.

[20] W. Cahn, "Surface stress and the chemical equilibrium of small crystals-I. The case of the isotropic surface," *Acta Metall.*, vol. 28, p. 1333, 1980.

[21] B. J.-P. Buffat Ph., "Size effect on the melting temperature of gold particles," *Phys. Rev. A.,*, vol. 13, p. 2287, 1976.

[22] A. J. Bard and L. R. Faulkner, *Electrochemical methods: fundamentals and applications*. New York: John Wiley & Sons, 2000.

[23] L. Meites, *Handbook of analytical chemistry*. New York: McGraw Hill, 1963, p. Sect 5.

[24] "Koslow reference electrode," 2012. [Online]. Available: http://koslow.com/reference_electrodes/5088/mercury_oxide_reference_electrode_5088?cPath=62.

[25] "Pd-H reference electrode," 2011. [Online]. Available: http://en.wikipedia.org/wiki/Palladium-hydrogen_electrode.

[26] "Electron-sample interactions," 2012. [Online]. Available: http://serc.carleton.edu/research_education/geochemsheets/electroninteractions.html.

[27] "LE-CSSS: Nova." [Online]. Available: http://le-csss.asu.edu/nova.

[28] D. B. Williams and C. B. Carter, *Transmission electron microscopy: A textbook for materials science*. Springer, 2004.

[29] "TEM and STEM optical paths." [Online]. Available: http://www.ceos-gmbh.de/FAQ/types.html.

[30] "LE-CSSS: 2010F." [Online]. Available: http://le-csss.asu.edu/2010.

[31] "LE-CSSS: ARM200F." [Online]. Available: http://le-csss.asu.edu/ARM200F.

[32] "Wikipedia: Scanning tunneling microscope," 2012. [Online]. Available: http://en.wikipedia.org/wiki/Scanning_tunneling_microscope.

[33] R. Neihof, "Simple non-gassing electrodes for use in electrophoresis," *Nature*, vol. 185, p. 526, 1960.

[34] R. Neihof, "Microelectrophoresis apparatus employing palladium electrodes," *Journal of colloid and interface science*, vol. 30, no. 1, pp. 128–33, May 1969.

[35] M. Fleischmann and J. N. Hiddleston, "A palladium-hydrogen probe electrode for use as a microreference electrode," *J. Phys. E*, vol. 1, p. 667, 1968.

[36] L. Tang, B. Han, K. Persson, C. Friesen, T. He, K. Sieradzki, and G. Ceder, "Electrochemical stability of nanometer-scale Pt particles in acid environments," *J. Am. Chem. Soc.*, vol. 132, no. 14, pp. 596–600, 2010.

[37] J. Lindahl, T. Takanen, and L. Montelius, “Easy and reproducible method for making sharp tips of Pt/Ir,” *J. Vac. Sci. Technol. B*, vol. 16, no. 6, pp. 3077–3081, 1998.

[38] L. Libioulle, Y. Houbion, and J.-M. Gilles, “Very sharp platinum tips for scanning tunneling microscopy,” *Revi. Sci. Instrum.*, vol. 66, no. 1, p. 97, 1995.

[39] R. Zhang, “Preparation of sharp polycrystalline tungsten tips for scanning tunneling microscopy imaging,” *J. Vac. Sci. Technol. B*, vol. 14, no. 1, p. 1, Jan. 1996.

[40] J. W. Gibbs, *The collected works of J.W. Gibbs*. New York: Ox Bow Press, 1906.

[41] J. L. F. Da Silva, C. Stampfl, and M. Scheffler, “Converged properties of clean metal surfaces by all-electron first-principles calculations,” *Surface Science*, vol. 600, no. 3, pp. 703–715, Feb. 2006.

[42] R. J. Needs and M. J. Mansfeld, “Calculations of the surface stress tensor and surface energy of the (111) surfaces of iridium , platinum and gold,” *J. Phys. Condens. Matter.*, vol. 1, p. 7555, 1989.

[43] N. Seriani, W. Pompe, and L. C. Ciacchi, “Catalytic oxidation activity of Pt_3O_4 surfaces and thin films,” *The journal of physical chemistry. B*, vol. 110, no. 30, pp. 14860–9, Aug. 2006.

[44] N. Vasiljevic, T. Trimble, N. Dimitrov, and K. Sieradzki, “Electrocapillarity behavior of Au111 in $SO_4^{(2-)}$ and F^-,” *Langmuir : the ACS journal of surfaces and colloids*, vol. 20, no. 16, pp. 6639–43, Aug. 2004.

[45] J. R. Mcbride, G. W. Graham, C. R. Peters, and W. H. Weber, “Growth and characterization platinum oxides of reactively sputtered thin-film,” *J. Appl. Phys.*, vol. 69, pp. 1596–1604, 1991.

[46] L. Tang, X. Li, R. C. Cammarata, C. Friesen, and K. Sieradzki, “Electrochemical stability of elemental metal nanoparticles.,” *Journal of the American Chemical Society*, vol. 132, no. 33, pp. 11722–6, Aug. 2010.

[47] A. Soon, M. Todorova, B. Delley, and C. Stampfl, “Thermodynamic stability and structure of copper oxide surfaces: A first-principles investigation,” *Physical Review B*, vol. 75, no. 12, pp. 1–9, Mar. 2007.

[48] T. Trimble, L. Tang, N. Vasiljevic, N. Dimitrov, M. van Schilfgaarde, C. Friesen, C. Thompson, S. Seel, J. Floro, and K. Sieradzki, “Anion adsorption induced reversal of coherency strain,” *Physical Review Letters*, vol. 95, no. 16, pp. 1–4, Oct. 2005.

[49] A. Sanson, F. Rocca, G. Dalba, P. Fornasini, R. Grisenti, M. Dapiaggi, and G. Artioli, “Negative thermal expansion and local dynamics in Cu_2O and Ag_2O,” *Physical Review B*, vol. 73, no. 21, pp. 1–13, Jun. 2006.

[50] M. Methfessel, D. Hennig, and M. Scheffler, “Trends of the surface relaxations, surface energies, and work functions of the 4d transition metals,” *Phys. Rev. B.*, vol. 46, no. 8, pp. 4816–4829, 1992.

[51] J. Wan, Y. Fan, D. Gong, S. Shen, and X. Fan, “Surface relaxation and stress of fcc metals : Cu , Ag , Au , Ni , Pd , Pt , Al and Pb,” *Modelling Simul. Mater. Sci. Eng.*, vol. 7, p. 189, 1999.

[52] P. J. Feibelman, “First-principles calculations of stress induced by gas adsorption on Pt(111),” *Physical Review B*, vol. 56, no. 4, pp. 2175–2182, Jul. 1997.

[53] A. Katagiri and M. Nakata, “Preparation of a high surface area nickel electrode by alloying and dealloying in a $ZnCl_2$-NaCl melt,” *Journal of The Electrochemical Society*, vol. 150, no. 9, p. C585, 2003.

[54] D. Kramer, R. N. Viswanath, and J. Weissmüller, “Surface-stress induced macroscopic bending of nanoporous gold cantilevers,” *Nano Letters*, vol. 4, no. 5, pp. 793–796, May 2004.

[55] N. V. Lavrik, C. A. Tipple, M. J. Sepaniak, and P. G. Datskos, “Enhanced chemi-mechanical transduction at nanostructured interfaces,” *Chemical Physics Letters*, vol. 336, pp. 371–376, 2001.

[56] Y. Ding, Y.-J. Kim, and J. Erlebacher, “Nanoporous gold leaf: ‘ancient technology’/advanced material,” *Advanced Materials*, vol. 16, no. 21, pp. 1897–1900, Nov. 2004.

[57] R. Li and K. Sieradzki, “Ductile-brittle transition in random porous Au,” *Phys. Rev. L.*, vol. 68, no. 8, p. 1168, 1992.

[58] H. Qiu, Z. Zhang, X. Huang, and Y. Qu, “Dealloying Ag-Al alloy to prepare nanoporous silver as a substrate for surface-enhanced raman scattering: effects of structural evolution and surface modification,” *Chemphyschem : a European journal of chemical physics and physical chemistry*, May 2011.

[59] J. R. Hayes, A. M. Hodge, J. Biener, A. V. Hamza, and K. Sieradzki, "Monolithic nanoporous copper by dealloying Mn–Cu," *Journal of Materials Research*, vol. 21, no. 10, pp. 2611–2616, Mar. 2011.

[60] T. Wada, K. Yubuta, A. Inoue, and H. Kato, "Dealloying by metallic melt," *Materials Letters*, vol. 65, no. 7, pp. 1076–1078, Apr. 2011.

[61] A. Dursun, D. V. Pugh, and S. G. Corcoran, "Probing the dealloying critical potential," *Journal of The Electrochemical Society*, vol. 152, no. 2, p. B65, 2005.

[62] D. Stauffer, *Introduction to percolation theory*. London: Taylor and Francis, 1985.

[63] J. Erlebacher, "An atomistic description of dealloying," *Journal of The Electrochemical Society*, vol. 151, no. 10, p. C614, 2004.

[64] A. Henglein, "Physicochemical properties of small metal particles in solution: 'Microelectrode' reactions, chemisorption, composite metal particles, and the atom-to-metal transition," *J. Phys. Chem.*, vol. 97, p. 5457, 1993.

[65] Y. Volokitin, J. Sinzig, L. de Jongh, G. Schmid, M. Vargaftik, and I. Moiseev, "Quantum-size effects in the thermodynamic properties of metallic nanoparticles," *Nature*, vol. 384, p. 621, 1996.

[66] C. Alonso, R. C. Salvarezza, J. M. Vara, and a. J. Arvia, "The surface diffusion of gold atoms on gold electrodes in acid solution and its dependence on the presence of foreign adsorbates," *Electrochimica Acta*, vol. 35, no. 9, pp. 1331–1336, Jan. 1990.

[67] I. McCue, J. Snyder, X. Li, Q. Chen, K. Sieradzki, and J. Erlebacher, "Apparent inverse Gibbs-thomson effect in dealloyed nanoporous nanoparticles," *Physical Review Letters*, vol. 108, no. 22, pp. 1–5, May 2012.

[68] I. Dutta, M. K. Carpenter, M. P. Balogh, J. M. Ziegelbauer, T. E. Moylan, M. H. Atwan, and N. P. Irish, "Electrochemical and structural study of a chemically dealloyed PtCu oxygen reduction catalyst," *The Journal of Physical Chemistry C*, vol. 114, no. 39, pp. 16309–16320, Oct. 2010.

[69] P. Mani, R. Srivastava, and P. Strasser, "Dealloyed binary PtM_3 (M=Cu, Co, Ni) and ternary $PtNi_3M$ (M=Cu, Co, Fe, Cr) electrocatalysts for the oxygen reduction reaction: Performance in polymer electrolyte membrane

fuel cells," *Journal of Power Sources*, vol. 196, no. 2, pp. 666–673, Jan. 2011.

[70] R. Srivastava, P. Mani, and P. Strasser, "In situ voltammetric de-alloying of fuel cell catalyst electrode layer: A combined scanning electron microscope/electron probe micro-analysis study," *Journal of Power Sources*, vol. 190, no. 1, pp. 40–47, May 2009.

[71] P. Strasser, S. Koh, T. Anniyev, J. Greeley, K. More, C. Yu, Z. Liu, S. Kaya, D. Nordlund, H. Ogasawara, M. F. Toney, and A. Nilsson, "Lattice-strain control of the activity in dealloyed core-shell fuel cell catalysts.," *Nature chemistry*, vol. 2, no. 6, pp. 454–60, Jun. 2010.

[72] M. Oezaslan, M. Heggen, and P. Strasser, "Size-dependent morphology of dealloyed bimetallic catalysts: linking the nano to the macro scale.," *Journal of the American Chemical Society*, vol. 134, no. 1, pp. 514–24, Jan. 2012.

[73] S. Chen, H. a. Gasteiger, K. Hayakawa, T. Tada, and Y. Shao-Horn, "Platinum-alloy cathode catalyst degradation in proton exchange membrane fuel cells: nanometer-scale compositional and morphological changes," *Journal of The Electrochemical Society*, vol. 157, no. 1, p. A82, 2010.

[74] J. Snyder, I. McCue, K. Livi, and J. Erlebacher, "Structure/processing/properties relationships in nanoporous nanoparticles as applied to catalysis of the cathodic oxygen reduction reaction," *Journal of the American Chemical Society*, vol. 134, p. 8633, May 2012.

[75] H. Bönnemann and R. M. Richards, "Nanoscopic metal particles synthetic methods and potential applications," *Eur. J. Inorg. Chem.*, pp. 2455–2480, 2001.

[76] C. Burda, X. Chen, R. Narayanan, and M. a El-Sayed, *Chemistry and properties of nanocrystals of different shapes.*, vol. 105, no. 4. 2005, pp. 1025–102.

[77] A. Chen and P. Holt-Hindle, "Platinum-based nanostructured materials: Synthesis, properties, and applications," *Chemical reviews*, vol. 110, no. 6, pp. 3767–804, Jun. 2010.

[78] J. Park, J. Joo, S. G. Kwon, Y. Jang, and T. Hyeon, "Synthesis of monodisperse spherical nanocrystals," *Angewandte Chemie (International ed. in English)*, vol. 46, no. 25, pp. 4630–60, Jan. 2007.

[79] C.-J. Zhong, J. Luo, B. Fang, B. N. Wanjala, P. N. Njoki, R. Loukrakpam, and J. Yin, “Nanostructured catalysts in fuel cells.,” *Nanotechnology*, vol. 21, no. 6, p. 062001, Feb. 2010.

[80] N. Toshima and T. Yonezawab, “Bimetallic nanoparticles-novel materials for chemical and physical applications,” *New J. Chem.*, pp. 1179–1201, 1998.

[81] S. G, *Nanoparticles: From theory to application*. Wiley-VCH, 2010.

[82] S. G. Lemay, D. M. van den Broek, A. J. Storm, D. Krapf, R. M. M. Smeets, H. a Heering, and C. Dekker, “Lithographically fabricated nanopore-based electrodes for electrochemistry,” *Analytical chemistry*, vol. 77, no. 6, pp. 1911–5, Mar. 2005.

[83] D. Krapf, M.-Y. Wu, R. M. M. Smeets, H. W. Zandbergen, C. Dekker, and S. G. Lemay, “Fabrication and characterization of nanopore-based electrodes with radii down to 2 nm,” *Nano letters*, vol. 6, no. 1, pp. 105–9, Jan. 2006.

[84] P. Singh and D. a. Buttry, “Comparison of oxygen reduction reaction at silver nanoparticles and polycrystalline silver electrodes in alkaline solution,” *The Journal of Physical Chemistry C*, vol. 116, no. 19, pp. 10656–10663, May 2012.

[85] N. Braidy, Z. J. Jakubek, B. Simard, and G. a Botton, “Quantitative energy dispersive X-ray microanalysis of electron beam-sensitive alloyed nanoparticles.,” *Microscopy and microanalysis : the official journal of Microscopy Society of America, Microbeam Analysis Society, Microscopical Society of Canada*, vol. 14, no. 2, pp. 166–75, Apr. 2008.

[86] C. E. Lyman, R. E. Lakis, B. Totdal, and R. Prestvik, “Analysis of alloy nanoparticles,” *Mikrochim. Acta*, vol. 132, pp. 301–308, 2000.

[87] A. Wijaya and K. Hamad-Schifferli, “Ligand customization and DNA functionalization of gold nanorods via round-trip phase transfer ligand exchange,” *Langmuir : the ACS journal of surfaces and colloids*, vol. 24, no. 18, pp. 9966–9, Sep. 2008.

[88] E. Delamarche, B. Michel, H. Kang, and C. Gerber, “Thermal stability of self-assembled monolayers,” *Langmuir*, vol. 10, no. 31, pp. 4103–4108, 1994.

[89] C. A. Widrig, C. Chung, and M. D. Porter, "The electrochemical desorption of n-alkanethiol from polycrystalline Au and Ag electrodes monolayers," *J. Electroanal. Chem.*, vol. 310, pp. 335–359, 1991.

[90] M. M. Walczak, D. D. Popenoe, R. S. Deinhammer, B. D. Lamp, C. Chung, and M. D. Porter, "Reductive desorption of alkanethiolate monolayers at gold: A measure of surface coverage," *Langmuir*, vol. 7, no. 12, pp. 2687–2693, 1991.

[91] L. Deng, W. Hu, H. Deng, S. Xiao, and J. Tang, "Au-Ag bimetallic nanoparticles : surface segregation and atomic-scale structure," *J. Phys. Chem. C*, vol. 115, pp. 11355–11363, 2011.

[92] S. Link, Z. L. Wang, and M. EI-Sayed, "Alloy formation of gold-silver nanoparticles and the dependence of the plasmon absorption on their composition," *J. Phys. Chem. B*, vol. 103, pp. 3529–3533, 1999.

[93] J. M. Dona and J. Gonzalez-Velasco, "The dependence of the surface diffusion coefficients of gold atoms on the potential : its influence on reconstruction of metal lattices," *Surf. Sci.*, vol. 274, p. 205, 1992.

[94] S. Dieluweit, H. Ibach, and M. Giesen, "Potential dependence of step and kink energies on Au(100) electrodes in sulfuric acid," *Faraday Discussions*, vol. 121, no. 100, pp. 27–42, Aug. 2002.

[95] E. Pichardo-Pedrero, G. L. Beltramo, and M. Giesen, "Electrochemical annealing and its relevance in metal electroplating: An atomistic view," *Applied Physics A*, vol. 87, no. 3, pp. 461–467, Mar. 2007.

[96] H. Hovel, T. Becker, A. Bettac, B. Reihl, M. Tschudy, and E. J. Williams, "Controlled cluster condensation into preformed nanometer-sized pits," vol. 81, no. 1, pp. 154–158, 1997.

APPENDIX A

AU 2D ISLANDS DECAY

The stability of Au islands from lifted reconstruction in 0.1M H_2SO_4 was studied by in situ ECSTM. Fresh deposited Au (111) film was used as the working electrode and Pd-H wire was used as reference electrode. A PtIr tip coated by Apiezon wax was used for scanning and the leaking current was less than 20 pA. The tunneling current for imaging was 0.6nA. The potential was ramped up to 1.2 V to lightly oxidized the Au surface and then jumped back to 0.8 V at which lots of Au island (3-8 nm in diameter) appeared on the surface. Then the voltage was increased with a 20 mV step up to 1.15 V vs. NHE. Figure A.1 are the ECSTM images at selective voltages and Figure A.2 shows the plot of the island sizes versus voltages at which there is an obvious size change of the islands.

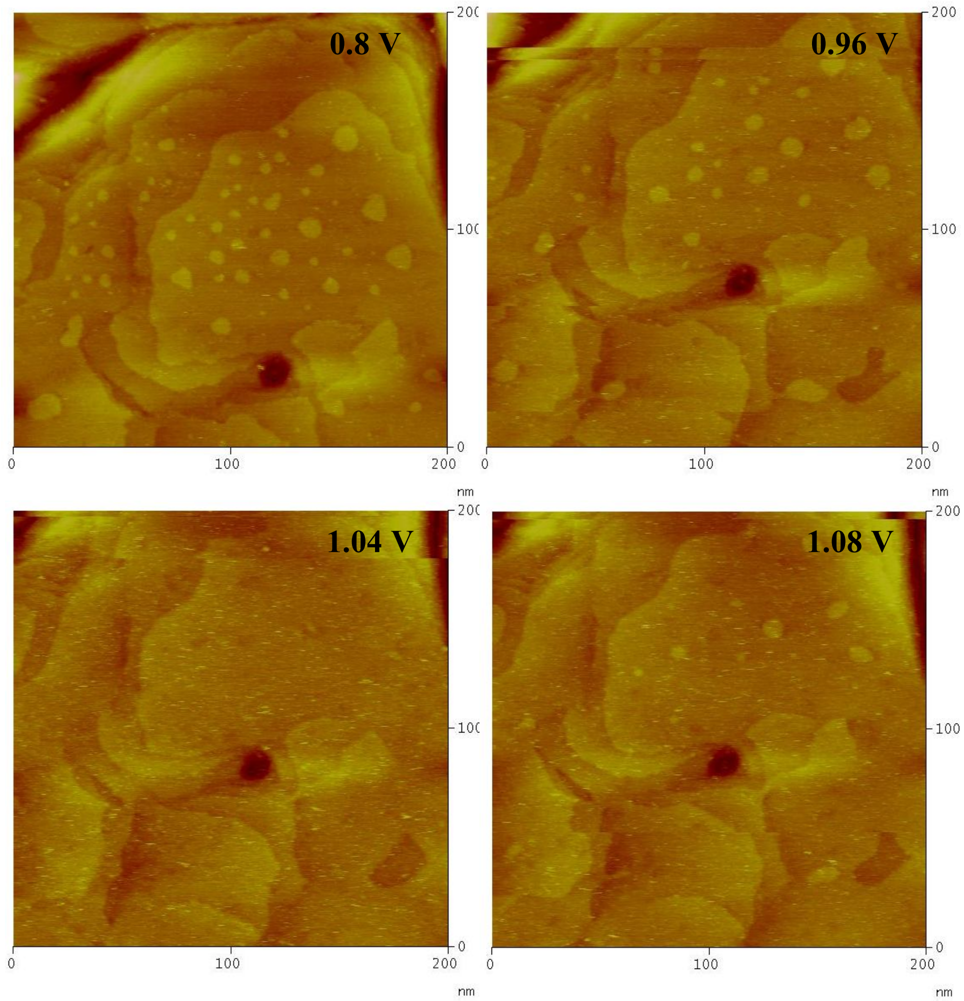

Figure A.1. ECSTM images of the Au 2D island decay as voltage increases.

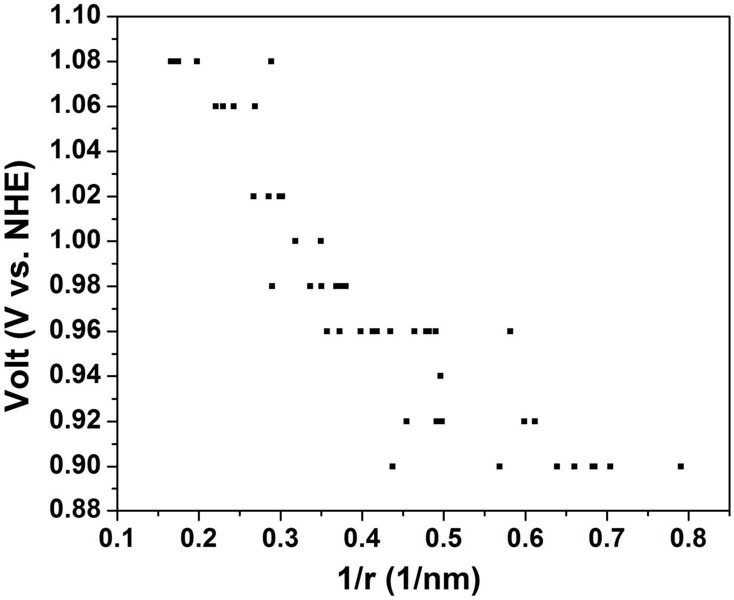

Figure A.2. Au island sizes (1/r) versus dissolution potentials.

For 2D islands, the Gibbs-Thomson equation transforms to

$$\Delta V = \frac{\rho A}{nqr} = \frac{\gamma a A}{nqr} = \frac{\gamma \Omega}{nqr}. \tag{A.1}$$

Assuming during the dissolution process, Au became Au^+, the calculated surface energy is $2.55 J/m^2$, which is about twice of the known value. If calculate the step energy based on this surface energy:

$$\rho = \gamma a = 2.55 \times 4.03 / \sqrt{3} \times 10^{-10} = 6 \times 10^{-10} J/m, \tag{A.2}$$

which is

$$\frac{6 \times 10^{-10} J/m \times 2.88 \times 10^{-10} m/atom}{1.6 \times 10^{-19} C} = 1.08 eV/atom. \tag{A.3}$$

According to Giesen's paper[94][95], the step energy for Au is even less than 0.1eV (~0.04eV) and the step energy for Ag is ~0.3eV.

APPENDIX B

CLUSTER DEPOSITION ON SPUTTERED HOPG

Another technique of preparing particles [96] was tried to see whether it would increase the adhesion between particles and substrate for ECSTM experiment. HOPG was selected as substrate and sputtered by Argon ions (0.5 KV beam voltage, 3 mA emission current, 2 s) to generate a decent density of defects. Then this sputtered surface was thermal annealed in air at 530°C for 40 min to coarsen the defects and burn away the sputtered C around the defects. Figure B.1 are the HOPG surface before sputtering, after sputtering, and after heat treatment. Then ~0.5 monolayer Au was deposited on the sputtered HOPG surface with a rate of 0.1 Å/s at 340°C. The resulting surface was checked in STM with a tunneling current of 200 pA. The adhesion between particles and substrate was still not quite good. STM images in Figure B.2 show that some particles were pushed away after one scan.

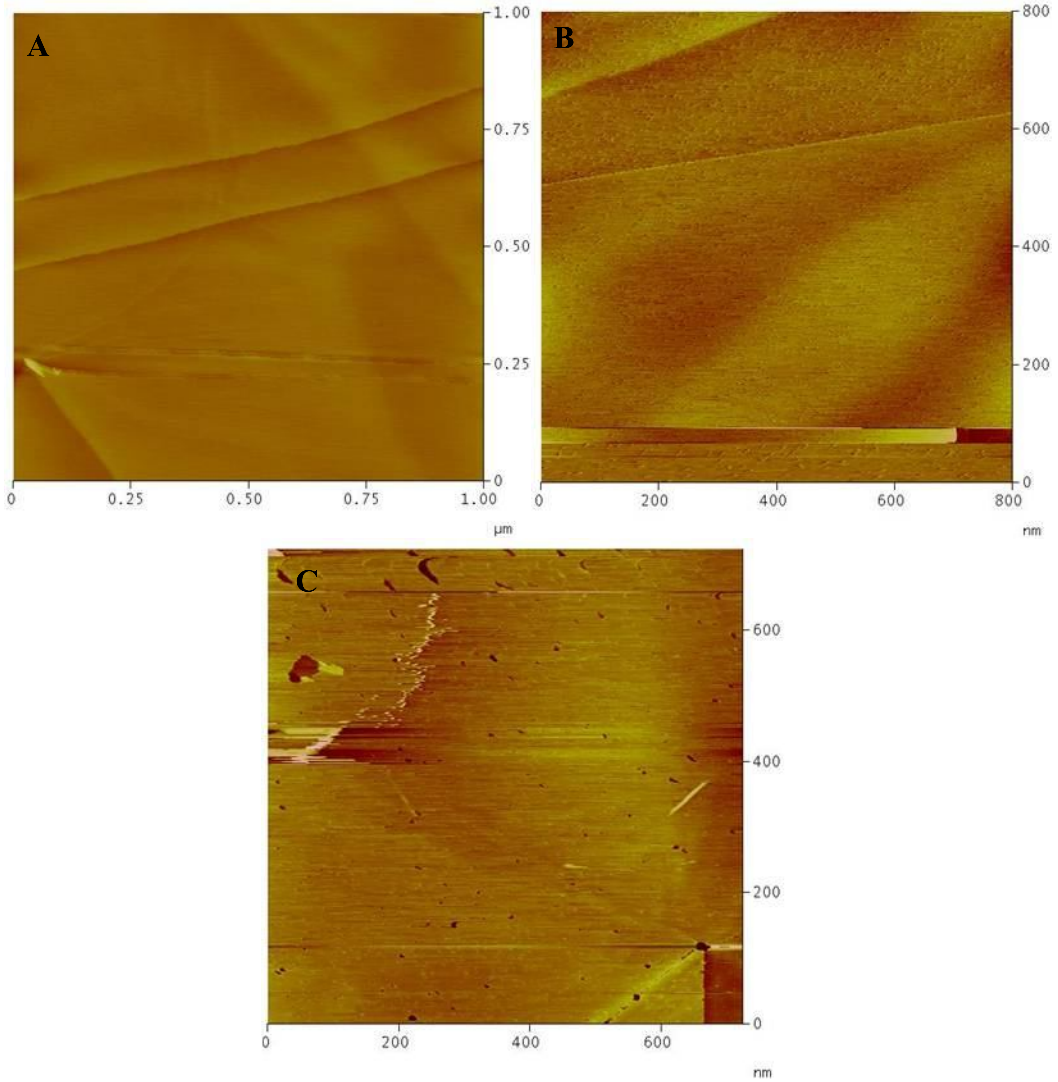

Figure B.1. STM height mode images for: (A) Fresh HOPG surface. (B) HOPG surface after sputtering. (C) HOPG surface after heat treatment.

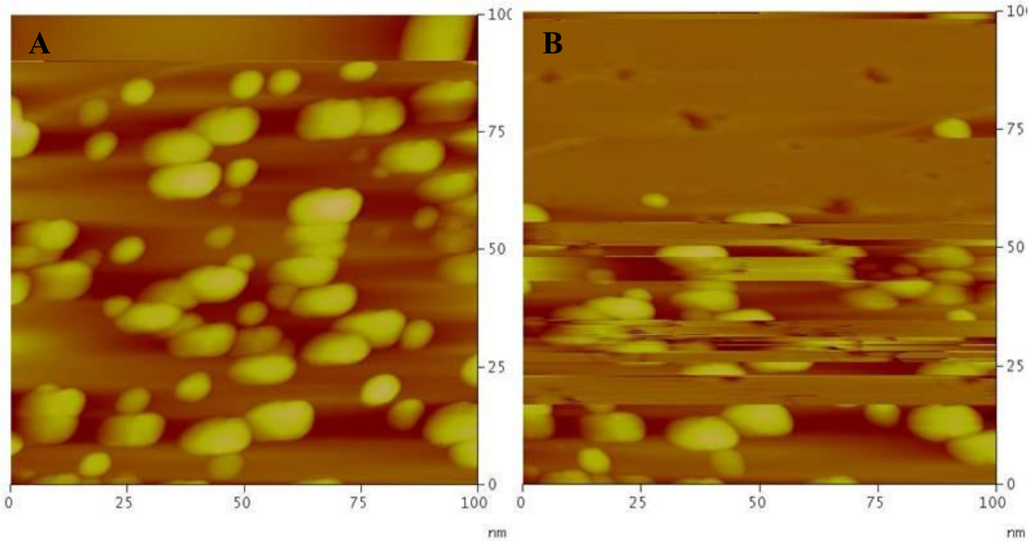

Figure B.2. STM images (100 × 100 nm) of Au clusters deposited by E-beam deposition on sputtered HOPG surface: (A) 1st scan. (B) 2nd scan.

APPENDIX C

CALCULATION OF MOLAR VOLUME FOR METAL OXIDE

Ag_2O and Cu_2O compounds are both cuprite structure, which is made up by two interpenetrating lattices, one fcc of metal atom and one bcc of oxygen atom as shown in Figure C.1. The lattice constant is 4.27 Å for Cu_2O and 4.72 Å for Ag_2O [49][47]. The molar volume of Cu_2O and Ag_2O would be:

$(4.27\times10^{-8})^3\times0.5\times6.02\times10^{23}$ cm^3 = 23.4×10^{-6} cm^3.

$(4.72\times10^{-8})^3\times0.5\times6.02\times10^{23}$ cm^3 = 31.6×10^{-6} cm^3.

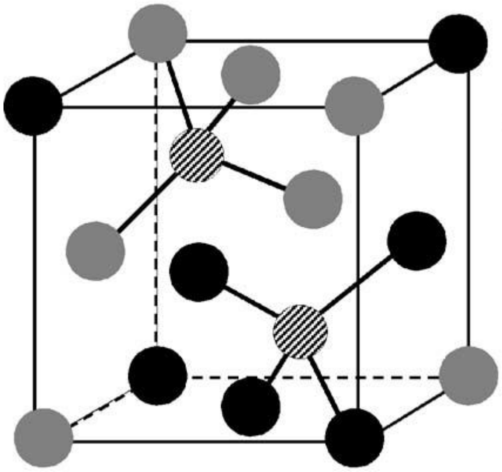

Figure C.1. The cuprite structure. The full circles are fcc unit cell of metal atoms and the dashed circles are oxygen atoms [49].